

Leopold-Franzens-Universität Innsbruck

Master's Thesis

**Simultaneous and individual ion addressing for quantum
information processing**



in partial fulfillment of the requirements
for the degree of
MASTER OF SCIENCE (MSc.)

carried out at the Institute of Experimental Physics
under the guidance of Rainer Blatt

presented by
Julian Rickert

November 2018

Abbreviations

AOM	Acousto-Optical Modulator
CCD	Charge-Coupled Device
CNOT-gate	Controlled-NOT gate
EMCCD	Electron Multiplying Charge-Coupled Device
EOD	Electro-Optic Deflector
FBS	Fibre Beam Splitter
FC/APC	Fibre Connector / Angled Physical Contact
MMA	Micro-Mirror Array
MS-gate	Mølmer-Sørensen gate
NA	Numerical Aperture
PBS	Polarising Beam Splitter
PER	Polarisation Extinction Ratio
PM	Polarisation Maintaining
PMT	Photo-Multiplier Tube
RF	Radio Frequency
ROC	Radius Of Curvature
SM	Single-Mode

Kurzfassung

Auf dem Weg zu fehlertoleranten Quantencomputern wird es notwendig, Quantengatter auf einem Qubit-Register in einer kurzen Zeitspanne durchzuführen. Bei Ionen-Quantencomputern werden diese Gatter durch eine kontrollierte Wechselwirkung der Ionen mit eingestrahlten Lasern implementiert. Diese Masterarbeit beschäftigt sich mit der Entwicklung und Implementierung eines neuen Aufbaus zur Einzelionenadressierung, welcher die gleichzeitige und individuelle Manipulation der Ionen ermöglicht. In diesem Aufbau werden Faser-Strahlteiler verwendet, um den adressierten Strahl in mehrere Teilstrahlen zu zerlegen. Anschließend steuern fasergekoppelte akusto-optische Modulatoren jeden der Teilstrahlen individuell. Ein Mikrospiegelarray wird dazu verwendet, um die einzelnen Strahlen auf die Positionen der Ionen zu lenken. Die Optik zur Fokussierung der Strahlen wird simuliert und in einem Testaufbau untersucht. Der aussichtsreichste der simulierten Aufbauten, welcher zur Adressierung von bis zu vier Ionen benutzt werden kann, wird im Experiment implementiert. Der minimale Strahlradius des mittleren Adressierstrahls in diesem Aufbau wird zu $w_0 = 1.52(5) \mu\text{m}$ bestimmt. Im Ausblick auf zukünftige Experimente werden Simulationen mit einem Objektiv mit hoher NA ~ 0.8 durchgeführt; diese Simulationen legen die Adressierbarkeit von bis zu 19 Ionen nahe.

Abstract

For fault tolerant quantum computing it is necessary to perform a series of quantum gates on a register of qubits in a short period of time. In the case of an ion trap quantum computer these gates are implemented by shining laser beams onto the ions in a controlled way. This thesis deals with the development and implementation of a novel setup for single ion addressing, which enables simultaneous and individual manipulation of the ions. The new setup makes use of fibre beamsplitters for multiplexing the addressing laser and fibre AOMs for altering each beam individually. A micro-mirror array is utilised to point each beam to a single ion. The optics needed to focus the beams onto individual ions is simulated and investigated in a test setup. The most promising of the simulated setups, which is expected to be able to address up to four ions, is implemented into the experiment. The waist of the central addressing beam in this setup is measured to be $w_0 = 1.52(5) \mu\text{m}$. For future experiments, simulations with another objective with NA ~ 0.8 are performed, which indicate addressability of up to 19 ions.

Contents

1. Introduction	3
2. Theoretical framework	8
2.1. The Paul trap	8
2.2. Atom-light-interaction	10
2.3. Quantum computation	13
2.4. Ray optics	16
2.5. Gaussian optics	18
3. Experimental setup	23
3.1. The $^{40}\text{Ca}^+$ ion	24
3.2. Detection of the qubit state	25
3.2.1. PMT	26
3.2.2. EMCCD	27
3.3. The existing qubit laser beam path	29
3.4. The new 729 nm beam path	30
3.4.1. Fibre optics	31
3.4.2. Free space optics	36
4. Optical design and tests	40
4.1. Characterising the output beam of the fibre array	40
4.2. Simulating the lens array	42
4.3. Optical setup to address small strings of ions	46
4.3.1. Simulation of the setup	48
4.3.2. Experimental test setup	51
5. Characterisation of the addressing beams	55
5.1. Testing the addressing setup	55
5.2. Imaging calibration	56
5.3. Beam-width measurement	58
5.4. Addressing in an ion crystal	61
6. Summary and outlook	65
A. ZEMAX OpticStudio	70
B. Specifications of the new fibre array from SQS	76

Contents

Bibliography

81

1. Introduction

The discovery of quantum mechanics was one of the greatest advances in science in the 20th century. Quantum mechanics was formulated in 1926 by *E. Schrödinger* [1] and *W. Heisenberg* [2] in two equivalent theories and is used to describe the states of microscopic particles and their evolution in time, the understanding of which led to numerous technological advances such as transistors, light-emitting diodes, and lasers.

Another great advance of the last century was the concept of the modern computer introduced by *A. Turing* [3], who proposed a device, that could be used to perform any computation; a so called universal computing machine. Today's computers are realised with transistors, which incorporate quantum mechanical elements but are still governed by classical laws. Thus, computations are still carried out with classical bits, that can take on the values 0 or 1.

In the early 1980s several people proposed to perform computations on quantum mechanical states instead of using digital bits [4, 5, 6]. Since then, it has been shown theoretically that such quantum computers are able to implement quantum algorithms which outperform the best classical algorithms known today. These quantum algorithms include the factorisation of natural numbers into their prime factors [7] and the search of unsorted databases [8]. Further, it was shown that quantum computers might outperform classical computers in simulating quantum mechanical systems [9]. In quantum computers, bits are exchanged by quantum mechanical two-state systems called qubits [10]. Today, several quantum mechanical systems, that could host as a qubit, have been investigated in laboratory experiments. Those qubit candidates include the electronic states in ions [11], the polarisation state of photons [12], and fluxes in superconducting circuits [13].

A promising candidate for a large scale quantum computer is the linear ion trap quantum computer with $^{40}\text{Ca}^+$ ions, as used in our laboratory [14], which can be scaled up by connecting several linear ion traps with photonic interconnects [15]. The creation of a 14-qubit entangled state [16], error correction procedures enhancing the coherence time of the qubits [17], the implementation of Shor's algorithm [18], and digital quantum simulation [19] have been demonstrated in the research group of *Prof. Rainer Blatt*.

The computer could be used to perform any quantum computation, since a universal gate set has been implemented [20]. Currently, we use two different laser beams to mediate a coupling between two electronic levels of an ion; those two levels serve as a qubit. One beam illuminates the string of ions globally and is used to perform entangling gates between all ions in the ion string and rotations of the qubit states around the x/y-axis on all ions simultaneously. A second, tightly focused, steerable beam is used to implement phase shifts, i.e. rotations around the z-axis, on single ions. A scheme of this setup is depicted in Figure 1.1.

1. Introduction

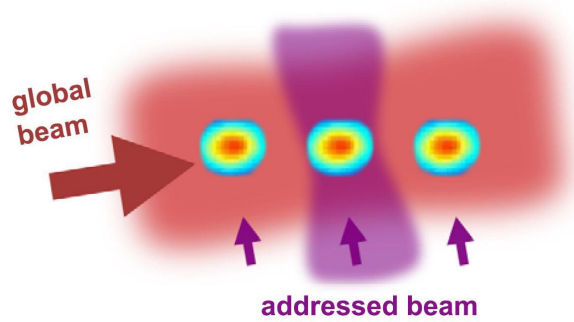


Figure 1.1.: In the current addressing setup a global beam illuminates all ions at once and an additional addressed beam is focused onto single ions. These two beams are used to implement a universal gate set onto the ion string. A scheme of the current single ion addressing setup is given in Fig. 1.2 a. The image was taken from Ref. [14].

In the past years, this setup has been optimised to perform quantum gates with high fidelities. However, the efficiency with which quantum operations can be applied to the ions is limited by the addressing setup, since it can only be used to address one ion at a time or all ions at once with a globally applied laser field. Thus, if one wants to perform a quantum gate on a subset of ions, the other ions need to be hidden from the global beam [17], which leads to an additional overhead in laser pulses that need to be applied to the ion string.

In this thesis, I propose and characterise a new addressing scheme, which can be used to address all ions simultaneously and individually. Due to this, the new addressing scheme would reduce the number of pulses needed to implement quantum gates on subsets of the ion string. Thus, the capabilities of the ion quantum computer would be enhanced through a speed-up in the application of quantum algorithms. For example, performing arbitrary rotations and entangling gates on arbitrary subsets of qubits would reduce the number of gates needed to perform certain error correction codes. One of these codes is the color code, which has already been implemented in our experiment [17].

There exist a few different single ion addressing setups with focused laser light that were developed and tested during the last 20 years. In the following paragraph some of those setups and the advances, which they put forward are summarised; the new setup proposed in this thesis is put into context with the other addressing schemes.

In 1999 *H.C. Nägerl* in the group of *Prof. Rainer Blatt* demonstrated for the first time the addressability of individual ions in a Paul trap with a laser beam [21]. In this experiment the addressing laser was moved from one $^{40}\text{Ca}^+$ ion to the neighbouring $^{40}\text{Ca}^+$ ion by deflecting it with an acousto-optic deflector (AOD). Here, an AOD is a crystal with a radio-frequency (RF) signal applied to it, which leads to deflection and frequency mixing with a light field passing through the crystal. A detailed description of this effect can be found in Ref. [22]. By applying several RF signals to the AOD, several output beams with different frequencies and different deflection angles are generated. Resonant interactions cannot be implemented without an experimental overhead, since the output frequencies depend on the deflection angle

imprinted by the AOD. Today, an AOD is used to perform rotations around the z-axis in another linear ion trap experiment in the group of *Prof. Rainer Blatt* [23]. A scheme of the AOD addressing setup is given in Fig. 1.2 b.

Another setup for single ion addressing makes use of an electro-optic deflector (EOD) to deflect a laser beam passing through it. An EOD is a device containing a crystal whose index of refraction changes when applying a constant electric field to it. A light field passing through the crystal is deflected by this change; this effect is called the electro-optic effect and is described in Ref. [22]. In 2003 *F. Schmidt-Kaler* in the group of *Prof. Rainer Blatt* used an EOD addressing setup to achieve a universal quantum gate set for trapped ions for the first time [20]. They used the EOD to move the addressing laser beam between ions in the trap and could demonstrate individual addressability of two ions; they were able to perform single qubit gates on the ions and showed the implementation of an entangling gate between both ions. A scheme of the EOD addressing setup is given in Fig. 1.2 a. This setup is currently used for single ion addressing in our experiment; it will be described in detail in Ch. 3.3.

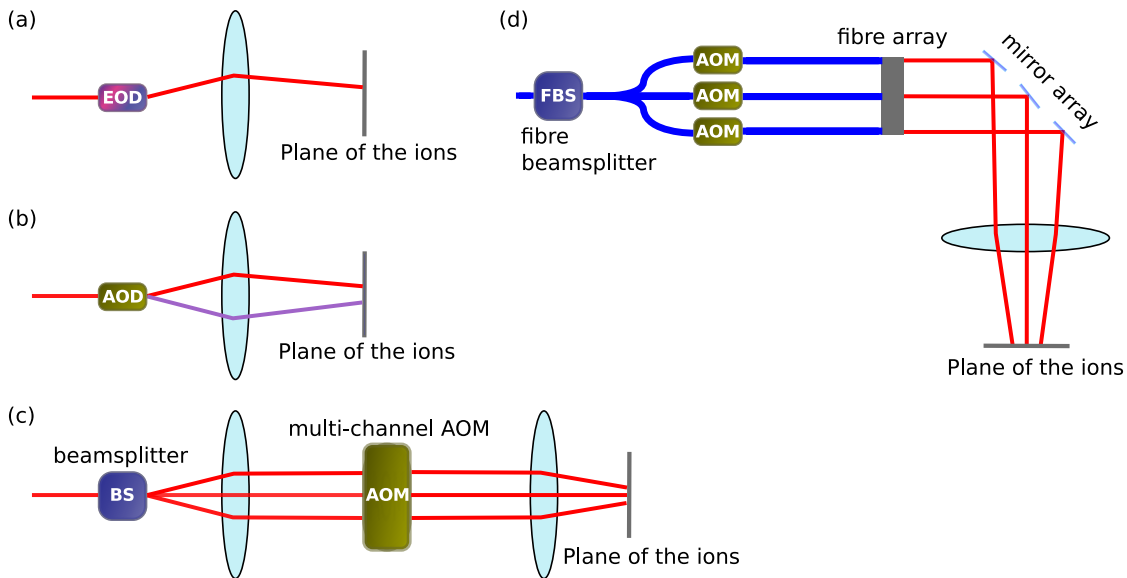


Figure 1.2.: Schemes of different setups for single ion addressing with focused laser beams. (a) Addressing via moving the beam with an EOD. (b) Addressing via moving the beam with an AOD. The AOD can produce several output beams which have a frequency that depends on the deflection angle. (c) Addressing via multiplexing the beam in a beamsplitter and altering each beam in a multi-channel AOM (acousto-optical modulator). (d) The setup proposed in this thesis. An FBS (fibre beamsplitter) is used for multiplexing the beam, each beam is altered with a fibre AOM and directed onto the ion positions via a mirror array.

In 2016 *S. Debnath* in the group of *Prof. Christopher Monroe* demonstrated another architecture

1. Introduction

for ion quantum computers, which uses a different gate set than the one implemented with the EOD and the global beam in our experimental setup [24]. Here, Raman transitions are employed to connect the two electronic qubit states in $^{171}\text{Yb}^+$ ions. In their experiment, they use a chain of seven ions which are illuminated by a global Raman beam from one direction and seven individual Raman beams from the opposing direction. Those individual beams are generated by a diffractive beam splitter and modulated individually by a multi-channel AOM. Thus, this setup enables individual and simultaneous addressing of up to seven ions. A scheme of the setup is given in Fig. 1.2 c. The implemented gate set consists of arbitrary single qubit rotations about any axis on the equator of the Bloch sphere and two qubit entangling gates between any of the seven qubits [25].

In this thesis a different setup for obtaining individual and simultaneous ion addressing is proposed and tested. This optical setup makes use of fibre beamsplitters and fibre AOMs to generate multiple laser beams with individual phase, amplitude and frequency profiles. A micro-mirror array is used to guide the single laser beams onto the positions of the ions. Each beam is used to address a single ion. Therefore, the number of ions that can be addressed with this setup is equal to the number of laser beams generated by the fibre beamsplitters. These beams can be used to implement arbitrary single qubit rotations on each ion individually and simultaneously. Additionally, Mølmer-Sørensen-gates [26] can be performed on arbitrary subsets of ions. Thus, this single ion addressing setup renders the global beam obsolete for performing quantum gates on the ions. The scheme of this setup is shown in Fig. 1.2 d and compared to the other addressing setups in Table 1.1.

As mentioned before, the two latter approaches implement a different gate set than previous ones. This new gate set is more versatile than the formerly implemented gate set in the sense that a larger set of gates can be implemented with a single laser pulse or a single set of laser pulses applied simultaneously.

Table 1.1.: Summary of experimental schemes for single ion addressing with focused laser light

Scheme	References	# of addressable qubits	simultaneous addressing	full phase/frequency control
AOD	[21], [27], [23]	~20	yes	no
EOD	[14], [20]	~10	no	yes
multi-channel AOM	[24], [25]	7	yes	yes
fibre AOMs and micro-mirror array	this thesis	4(19)	yes	yes

This thesis is structured in the following way:

In Chapter 2 the basics of trapped ions interacting with laser fields are summarised and a short introduction to quantum computation with trapped ions is given. Further, the theory of propagation of laser beams through the addressing setup is reviewed in Sections 2.4 and 2.5.

In Chapter 3 the transitions in $^{40}\text{Ca}^+$ employed for state preparation, measurement and state manipulation are outlined. Furthermore, in Section 3.2 the two detection methods for detecting the state of the ions are discussed. The two Sections 3.3 and 3.4 describe the current single addressing setup and the scheme of the new addressing setup proposed in this thesis. Also, the fibre optics employed for the new setup are characterised.

The optical setup following the fibre optics, i.e. the free space optics for the new addressing setup was simulated with ZEMAX OpticStudio. Those simulations are presented in Chapter 4. Moreover, the most promising of the simulated setups, able to address up to four ions, has been implemented in an experimental test setup for comparison with the simulation; the results from this test setup are also summarised here. Chapter 5 summarises the main results of this thesis obtained from integrating the test setup into the experiment. Measurements of the beam waist of the central addressing beam and the crosstalk between the addressing beams in a three ion crystal are presented in Sections 5.3 and 5.4. Chapter 6 summarises the work of this thesis and gives an outlook on how the new addressing setup can be improved in the future. Further, another experimental setup with a different objective, wherewith more than four ions could be addressed, is investigated.

2. Theoretical framework

Ions are confined in a trap to perform quantum information processing with them. The trap used in this thesis is a *Paul trap* whose properties are discussed in Section 2.1. Manipulating the state of ions requires them to interact with electro-magnetic fields. The type of this interaction is described in Section 2.2 based on Refs. [28] and [29]. The principles of quantum computation with special emphasis on trapped ion quantum computation are given in Section 2.3. Sections 2.4 and 2.5 summarise the most important aspects of optical systems. The theory of optical systems is presented in much more detail in Refs. [30], [22] and [31].

2.1. The Paul trap

The ions in our experiment are trapped by oscillating electric fields, which generate a so called *Paul trap* whose working principle was first proposed by *W. Paul* and *H. Steinwedel* in Ref. [32]. In our experiment we use a linear Paul trap which is discussed in great detail in Ref. [33]. Here, the principles of a linear Paul trap, which is depicted in Figure 2.1, will be outlined.

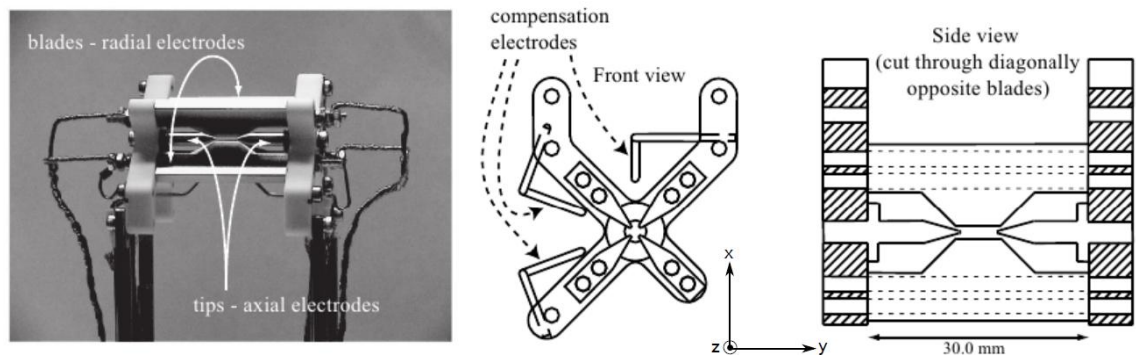


Figure 2.1.: Left: Picture of the linear Paul trap currently used in the experiment. Four blades provide the electric fields for radial confinement while the fields for axial confinement are applied to the two endcap electrodes. Right: Cut through the trap along the z -direction and along the radial direction. Compensation electrodes are used to move the potential minimum into the centre of the trap where micromotion is minimal. The image was taken from Ref. [33].

A Paul trap generates a potential of the form

$$\Phi(\vec{r}) = V \frac{x^2 - y^2}{2r_0^2} \cos(\Omega t) + \Phi_{axial}(\vec{r}) \quad (2.1)$$

where $V = 2(V_1 - V_2)$ with V_1 and V_2 being the voltages applied to two diagonally opposing electrodes of the trap, r_0 is the minimal distance of the trap axis to the electrodes and Ω is a radio frequency that changes the orientation of the applied electric field. The additional axial trapping potential $\Phi_{axial}(\vec{r}) = V_{cap} \cdot z^2/L^2$ is obtained from applying a DC potential V_{cap} to the two endcaps of the trap. Here, L is the distance between the two endcaps.

The resulting equations of motion for ions in a potential given by Eq. 2.1 are discussed in [34]. They are

$$\frac{d^2x}{d\tau^2} + (b - 2q \cos(2\tau)) x = 0 \quad (2.2)$$

$$\frac{d^2y}{d\tau^2} + (b + 2q \cos(2\tau)) y = 0 \quad (2.3)$$

$$\frac{d^2z}{d\tau^2} + 2bz = 0 \quad (2.4)$$

where

$$\tau = \frac{1}{2}\Omega t \quad \text{and} \quad b = \frac{e\alpha V_{cap}}{ML^2\Omega^2} \quad \text{and} \quad q = \frac{2eV}{Mr_0^2\Omega^2} \quad (2.5)$$

with α being a numerical factor that depends on the trap geometry, Ω and r_0 as in Eq. 2.1, M and e the mass and charge of an ion, L the distance between the two endcaps and V_{cap} the voltage applied to them. These equations result in a harmonic axial motion with frequency

$$\omega_{tr} = \sqrt{\frac{e\alpha V_{cap}}{2ML^2}} \quad (2.6)$$

Moreover, the radial motion is harmonic and given by the trap frequency

$$\omega_r = \omega_x = \omega_y = \sqrt{\frac{q\Omega}{2\sqrt{2}} - \frac{1}{2}\omega_z^2} \quad (2.7)$$

For quantum computing applications the radial trapping frequency is chosen much larger than the axial frequency to obtain one dimensional chains of atoms.

If one wants to address single ions with focussed laser light, the distance between ions in an ion string is a crucial parameter for performing quantum information processing on them, since it should be larger than the waist of the addressing beam to avoid addressing more than one ion with a single beam. The distance between ions in an ion string has been investigated by *D. F. V. James* in [35]. According to his findings the position of the n^{th} ion in a Paul trap is given by

$$x_n = u_n \cdot \sqrt[3]{\frac{e^2}{4\pi\epsilon_0 M \omega_{tr}^2}} \quad (2.8)$$

2. Theoretical framework

with the scaled equilibrium positions u_n given in [35], the mass of the ion M and the trap frequency ω_{tr} . Inserting the scaled equilibrium positions [35] one finds a distance of $\Delta = 5.6 \mu\text{m}$ between two $^{40}\text{Ca}^+$ ions in a two ion crystal at a trap frequency of $\omega_{tr} = 2\pi \cdot 1 \text{ MHz}$ and a distance of $\Delta = 4.8 \mu\text{m}$ between each of the three ions in a three ion crystal at the same trap frequency. For larger ion numbers the distance between adjacent ions decreases further; additionally the distance between ions in the centre of the trap is smaller than the distance between ions at the ends of the ion string. This is due to the ions assuming equilibrium positions in the combined potential of the trap and the Coulomb potential of the other ions comprised in the chain.

2.2. Atom-light-interaction

Quantum information processing with single ions can only be performed if the ions can be trapped and manipulated reliably. Both is done via interactions with electro-magnetic fields. The following treatment discusses the time evolution of trapped ions subjected to light fields. Ions are trapped in the electric potential of a Paul trap, which was described in the previous section. The potential of the Paul trap is a three-dimensional harmonic potential. In the following, the atom-light interaction of a single particle in a one-dimensional harmonic potential will be discussed, as the three-dimensional potential can be described by three linearly independent one-dimensional harmonic potentials in each of the three directions.

The Hamiltonian of a single ion in a one-dimensional harmonic trap consists of the ion's kinetic energy $E_{\text{kin}} = \hat{p}^2/2m$ and its potential energy $V = m\omega_{tr}^2\hat{x}^2/2$, where m is the mass of the ion and ω_{tr} is the frequency of the harmonic trap. The position and momentum operators can be expressed by the so called annihilation and creation operators, developed by *Paul Dirac* [36], in the following way

$$\hat{x} := \sqrt{\frac{\hbar}{2m\omega_{tr}}} (\hat{a}^\dagger + \hat{a}) \quad \text{and} \quad (2.9)$$

$$\hat{p} := i\sqrt{\frac{\hbar m\omega_{tr}}{2}} (\hat{a}^\dagger - \hat{a}) \quad . \quad (2.10)$$

Applying the annihilation operator \hat{a} to a state of the harmonic oscillator annihilates an excitation and applying the creation operator \hat{a}^\dagger creates an excitation. The excitations in the harmonic potential are also called phonons. The number of phonons present in the trap corresponds to the expectation value of the phonon number operator $\hat{n} = \hat{a}^\dagger\hat{a}$. With these relations the Hamiltonian of the ion in the harmonic trap can be expressed as

$$\hat{H}_0 = \hbar\omega_{tr} \left(\hat{n} + \frac{1}{2} \right) \quad . \quad (2.11)$$

In the following discussion the electronic structure of the ion is assumed to be a two level system with ground state $|S\rangle$ and excited state $|D\rangle$ ¹. This electronic structure leads to the term $H_A = \hbar\omega_A\sigma_z/2$ in the Hamiltonian. Thus, one arrives at the energy level structure depicted in Figure 2.2 a.

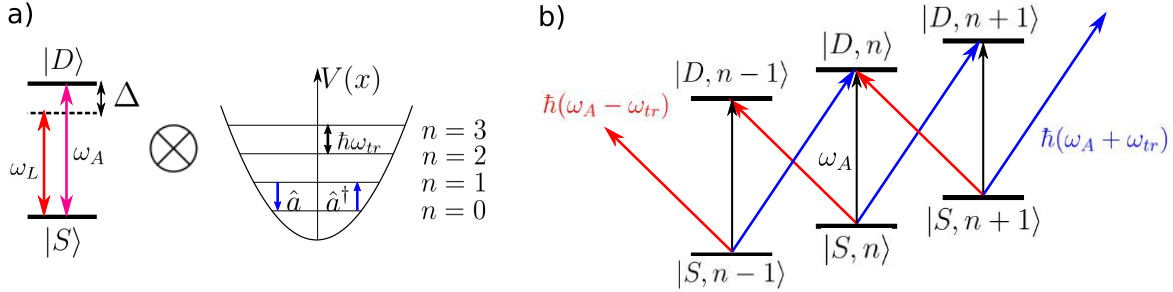


Figure 2.2.: (a) Level structure of a two level system with transition frequency ω_A and level structure of a one-dimensional harmonic oscillator with level spacing $\hbar\omega_{tr}$. (b) Level structure of the combined system. In this configuration the atom can undergo different transitions to change from the ground state $|S\rangle$ to the excited state $|D\rangle$.

The combined Hamiltonian of the atom confined in the trap illuminated by a monochromatic laser field is given in the interaction picture using the rotating wave approximation as [28]

$$H_I = \frac{\hbar\Omega}{2}\sigma_+e^{-i\Delta t} \cdot e^{i\eta[ae^{-i\omega_{tr}t} + a^\dagger e^{i\omega_{tr}t}]} + h.c. \quad . \quad (2.12)$$

In this expression Ω denotes the Rabi frequency, which characterises the strength of the interaction of the light field with the atomic transition; it is proportional to [35]

$$\Omega \propto |\vec{E}| \quad . \quad (2.13)$$

Here, \vec{E} is the electric field of the laser. Further, σ^\pm are the atomic raising and lowering operators, Δ is the detuning between the atomic transition frequency ω_A and the light frequency ω_L and η is the Lamb-Dicke parameter defined as

$$\eta := kz_0 = k\sqrt{\frac{\hbar}{2m\omega_{tr}}} \quad (2.14)$$

with k being the wavevector of the laser field, z_0 the size of the ion's ground state wavepacket in the harmonic oscillator and the mass of the ion m . Therefore, the Lamb-Dicke parameter compares two length scales, namely the size of the ion and the wavelength of the laser beam. If the extent of the ion's wavefunction is much smaller than the wavelength of the laser, one can

¹The labelling ensures consistency with the electronic states of the $^{40}\text{Ca}^+$ ion used in the experiment described in Chapter 3.

2. Theoretical framework

perform the so called Lamb-Dicke approximation [37]

$$\eta^2(2n + 1) \ll 1 \quad , \quad (2.15)$$

with the phononic excitation number n . The square of the Lamb-Dicke parameter is proportional to the recoil energy of a photon imparted onto the ion and antiproportional to the energy spacing in the harmonic oscillator as can be seen by squaring Eq. 2.14. Thus, the Lamb-Dicke approximation essentially states, that the photon's recoil is small enough such that transitions changing the phononic quantum number by more than one excitation are suppressed. Applying this approximation

$$e^{(i\eta[ae^{-i\omega_{tr}t} + a^\dagger e^{i\omega_{tr}t}])} \approx 1 + i\eta [ae^{-i\omega_{tr}t} + a^\dagger e^{i\omega_{tr}t}] + \mathcal{O}(\eta^2) \quad (2.16)$$

and assuming $\Delta = 0$ the interaction Hamiltonian reduces to

$$H_{\text{car}} = \frac{\hbar\Omega}{2}(\sigma_+ + \sigma_-) \quad . \quad (2.17)$$

This Hamiltonian describes transitions which do not change the phononic quantum number of the atom in the trap; those carrier transitions are drawn in black in Figure 2.2 b. Assuming the initial wavefunction $c_n(t) |S, n\rangle + d_n(t) |D, n\rangle$ and inserting it into the time-dependent Schrödinger equation with the interaction Hamiltonian from Eq. 2.17 leads to an excited state occupation in the phononic ground state of

$$p_D = |d_0(t)|^2 = \sin^2\left(\frac{\Omega t}{2}\right) = \frac{1}{2}(1 - \cos(\Omega t)) \quad (2.18)$$

which is depicted in Figure 2.3.

For the derivation of Eq. 2.18 it was assumed that the ion is in the motional Fock state with phonon number zero. In general the ion will be in a thermal mixture of states with different phonon numbers. A formula for the excited state population in such a mixture has been derived in Ref. [28]. It is given as

$$p_D = \frac{1}{2} \left(1 - \frac{\cos(\Omega t) + (\Omega \bar{n} \eta^2 t) \sin(\Omega t)}{1 + (\Omega \bar{n} \eta^2 t)^2} \right) \quad (2.19)$$

with the mean phonon number \bar{n} and the Lamb-Dicke parameter η .

Setting the detuning of the laser light equal to the trap frequency of the harmonic oscillator, i.e. $\Delta = \omega_{tr}$, leads to the Hamiltonian

$$H_+ = \frac{i\hbar\Omega\eta}{2}(\sigma_+ a^\dagger - \sigma_- a) \quad (2.20)$$

describing interactions where one phononic excitation is assigned to the atom while it is transferred into the excited state; those transitions are drawn in blue in Figure 2.2 b and are

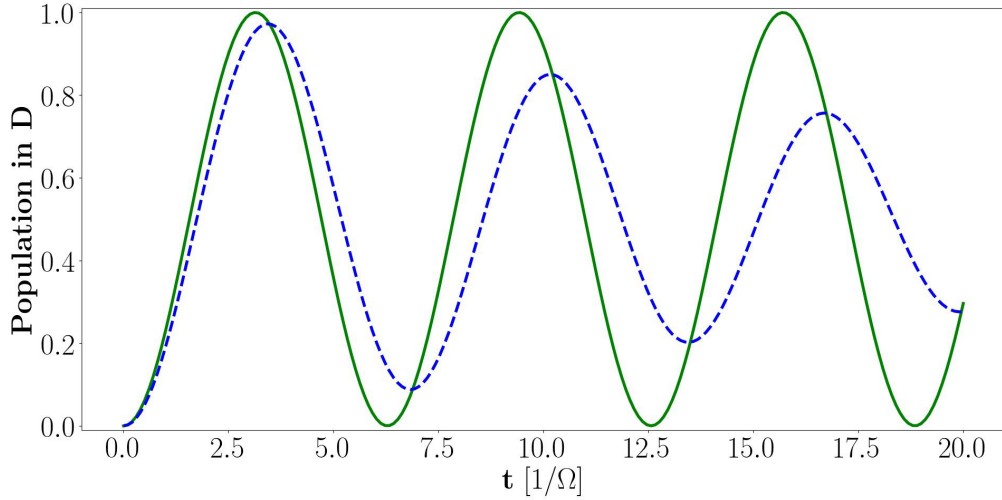


Figure 2.3.: Plot of the excited state population of a two-level ion illuminated by on-resonant monochromatic laser light. The green line shows the occupation of the excited state in a motional Fock state according to Eq. 2.18. The blue dashed line shows an ion oscillating at the same Rabi frequency, but in a harmonic trap with a phononic excitation of $\bar{n}\eta^2 = 0.1$ according to Eq. 2.19.

called blue sideband transitions. Further, setting $\Delta = -\omega_{tr}$ leads to

$$H_- = \frac{i\hbar\Omega\eta}{2}(\sigma_- a^\dagger - \sigma_+ a) \quad (2.21)$$

describing interactions where one phononic excitation is removed from the atom while it is transferred into the excited state; those transitions are drawn in red in Figure 2.2 b and are called red sideband transitions.

The red sideband transitions are used to cool the ions into the motional ground state of the trap. Additionally, red and blue sideband transitions are employed to entangle several ions in one trap via their shared motional state. More details about the sideband transitions and how they are used for cooling the particles can be found in Ref. [28]; entanglement of the ions using those transitions is described in Ref. [38].

2.3. Quantum computation

In a quantum computer, information is stored in qubits, which are quantum mechanical two-level systems. Those qubits are the equivalent to bits in a classical computer. Classical bits can be in two distinct states, either 0 or 1, whereas qubits can be in any complex superposition of the two states $|0\rangle$ and $|1\rangle$ with norm one. Thus, the state of a qubit can be described as a vector on the two-dimensional Bloch sphere, which is depicted in Figure 2.4. Let $|S\rangle$ and $|D\rangle$ be the

2. Theoretical framework

two basis states in \mathcal{H} , then the state of the qubit is completely determined by the wavefunction

$$|\psi\rangle = \sin\left(\frac{\theta}{2}\right) e^{i\phi/2} |S\rangle + \cos\left(\frac{\theta}{2}\right) e^{-i\phi/2} |D\rangle \quad (2.22)$$

with θ being the polar angle and ϕ being the azimuthal angle.

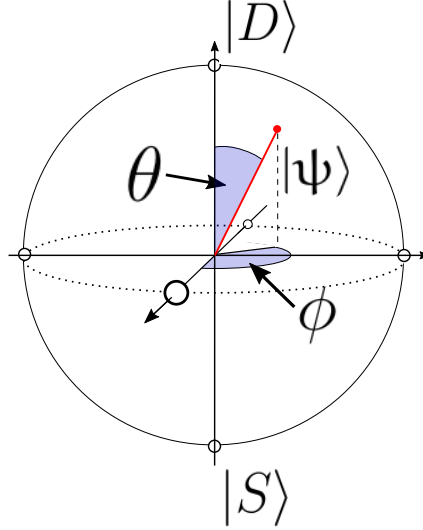


Figure 2.4.: Representation of a state $|\psi\rangle$ on the Bloch sphere. The state $|\psi\rangle$ is completely determined by the two angles θ and ϕ . The poles are given by the two orthogonal states $|S\rangle$ and $|D\rangle$.

Calculations on qubits can be performed by applying quantum gates to them, which are the quantum mechanical counterpart of logical gate operations on a classical computer. The quantum gates are given by unitary operations \hat{U} , which fulfil the following criterion for arbitrary wavefunctions $|\psi'\rangle = \hat{U} |\psi\rangle$:

$$|\langle\psi'|\psi'\rangle|^2 = |\langle\hat{U}|\psi\rangle|^2 \quad \text{for} \quad \hat{U}\hat{U}^\dagger = \hat{U}^\dagger\hat{U} = \mathbb{1} \quad . \quad (2.23)$$

Thus, these gates ensure an evolution of the qubit on the surface of the Bloch sphere [39]. The vector space of these 2×2 unitary matrices is spanned by the Pauli matrices $\sigma_{x,y,z}$ and the unit matrix $\mathbb{1}$:

$$\mathbb{1} = \begin{pmatrix} 1 & 0 \\ 0 & 1 \end{pmatrix}, \quad \sigma_x = \begin{pmatrix} 0 & 1 \\ 1 & 0 \end{pmatrix}, \quad \sigma_y = \begin{pmatrix} 0 & -i \\ i & 0 \end{pmatrix} \quad \text{and} \quad \sigma_z = \begin{pmatrix} 1 & 0 \\ 0 & -1 \end{pmatrix} \quad . \quad (2.24)$$

Thus, all single qubit gates can be described by a combination of rotations on the Bloch sphere

and can be expressed by a combination of those matrices:

$$\hat{U} = e^{i\delta} e^{-i\theta \vec{n} \vec{\sigma} / 2} = e^{i\delta} \left[\cos\left(\frac{\theta}{2}\right) \mathbb{1} - i \sin\left(\frac{\theta}{2}\right) (n_x \sigma_x + n_y \sigma_y + n_z \sigma_z) \right] \quad (2.25)$$

In this expression δ accounts for a global phase, that cannot be measured in a single qubit and \vec{n} is a vector with norm one, which corresponds to the axis around which the state is rotated.

It can be shown that these single qubit gates plus a maximally entangling gate form a universal set of quantum operations, meaning that applying this set of gates to a set of qubits will enable performing any arbitrary unitary operation on them. This set of gates is equivalent to a universal gate set for a classical computer and is partially derived in Chapter 4 of [39]. In 1999 Daniel Gottesmann and Isaac L. Chuang gave the proof of universality for single qubit gates and an entangling gate [40]. In an ion trap quantum computer one possible entangling gate is the Mølmer-Sørensen-gate, which was introduced by K. Mølmer and A. Sørensen in 1999 [26].

In the case of ion quantum computers the quantum gates are implemented via controlled laser pulses whose interaction has been discussed in Section 2.2. Shining a laser pulse resonant to the qubit transition onto the ion leads to a rotation of the qubit's state around the x/y-axis. The corresponding operator is

$$S_\phi(\theta) = e^{-i\theta(\sigma_x \cos(\phi) + \sigma_y \sin(\phi))/2} \quad (2.26)$$

with ϕ and θ as in Fig. 2.4. The rotation angle is $\theta = \Omega t$, where Ω is the coupling between the qubit transition and the laser field as given in Eq. 2.13 and t is the period of time for which the laser field is applied. The axis of rotation ϕ is determined by the phase of the laser field, which is defined for each ion relative to the first pulse applied to it in a given sequence of gates. Far off-resonant laser pulses with a detuning Δ are used to perform rotations around the z-axis via the AC Stark shift $\delta_{ac} = -\Omega^2/(2\Delta)$ [14]. The corresponding operator for this interaction is

$$S_z = e^{-i\theta \sigma_z / 2} \quad (2.27)$$

The rotation angle $\theta = \delta_{ac} t$ is given by the AC Stark shift and the duration for which the laser field is applied. As can be seen from Eq. 2.27, the rotations around the z-axis do not depend on the phase of the light field, which is why they can be introduced to the ions by a second laser, which does not need to have a phase coherence with respect to the laser field applied for rotations around the x/y-axis. Thus, in the current addressing setup in our laboratory those two operations are mediated by two independent laser fields. One of the two fields is applied globally to the string of ions and is used to perform rotations around the x/y-axis and the other laser field can be applied to a single ion at a time and implements the rotations around the z-axis.

For single ion addressing, the laser pulses which are used for the rotations around the z-axis need to be focussed onto individual ions in the crystal. The optics employed for this needs to be able to focus a laser beam down to a size that is smaller than the inter-ion separation in the ion crystal to ensure single ion addressing. This separation is on the order of a few μm in our trap. Further, the optics should ensure, that the addressing beam is guided to the position of the ion. The light propagation through the optics can be described by ray optics and Gaussian optics.

2.4. Ray optics

The framework of ray optics will be used in this thesis to determine the position of laser beams passing through a system of lenses. Ray optics, also called geometric optics, is a theory to describe the propagation of electromagnetic waves through free space and optical elements. In this approximation the wave nature of light is neglected. Thus, light fields can be described as rays obeying geometrical rules.

The direction and position of light rays can be calculated efficiently in ray optics, which is due to the fact, that light rays are easier to track than solving the wave equation. This enables to study phenomena such as image formation. Ray optics relies on Fermat's principle [22]. The principle states, that a light ray will travel along a path in space whose optical length doesn't change under small variations of the path.

$$\delta \int_A^B n(\vec{r}) ds = 0 \quad (2.28)$$

Here, $n(\vec{r})$ is the refractive index of the medium surrounding the ray and δ indicates the variation of the integral [41] along a path from point A to point B. In his treatise *Analysis ad refractiones*, which he published in 1662 [42], Fermat used his principle to deduce the law of reflection

$$\theta = \theta' \quad (2.29)$$

stating that the incident angle of a light ray θ on a surface is equal to the reflected angle θ' . He also obtained the law of refraction, also called Snell's law

$$n_1 \sin(\theta_2) = n_2 \sin(\theta_1) \equiv NA \quad , \quad (2.30)$$

with n_1 and n_2 being the indices of refraction of the incident medium and the medium on the other side of the boundary. The angle θ_1 is spanned between the incident ray and the normal to the boundary, while θ_2 is spanned between the refracted ray and the normal to the boundary. Snell's law and the law of reflection are illustrated in Figure 2.5.

The variable $n \sin(\theta)$ is also known as numerical aperture (NA). It characterises the solid angle of the light cone that an optical system can accept or emit. The NA of a lens is given as

$$NA \approx D/(2f) \quad (2.31)$$

with its diameter D and its focal length f . In the following paragraphs the discussion of ray optics will be limited to the paraxial approximation. In this approximation it is assumed that the light rays form small angles with the optical axis, which is the axis passing through the centre of the optical elements in the setup, leading to the approximation

$$\sin(\theta) \approx \tan(\theta) \approx \theta \quad . \quad (2.32)$$

Therefore, optical components can be understood as linear transformations applied to incoming light rays. Due to the linear dependence of the input angle and position relative to the optical

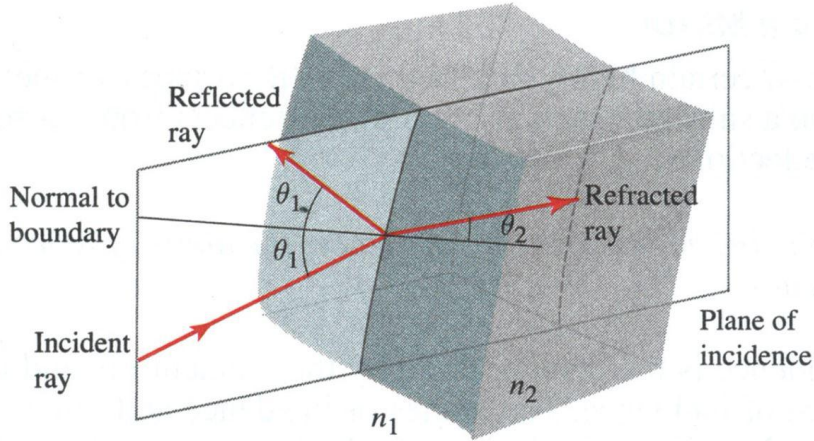


Figure 2.5.: Sketch of the reflection and refraction of an incident ray onto a boundary with a refractive index of n_1 on the side of the incident ray and a refractive index of n_2 on the side of the refracted ray. The reflected and refracted ray lie in the plane of incidence. The illustration was taken from [22].

axis to the output angle and position, optical elements can be modelled as 2×2 matrices, also called ABCD matrices [31]. The action of an ABCD matrix onto an optical ray can be expressed through the equation

$$\begin{pmatrix} y_2 \\ \theta_2 \end{pmatrix} = \begin{pmatrix} A & B \\ C & D \end{pmatrix} \begin{pmatrix} y_1 \\ \theta_1 \end{pmatrix}, \quad (2.33)$$

with, $\theta_{1,2}$ being the angles between the ray and the optical axis before and after the optical element respectively and $y_{1,2}$ being the radial distances of the rays to the optical axis.

Paraboloidal surfaces have the property that all rays impinging on them parallel to the optical axis are focused on a single point

$$f = \frac{ROC}{2}, \quad (2.34)$$

where ROC denotes the radius of curvature of the surface²; f is called the focal length of an optical element. Due to the small angles of light rays to the optical axis assumed in the paraxial approximation, the radial position of the rays relative to the optical axis is small enough, such that spherical boundaries can be approximated by such paraboloids [22]. For thin lenses the paraxial approximation is always fulfilled, since those are optical elements with ROC much larger than their thickness. Therefore, a thin lens can be characterised by its focal length only. The most important ABCD-matrices for this thesis are those for free space and for a thin lens, which are shown in Figure 2.6.

Due to the linearity of the optical elements, a combination of N optical elements can be

²The ROC of a 2D surface in cartesian coordinates parametrised as a curve $y(x)$ is given as $ROC = (1 + y'(x)^2)^{3/2} / y''(x)$

2. Theoretical framework

expressed by a single ABCD-matrix M

$$M = M_N M_{N-1} \dots M_2 M_1 \quad . \quad (2.35)$$

Here, the indices indicate the order in which the light ray passes through elements with one being the first element and N being the last.

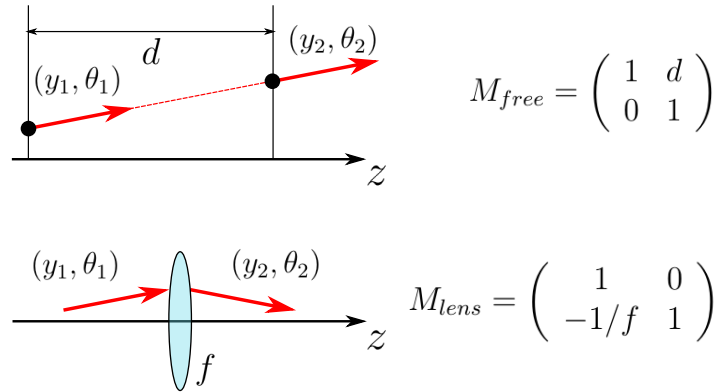


Figure 2.6.: Most common ABCD-matrices. The upper scheme shows the transformation of a light beam after a free space propagation of distance d . According to Eq. 2.33 the propagation can be expressed through M_{free} . The lower scheme shows the propagation of a light beam through a thin lens, which only changes the angle of an incoming beam. Thus, the transfer matrix of a thin lens is given as M_{lens} .

In an ion trap quantum computer the positions of the laser beams need to be matched to the positions of the ions in the trap to ensure maximum interaction between laser and ion. The position of a laser beam passing through an optical setup can be calculated using the formulas presented in this section. Further, ray optics gives a good framework for estimating aberrations of optical elements. Nevertheless, the spot size of a laser beam may be limited by diffraction, which is not taken into account in ray optics. This can be investigated using Gaussian optics, which is outlined in the following section.

2.5. Gaussian optics

Ray optics breaks down if light passes through or around objects whose dimensions are on the order of the light's wavelength [22]. It does not predict the correct field distribution if light is focussed to a spot size comparable to its wavelength. This becomes apparent, when considering the light distribution in the focal plane of a lens. In ray optics the spot is infinitesimally small, which is non-physical, since this violates the Abbe criterion [43]. This is because ray optics doesn't take the wave nature of light into account and thus neglects diffraction and interference effects.

Gaussian optics is the paraxial approximation to the wave nature of light fields, which is essentially governed by Maxwell's equations. These equations lead to a wave equation whose spatial and time-dependent part can be separated from each other [22]. The spatial part is governed by the Helmholtz equation:

$$\Delta U(\vec{r}) + k^2 U(\vec{r}) = 0 \quad (2.36)$$

with the wavevector k and the field amplitude $U(\vec{r})$. One solution of this wave equation are spherical waves $U(\vec{r}) = U_0 e^{ikr}/r$. Performing the paraxial approximation given in Eq. 2.32 to the spherical waves will lead to Gaussian beams. This approximation is illustrated in Figure 2.7.

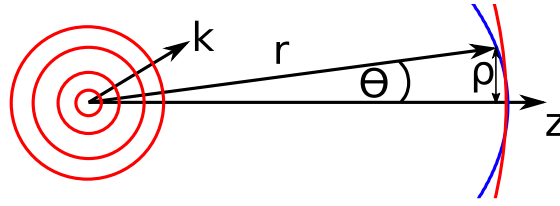


Figure 2.7.: Illustration of the Gaussian approximation. A spherical wave (red wavefronts) is approximated by a paraboloidal wavefront (blue). This approximation is valid for small angles θ or equivalently small distances from the optical axis $\rho = \sqrt{x^2 + y^2} \ll z$.

The paraxial approximation can be applied to the Helmholtz equation by assuming the solution $U(\vec{r}) = E(\vec{r})e^{ikz}$, where $E(\vec{r})$ is a slowly varying envelope, i.e. it changes slowly in z -direction compared to the changes in x - and y -direction. This approximation is compliant with the paraxial approximation performed in Sec. 2.4 in the sense that angles relative to the optical axis are small. Due to the slow change of $E(\vec{r})$ in z -direction, its second derivative with respect to z can be omitted. Inserting the approximated $E(\vec{r})$ into Eq. 2.36 results in the paraxial Helmholtz equation,

$$i\partial_z E(\vec{r}) + \frac{1}{2k}(\partial_x^2 + \partial_y^2)E(\vec{r}) = 0 \quad . \quad (2.37)$$

This equation is solved for

$$E(\vec{r}) = \frac{E_0}{q(z)} e^{\frac{ik\rho^2}{2q(z)}} \quad , \quad (2.38)$$

which exhibits paraboloidal wavefronts. Here, ρ is the distance from the z -axis and $q(z)$ is a complex function depending only on z . The laser light used in the laboratory can be described by Gaussian beams, because those are the eigenmodes of SM fibres and optical resonators used to guide laser light. Gaussian beams are versions of Eq. 2.38, where

$$q(z) = z - iz_R \quad (2.39)$$

2. Theoretical framework

with

$$z_R = \frac{\pi w_0^2}{\lambda} \quad (2.40)$$

being the Rayleigh range. The parameter w_0 denotes the waist in the focus of the beam, i.e. its minimum waist. The function $q(z)$, also called complex q-parameter, can be divided into real and imaginary part

$$\frac{1}{q(z)} = \frac{1}{R(z)} + \frac{i\lambda}{\pi w^2(z)} \quad (2.41)$$

with $R(z)$ being the phase front radius of curvature of the beam, λ being its wavelength and $w(z)$ the waist at position z . With this expression the Gaussian beam can be expressed as

$$E_G(\vec{r}) = E_0 \frac{w_0}{w(z)} e^{-\frac{\rho^2}{w(z)^2}} e^{\frac{ik\rho^2}{2R(z)}} e^{i\phi(z)} e^{ikz} \quad , \quad (2.42)$$

where

$$\phi(z) = \arctan\left(\frac{z}{z_R}\right) \quad . \quad (2.43)$$

is the Gouy phase [22]. In the following paragraphs the physical terms occurring in Eq. 2.42 and how they affect the ion-light coupling will be discussed, those are depicted in Figure 2.8.

Rayleigh range z_R : The Rayleigh range is the range along the optical axis wherein a Gaussian beam is said to be collimated, meaning that the waist diameter increases less than linearly with the propagation distance. It ranges from the position of the waist of the beam to the position where $w(z) = \sqrt{2}w_0$. At a distance of one Rayleigh range away from the beam waist the phase front radius of curvature of the beam is minimal, afterwards it expands like a spherical wave. Therefore, the coupling between ion and light decreases linearly outside of the Rayleigh range.

Beam waist $w(z)$: The beam waist at any position along the optical axis is given by

$$w(z) = w_0 \sqrt{1 + (z/z_R)^2} \quad (2.44)$$

where w_0 is the minimum waist. From expression 2.42 it can be derived, that the waist w_0 corresponds to the radial distance from the optical axis at which the field amplitude has dropped to $1/e$ of its value on the optical axis. This is the position at which the intensity of the beam has dropped to $1/e^2$. Smaller waists enhance the ion-light coupling, since they lead to higher intensities in the centre of the beam. Waists smaller than the inter ion separation are needed to obtain single ion addressing as opposed to addressing multiple ions at once.

Phase front radius of curvature $R(z)$: The phase front radius of curvature is given by

$$R(z) = z(1 + (z_R/z)^2) \quad . \quad (2.45)$$

For distances larger than z_R away from the initial waist, i.e. $z \gg z_R$ the phase front radius of curvature is approximately equal to z , which corresponds to the radius of curvature of a

spherical wave. Therefore using Eqs. 2.40 and 2.44 one arrives at the divergence angle

$$\theta_0 = \arctan\left(\frac{\lambda}{\pi w_0}\right) \approx \frac{\lambda}{\pi w_0} \quad , \quad (2.46)$$

which is the half-angle of the beam cone outside the Rayleigh range. Here, the beam cone spans the area of the beam where its intensity is larger than $1/e^2$ of its peak intensity.

Gouy phase $\phi(z)$: The Gouy phase arises due to the finite extent of the beam, which introduces a momentum spread in x- and y-direction [44]. At the position of the waist of the beam it gives the phase difference between a spherical wave and a Gaussian beam.

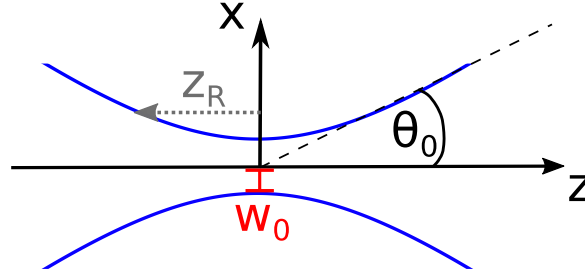


Figure 2.8.: Profile of a Gaussian beam along the optical axis around the waist position. The blue line is the waist function $w(z)$. The black dashed line approximates the waist in the far field and encloses the divergence angle θ_0 with the optical axis. The minimum waist w_0 is drawn in red and the Rayleigh range z_R is the distance along the optical axis at which the beam has a waist of $\sqrt{2}w_0$.

The propagation of a Gaussian beam through optical elements on the optical axis can also be expressed using the ABCD formalism presented in the last section. This can be seen by using $z = y/\tan(\theta) \approx y/\theta$ with y being the distance from the optical axis and substituting $z \rightarrow q(z)$. Thus, the complex q-parameter transforms as

$$q_2 = \frac{Aq_1 + B}{Cq_1 + D} \quad . \quad (2.47)$$

This transformation rule shows that lenses focus Gaussian beams differently than optical rays. This difference can be expressed in the modified thin lens formula for Gaussian beams [45]

$$\frac{1}{s + z_R^2/(s - f)} + \frac{1}{s'} = \frac{1}{f} \quad , \quad (2.48)$$

where the input beam waist lies at a distance s in front of the lens and the output waist is formed at a distance s' behind the lens. Also the size of the output waist can be analysed using Eq. 2.47. It is related to the input waist via

$$w'_0 = w_0 \frac{1}{[(1 - (s/f)^2) + (z_R/f)^2]^{1/2}} \quad . \quad (2.49)$$

2. Theoretical framework

Until now only the lowest order Gaussian beam has been discussed. It shall be noted here that the paraxial Helmholtz equation also allows for other solutions which show the same transformation rule as the Gaussian beam discussed here but have a larger divergence angle θ_0 . Often laser beams in the laboratory are not perfectly Gaussian due to optical aberrations. They consist of those higher order modes as well, which leads to higher divergence. The loss in beam quality can be quantified by the beam parameter product M^2

$$M^2 = \frac{\theta_{real}}{\theta_0} \quad , \quad (2.50)$$

which is the ratio of the divergence angle of the real beam θ_{real} to the divergence angle of a perfect Gaussian beam θ_0 . It is exactly one for Gaussian beams and greater than one for non-perfect Gaussian beams, indicating that higher order Gaussian beams cannot be focused as tightly as zeroth-order Gaussian beams [31].

3. Experimental setup

In this chapter the main components of the experiment necessary for the measurements in Chapter 5 are described. A more complete description of the whole experimental setup can be found in Refs. [33, 46]. An overview of the trapping chamber in which the ions reside is given in Figure 3.1. The transitions that are driven on the ion by the lasers depicted in this figure are outlined in Section 3.1. The following Section 3.2 is used to describe the methods used for imaging the ions, which enables detecting their quantum state. The last two sections are devoted to the study of the current and the new setup of the 729 nm beam path; the laser used to perform quantum gates on the ions.

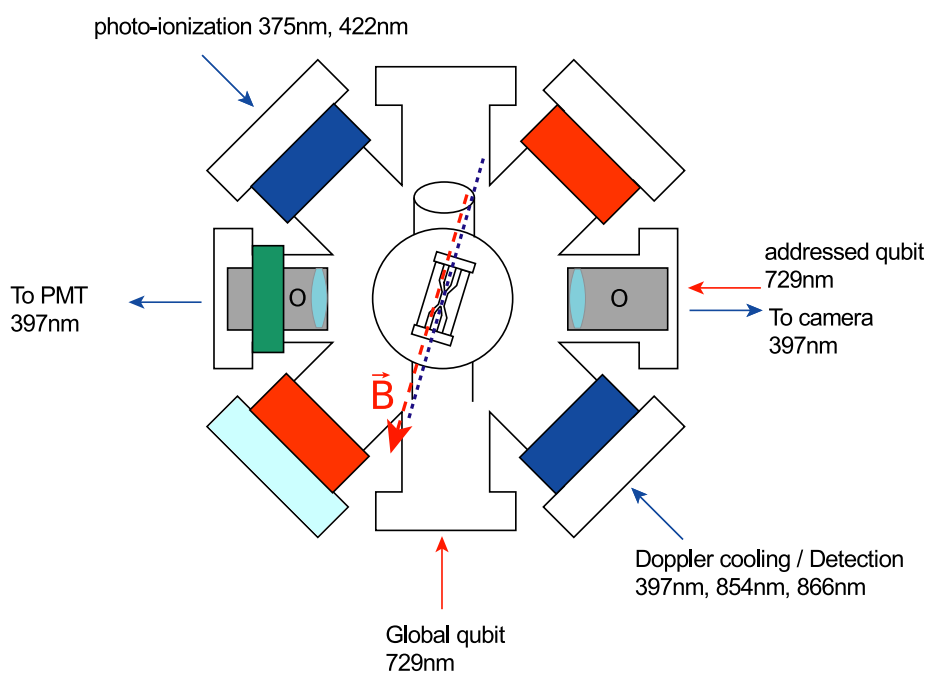


Figure 3.1.: Layout of the trap chamber. The directions from which the laser beams enter the trap chamber are indicated with solid arrows. A magnetic field along the z-axis of the trap defines the magnetic quantisation axis for the ions in the Paul trap, which resides in the centre of the trap chamber. The scheme was adapted from [46].

3. Experimental setup

3.1. The $^{40}\text{Ca}^+$ ion

In the presented experiment we use $^{40}\text{Ca}^+$ ions confined by the potential of a Paul trap to perform quantum information processing. In Figure 3.2 all the relevant transitions needed to achieve this are depicted.

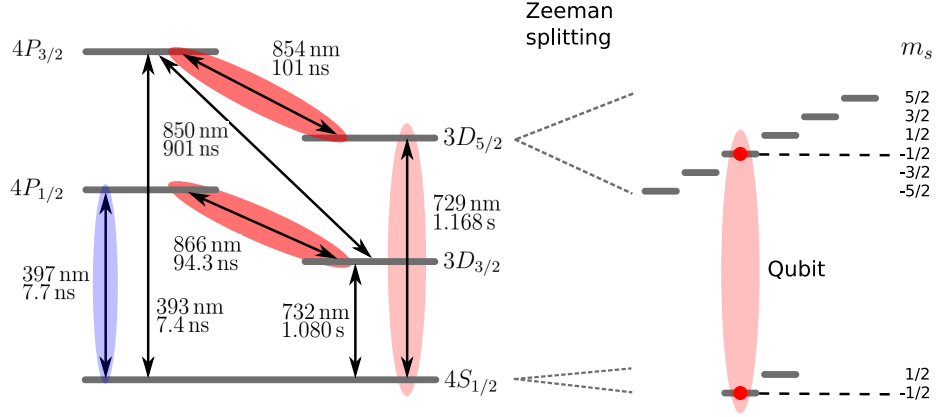


Figure 3.2.: Level scheme of the $^{40}\text{Ca}^+$ ion with all relevant transitions. Transitions driven with laser beams in the lab are highlighted. The wavelength and lifetime of each transition is given, where the values are taken from Refs. [35, 47].

Two lasers with wavelengths at 422 nm and 375 nm are used to ionise neutral calcium atoms, such that they can be trapped by the electric fields of the Paul trap. This optical ionisation method enables isotope selective loading.

Doppler cooling is performed with a laser tuned below the $4S_{1/2} \leftrightarrow 4P_{1/2}$ transition at 397 nm. This transition is used for Doppler cooling due to its broad linewidth of $\Gamma \sim 20$ MHz, which enables fast cooling. The atom in the $4P_{1/2}$ state can decay into the $3D_{3/2}$ state with a branching fraction of 6% [48]. Therefore, the ion is illuminated with 866 nm light during Doppler cooling to pump the $3D_{3/2}$ excitation back into the cooling cycle. With the linewidth of the cooling transition $\Gamma \sim 20$ MHz and typical trap frequencies of $\omega_{tr} \sim 1$ MHz we achieve mean phonon numbers of $\bar{n} \sim 10^1$. Doppler cooled ions can be used to determine the coupling strength between light field and atom according to Eq. 2.19, which allows us to infer the coupling strength as well as the mean phonon number from measured excited state populations. Nevertheless, phononic excitations lead to damped Rabi oscillations, as was shown in Fig. 2.3. For reducing the mean phonon number further, another cooling technique needs to be employed.

One such technique for cooling below the Doppler limit makes use of the atom's sidebands in the harmonic trap, which is why it is called sideband cooling. For sideband cooling the

¹Using the relation $\frac{\hbar\Gamma}{2} = \hbar\omega_{tr} \left(n + \frac{1}{2} \right)$, where the left hand side is the Doppler cooling limit [28]

transition between the $|4S_{1/2}, m_J = -1/2\rangle$ ground state level and the $|3D_{5/2}, m_J = -5/2\rangle$ excited state magnetic sublevel is driven. These magnetic sublevels have been chosen for the cooling process since the addressing of the transition between them reduces the probability to transfer the population into the $|4S_{1/2}, m_J = +1/2\rangle$ ground state, i.e. out of the cooling cycle. During sideband cooling the $3D_{5/2} \leftrightarrow 4P_{3/2}$ transition is driven simultaneously to the $4S_{1/2} \leftrightarrow 3D_{5/2}$ transition with a laser at 854 nm for resetting the ion into the $4S_{1/2}$ state. This process is depicted in Figure 3.3. Just like during Doppler cooling, the laser at 866 nm is used to pump excitation from $3D_{3/2}$ back into the cooling cycle.

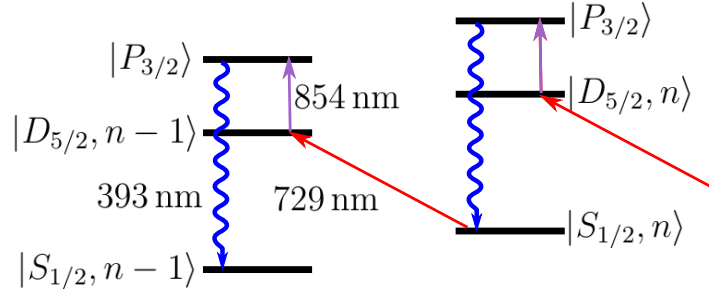


Figure 3.3.: Level scheme and transitions employed in the $^{40}\text{Ca}^+$ ion for sideband cooling. The 729 nm laser is narrow enough to resolve the sidebands on the $4S_{1/2} \leftrightarrow 3D_{5/2}$ transition. An additional laser at 854 nm is used to pump the ion back into the groundstate via the $|P_{3/2}\rangle$ level.

The $4S_{1/2} \leftrightarrow 3D_{5/2}$ quadrupole transition with magnetic quantum number $m_J = -1/2$ for the ground and excited state is chosen for the qubit transition due to its long lifetime of 1.168 s [47]. The choice of these specific Zeeman sublevels is due to the fact that the transition frequency on $m_J = \pm 1/2$ is least sensitive to magnetic field fluctuations which reduces the decoherence of the qubit owing to those fluctuations.

Readout of the quantum state of the qubit is done by driving the $4S_{1/2} \leftrightarrow 4P_{1/2}$ transition while performing optical pumping on the $4P_{1/2} \leftrightarrow 3D_{3/2}$ transition. This results in a closed cycling transition leading to fluorescence if the ion is in the qubit state $|S\rangle$ and no fluorescence if it is in the qubit state $|D\rangle$. The fluorescence light can be detected with a photo multiplier tube (PMT) and an electron multiplying CCD (EMCCD) to determine the quantum state of the ion as will be explained in the following section. This detection method is also called the electron shelving technique [11].

3.2. Detection of the qubit state

The state of the ions is detected by illuminating them with a laser at a wavelength of 397 nm and using the electron shelving technique as described in Section 3.1. Recording the fluorescence

3. Experimental setup

light emitted by the ions results in a measurement of the quantum state projecting it onto the σ_z -axis on the Bloch sphere [38].

3.2.1. PMT

The PMT is used to count the number of photons emitted by the ion string during the electron shelving procedure. Prior to using the PMT for detecting quantum states of the ions, the thresholds for detecting a certain number of ions in the $|S\rangle$ -state need to be defined manually as indicated by the red dashed line in Figure 3.4 in the case of a single ion.

The number of photons detected by the PMT is used to determine how many of the ions are in the $|S\rangle$ -state and how many of them are in the $|D\rangle$ -state. Thus, in a two-ion crystal the PMT can distinguish the states $|SS\rangle$, $|DD\rangle$, but cannot assign which ion is in the $|S\rangle$ -state when only one of them is fluorescing. For the third case the EMCCD needs to be employed to distinguish between the two possible states $|SD\rangle$ and $|DS\rangle$.

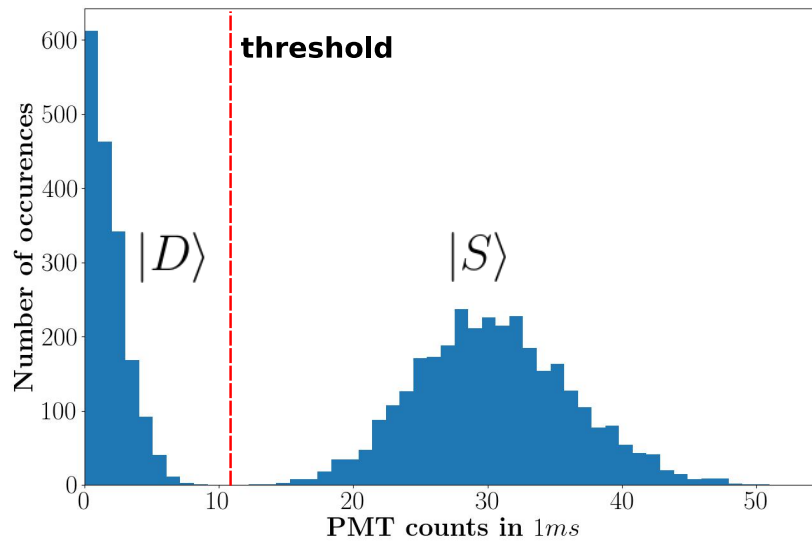


Figure 3.4.: The counts of the PMT for consecutive measurements of a single ion after illuminating it with pulses of 729 nm light of varying length are plotted in the histogram. The red dashed line separates the measurements which yield the $|D\rangle$ -state from those measurements yielding the $|S\rangle$ -state. The position of this line is chosen manually before the measurements and is adjusted to the PMT counts. The measurements shown here were taken with the M-ActION box which is described in detail in [49].

In the experiments described in Chapter 5 the PMT is used to perform measurements of the σ_z -operator. A single measurement will always project onto the state $|S\rangle$ or $|D\rangle$. Therefore,

each experiment is repeated N times resulting in N measurement outcomes to determine the expectation value of the σ_z -operator.

The uncertainty on the quantum state is given by the quantum projection noise [50] and can be expressed as

$$\Delta = \max \left(\sqrt{\frac{p_S(1-p_S)}{N}}, \frac{1}{N+2} \right) \quad (3.1)$$

where p_S is the probability to measure the qubit in the $|S\rangle$ -state and the second term is the result of Laplace's rule of succession [51]. It is added to prevent underestimation of the uncertainty in the case when all measurements result in the same outcome. The formula for the quantum projection noise would yield an uncertainty of zero in this case, which is non-physical, whereas the rule of succession takes into account, that the $N + 1^{\text{st}}$ measurement could lead to a different outcome.

3.2.2. EMCCD

The state of the qubits can also be detected using an EMCCD camera. The model that we employ is an Andor iXon Ultra 897 [52] with a pixel size of $16 \mu\text{m}$ and a sensor area of 512×512 pixel. The EMCCD detection has the advantage that the position of bright ions can be resolved, therefore it is able to distinguish between the states $|SD\rangle$ and $|DS\rangle$ in a two ion crystal. Due to a magnification of ~ 80 of the optics guiding the beam to the EMCCD camera, one pixel on the camera corresponds to $\sim 0.2 \mu\text{m}$ in the plane of the ions. Thus, the EMCCD can distinguish between quantum states with the same number of excitations for ion strings with tens of ions as well. For determining the state of an ion string from an image taken with the EMCCD camera, the pixel values are integrated along the y -axis, as is shown in Figure 3.5. Then, the resulting distribution is compared to reference distributions obtained from a reference image with all ions in the fluorescing state taken beforehand. In a two ion crystal the reference image shows both ions in the $|S\rangle$ state, i.e. the state $|SS\rangle$. Integrating this image along the y -axis reveals the positions and brightnesses of both ions. Therefore, the resulting distribution is utilised to infer the four distributions for the states $|SS\rangle$, $|SD\rangle$, $|DS\rangle$ and $|DD\rangle$. Further images are then integrated along the y -axis as well and the resulting distributions are compared to the inferred distributions. The state is then assigned to the state of the reference distribution that has the smallest mean squared deviation from its distribution. A detailed description of this procedure is given in Ref. [14]. The downside of the EMCCD detection is that it takes longer than the PMT detection [38], because more fluorescence needs to be collected. The uncertainty on a series of measurements is determined as described in the previous section.

3. Experimental setup

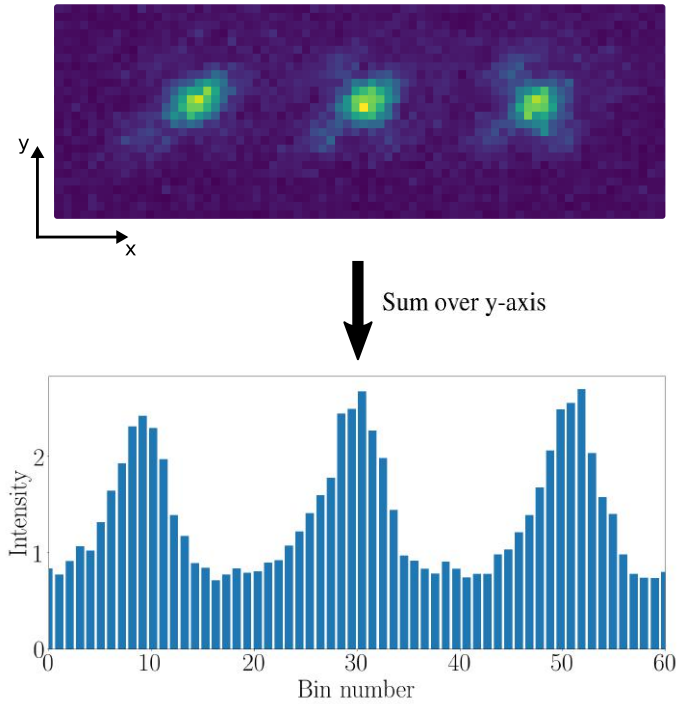


Figure 3.5.: An image of a three ion crystal taken with the EMCCD camera. For state detection, the fluorescence is integrated along the y-axis.

3.3. The existing qubit laser beam path

This section presents the current setup of the 729 nm laser which is used to drive the qubit transition in the $^{40}\text{Ca}^+$ ions. The setup is described in detail in Refs. [53] and [54]. The single ion addressing setup described in Ref. [53] will be exchanged with the setup described in Section 3.4.

The 729 nm light is generated by a continuous wave Ti:Sapphire laser. This laser has an output power of up to 4 W and has a linewidth of below 10 Hz. The light from the Ti:Sapphire laser is guided onto the experiment table in an SM fibre. To ensure a small bandwidth of the laser after passing through the SM fibre, fibre noise cancellation is used as described in Ref. [46]. Behind this setup, the beam is split into two beams, each of which is then guided to a double-pass AOM and coupled into a PM fibre comprising a fibre AOM. The double-pass AOM ensures a high extinction ratio whereas the fibre AOM can be used to produce bichromatic fields, which is needed for performing MS-gates. One of the beams is used as a global addressing beam and enters the Paul trap under an angle of 22.5° relative to the direction of the ion crystal axis, as can be seen in Figure 3.6.

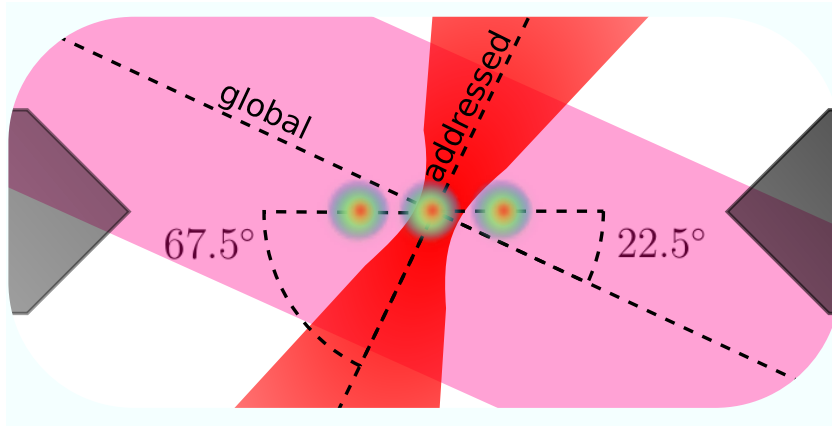


Figure 3.6.: The two laser beams used for manipulating the qubit state of the ions and their respective angles with the ion crystal axis. The global beam has an angle of 22.5° with this axis and the addressed beam enters the trap under an angle of 67.5° .

The global beam is used to drive global x and y rotations on the qubits and for the MS-gate. The other beam is directed onto the ion string at an angle of 67.5° and is used to implement AC-Stark shifts on single ions; this results in rotations around the z axis for individual qubits. The addressing of individual qubits is only possible if the laser beam's focus is sufficiently small and if it is possible to move the beam from one ion to the neighbouring ion. This focussing and moving is obtained through the single ion addressing optics. The optics was implemented by Daniel Nigg and is described in detail in Ref. [53]. The setup is depicted in Figure 3.7.

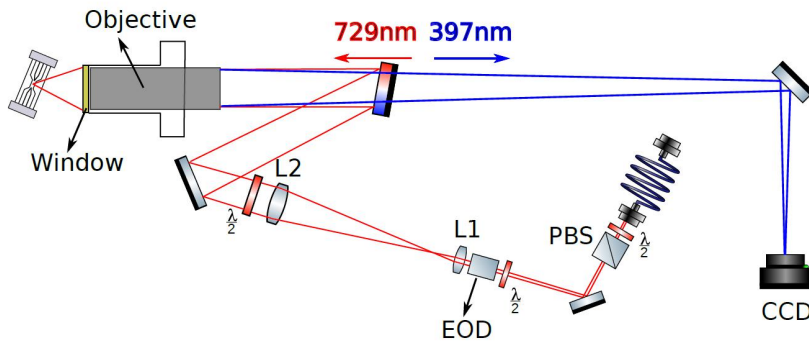


Figure 3.7.: The experimental setup for focussing and moving the addressed beam onto the position of a specific ion. An electro-optical deflector (EOD) is employed to deflect the beam such that it can be focused onto different ions behind the objective. Imaging on the EMCCD is done through the same optical path. The figure was taken from Ref. [53].

The 729 nm beam is launched from a polarisation maintaining fibre. A $\lambda/2$ -waveplate in combination with a polarising beam splitter (PBS) are used to adjust the polarisation of the beam. After the PBS, the beam goes through an electro-optic deflector (EOD) which deflects

3. Experimental setup

the laser beam depending on a dc voltage applied to it. A telescope consisting of the lenses L1 and L2 magnifies the beam by a factor of eight [53]. After the telescope the beam impinges onto a dichroic mirror which reflects light at 729 nm onto the objective². This path is also used for imaging the fluorescence of the ions at 397 nm onto the EMCCD; this wavelength passes the dichroic mirror and is directed onto the camera.

This addressing setup is capable of addressing single ions individually in a string of up to seven ions [53]. As discussed in Ch. 1 this setup can only perform manipulations on a single ion at a time. Further, the single ion addressing beam lacks phase stability to the global addressing beam, which is why solely AC-Stark operations can be applied, yielding single qubit rotations around the z-axis.

In the next section a more versatile setup is presented, which is capable of simultaneous and individual ion addressing. This enables performing rotations around x, y and z and MS-gates on arbitrary subsets of the ion string by only using the single addressing lasers. In this case the global beam is not needed anymore to provide a universal gate set for quantum computing.

3.4. The new 729 nm beam path

In the following, the new path for simultaneously and individually addressing each qubit in the ion string will be discussed. For addressing multiple ions simultaneously and individually each ion needs to be addressed with its own beam. Thus, the single ion addressing setup described in the last section is exchanged by a laser multiplexing setup, i.e. an incoming laser beam is split into several laser beams with the same frequency and the same overall power. The multiplexing setup is shown in Figures 3.8 and 3.12. Those two parts of the setup will be described in the following two subsections.

3.4.1. Fibre optics

For generating multiple laser beams, the incoming laser is coupled into a polarisation maintaining fibre and split into several fibres by utilising fibre beam splitters (FBS)³ ⁴. After the FBS, each beam is guided through a fibre-based AOM⁵ to change amplitude, phase, and frequency of laser pulses for each ion independently. This enables the implementation of arbitrary rotations for each ion individually and simultaneously.

²Silloptics S6ASS2241

³OZ Optics FOBS-12P-111-4/125-PPPPP-729-50/50-40-3A3A3A-1-0.5

⁴OZ Optics FOBS-14P-11111-4/125-PPPPP-729-25/25/25/25-40-3A3A3A3A3A-1-0.5

⁵Gooch & Housego Customized T-M150-0.5C2W-3-F2P with PM fibre at the input and Gooch & Housego Customized T-M150-0.5C2W-3-F2S with SM fibre at the input [55]

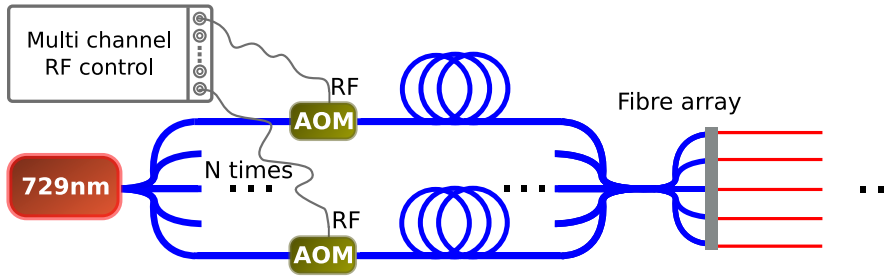


Figure 3.8.: The beam is split by fibre beamsplitters and controlled by fibre AOMs. Each fibre AOM can be steered separately with an RF frequency to change amplitude, phase and frequency of the light passing through it. Behind the fibre AOMs all fibres are aligned in a fibre array, where they are released into free space.

After the fibre AOMs, all the fibres are launched into free space with a fibre array⁶. The fibre array employed in this thesis consists of seven polarisation maintaining fibres with FC/APC connectors at the input and 1.0(1) m length per fibre. Each fibre has a core diameter of $4\ \mu\text{m}$ with a cladding diameter of $125\ \mu\text{m}$. The fibre array is specified to work in a wavelength range of 633 nm–820 nm, and the geometry of the array outputs is given in Figure 3.9.

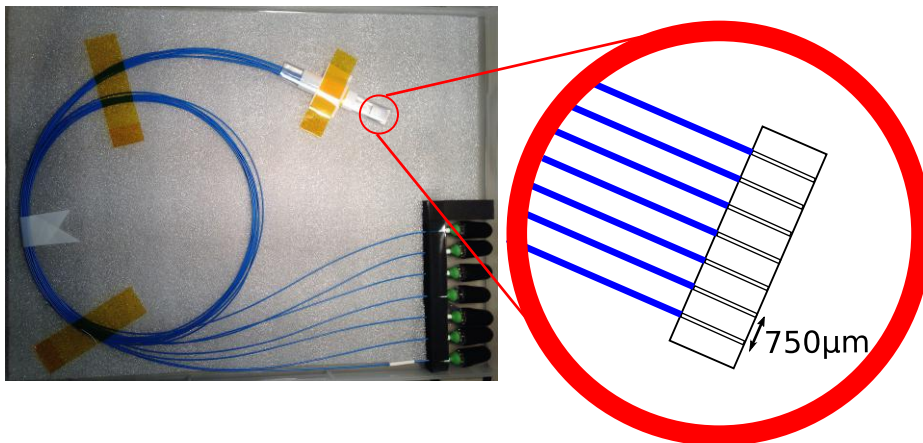


Figure 3.9.: Picture of the fibre array from OZ Optics. Seven fibres can be inserted into the FC/APC connectors in the bottom right corner. The array consists of seven outputs with a distance of $750\ \mu\text{m}$ between each other. This inter-fibre distance is unfavourable for our setup, since beams should be separated by $650\ \mu\text{m}$ to be matched to the free space optics following the fibres. Nonetheless, we used this geometry, because it was the only one that was in stock at that time.

As can be seen in Fig. 3.9, the fibres coming out of the fibre array are separated by $750\ \mu\text{m}$. In

⁶OZ Optics VGA-7-750-0-X-10.3-7.95-2.03-P-633-4/125-3A-1-1-0-SP

3. Experimental setup

fact, a distance of 650 μm between the fibres would better match our optical path, as can be seen in Fig. 3.13. This is why during the work of this thesis we designed a new fibre array, which was fabricated by *SQS-Fiberoptics*. This new fibre array is tailored to the available free space optics and will be introduced in Appendix B.

For well controlled atom-light interaction, the light field interacting with the ions needs a well defined polarisation. As mentioned previously, the fibres in the experiment are polarisation maintaining (PM). The degree of polarisation maintenance is given by the polarisation extinction ratio (PER), which is defined as the ratio of optical powers of perpendicular polarisations. Thus, for conserving the polarisation, the fibre beamsplitters and the fibre AOMs need to have a high PER. A PM fibre has a strong birefringence, such that orthogonal polarisations matched with the two propagation axes follow two independent propagation paths through the fibre. The two axes of the PM fibre are called fast and slow axis and linear polarised light that is coupled into the fibre along one of those axes retains its polarisation after propagating through the fibre.

If a laser is not coupled along one of those axes into a PM fibre, the PER drops and follows the rule $\text{PER} \leq -10 \cdot \log(\tan(2\theta))$ [56] with θ being the angle between the polarisation of the laser beam and one of the two axes of the PM fibre. A misalignment of 6° corresponds to a PER of at most 20 dB and a misalignment of 1.8° corresponds to at most 30 dB. Fibre connectors for PM fibres achieve typical PER of about 20 dB–30 dB [56].

The PER can be influenced by a fibre AOM or a fibre beamsplitter due to mismatch of the propagation axes of the PM fibre at the entrance of the device to the PM fibre at the output. Due to the strong birefringence between the two paths of a PM fibre, the two fractions of the radiation will gain a differential phase at the fibre end, depending on temperature or on bending of the fibre [57]. In case of radiation with sufficient coherence length, the two fractions of radiation will superimpose to an arbitrary elliptical polarisation at the output depending on fibre temperature and mechanical stress. The drifts due to mechanical stress can be reduced by fixating the PM fibre on the optical table; drifts due to temperature are inevitable because of temperature fluctuations in the laboratory.

In the following two paragraphs, measurements of the PER for the fibre-beamsplitters and fibre-AOMs are presented. For the measurement of the PER a linearly polarised laser beam was inserted into the input port of the fibre beamsplitters/AOM and the field on the output port was recorded with a polarisation analyser⁷.

Test of the fibre-beamsplitters

The fibre beamsplitters that were tested in the course of this thesis were manufactured by OZ Optics. They are designed to work at a wavelength of 729 nm and have fibre core diameters of 4 μm with a cladding diameter of 125 μm . Two 1-to-2 splitters and one 1-to-4 splitter were tested. The specified and measured split ratio of the beamsplitters together with the measurement results for the PER are summarised in Table 3.1; Figure 3.10 shows the plot of the results for the 1-to-4 splitter.

⁷Schäfter + Kirchhoff SK010PA and software SK PolarizationAnalyzer

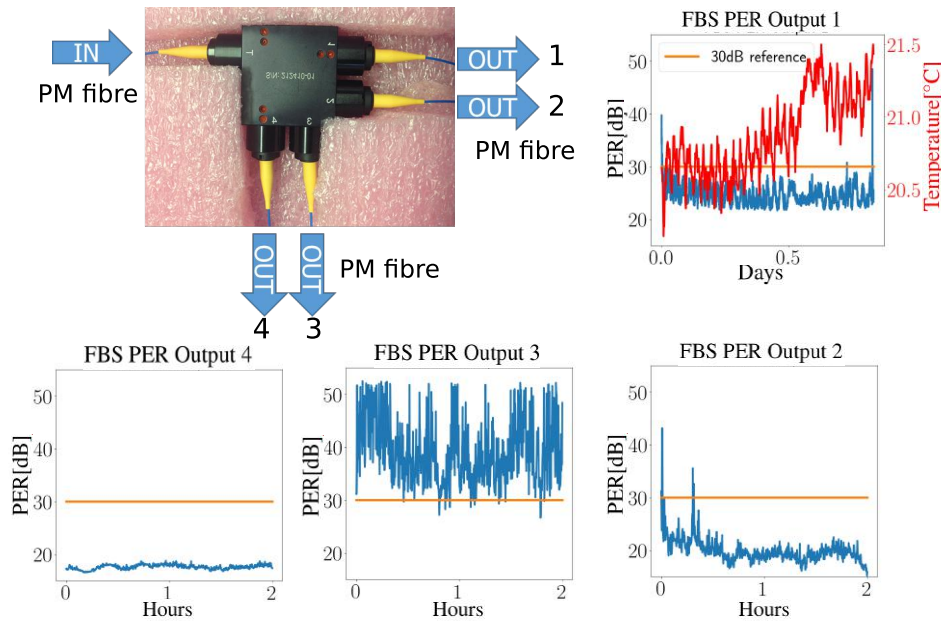


Figure 3.10.: Results for the PER measurement of the 1-to-4 FBS shown in the upper left corner. The plots on the right hand side and below the picture show the corresponding PER for each of the four outputs. The orange line at 30 dB is drawn for reference. Output port one has been measured over a period of 20 hours while the other outputs have been measured over a period of about two hours. For the long measurement, the temperature in the laboratory is plotted as well. The plots show differences between the different output ports.

Each output port from each fibre beamsplitter was recorded for two hours except for port one of the 1-to-4 splitter, which was recorded for 20 hours. During the measurements, the fibres coming out of the beamsplitters were fixated on the optical table, such that they were not subjected to varying mechanical strain, nonetheless the PER of all output ports fluctuated over the course of the measurement. The PER from output port one shows fluctuations on the timescale of 20 min which do not show correlations to the simultaneously measured temperature fluctuations in the laboratory. As can be seen in Table 3.1, different output ports of the FBS show different PER, which can be attributed to misalignments between the propagation axes of input and output fibre in the fabrication process. Nonetheless, each output, except for output four from the 1-to-4 FBS, shows a PER greater than 20 dB. The PER of output three is larger than 30 dB. The fluctuations present in the PER are visible in the data given in Figure 3.10 and are most likely due to temperature fluctuations on the order of 0.6 K in the laboratory, which occur on a similar timescale, as can be seen in the plotted data in this figure. Further the split ratio of the FBSs was measured by comparing the output intensities at each output, those ratios are compared to the ratios given in the specification sheet in Table 3.1. For this measurement the fourth output of the 1-to-4 FBS shows an output power ratio that is much less than specified. This fibre output also showed the worst PER.

3. Experimental setup

Table 3.1.: Properties of the FBS from OZ Optics

Output Port	PER [dB]	split ratio	
		spec. sheet	measured
1-to-2 FBS 1			
1	27(2)	49.6%	51(3)%
2	40(5)	50.4%	49(3)%
1-to-2 FBS 2			
1	28(1)	49.2%	57(3)%
2	28(2)	50.8%	43(3) %
1-to-4 FBS			
1	25(2)	23.5%	26(3)%
2	20(2)	25.5%	27(3)%
3	39(6)	26.5%	30(3)%
4	18(1)	24.5%	17(3)%

Test of the fibre-AOMs

The specifications of the fibre AOMs used in our laboratory are given in [55]. We tested one fibre AOM⁸ with 1.5 m polarisation maintaining fibres⁹ at the input and at the output (PM-PM-AOM) and another fibre AOM¹⁰ with a 1.5 m polarisation maintaining fibre at the output and a 0.5 m singlemode fibre¹¹ at the input (SM-PM-AOM). Both AOMs work at a frequency of 150 MHz and provide rise- and fall-times of 50 ns. The bandwidths of the fibre AOMs were measured to be more than 10 MHz. The losses, operating RF power and PER, which has also been measured in our laboratory are summarised in Table 3.2.

Figure 3.11 shows the PER measurement data from both AOMs, where the strain on the fibres was controlled by fixating them on the optical table under tension. The PER of the SM-PM-AOM shows an average of 43(7) dB over a period of three days while the PM-PM-AOM shows an average PER of 27(7) dB over a period of 20 hours. A reason for the fluctuations in the PER of the PM-PM-AOM could be imperfect alignment of the polarisation maintaining fibres inside the AOM. This effect is decreased by using a shorter singlemode fibre at the output as can be seen from the data obtained from the SM-PM-AOM. The strain on this SM fibre needs to be controlled to minimise fluctuations of the PER. The change in polarisation in the singlemode fibre is less than in the PM fibre, because it creates less birefringence than the PM fibre.

⁸Gooch & Housego Customized T-M150-0.5C2W-3-F2P

⁹Nuferm PM780-HP

¹⁰Gooch & Housego Customized T-M150-0.5C2W-3-F2S

¹¹Nuferm 780-HP

Table 3.2.: Properties of fibre AOMs from Gooch & Housego

Parameters	Units	Limits		Spec.	Measured
		Min	Max		
SM-PM-AOM					
Insertion Loss	dB	N.A.	3	2.3	
Extinction Ratio	dB	50	N.A.	61	
RF Power	W	N.A.	1	1	
PER	dB	N.A.	N.A.	N.A.	43(7)
PM-PM-AOM					
Insertion Loss	dB	N.A.	3	1.3	
Extinction Ratio	dB	50	N.A.	65	
RF Power	W	N.A.	1	0.6	
PER	dB	18	N.A.	18	27(7)

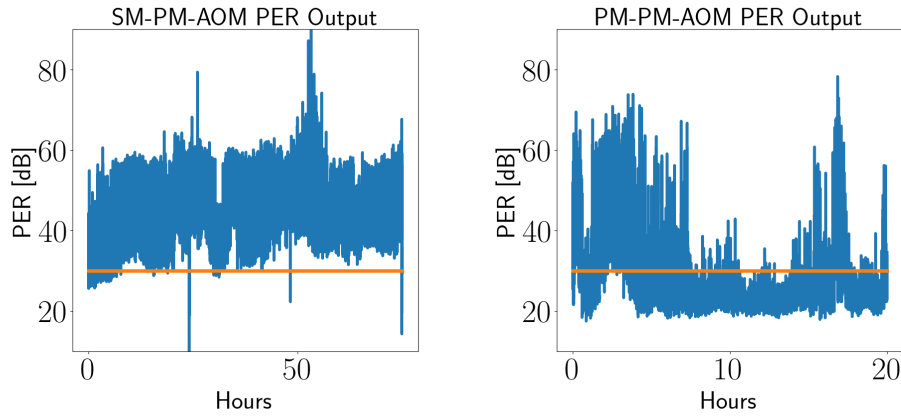


Figure 3.11.: The PER of the two fibre AOMs was measured over a period of three days and one day, respectively. The measured data for the AOM with the singlemode fibre at the output (SM-PM-AOM) is plotted on the left hand side and the data for the AOM with both fibres being polarisation maintaining (PM-PM-AOM) is plotted on the right hand side. The SM-PM-AOM shows a higher PER. The orange line is drawn as a reference at 30 dB.

3.4.2. Free space optics

After the fibre array, a free space optical setup is needed to guide the single lasers modulated by the fibre AOMs onto the positions of the ions. A scheme of this free space optics is given in Figure 3.12.

3. Experimental setup

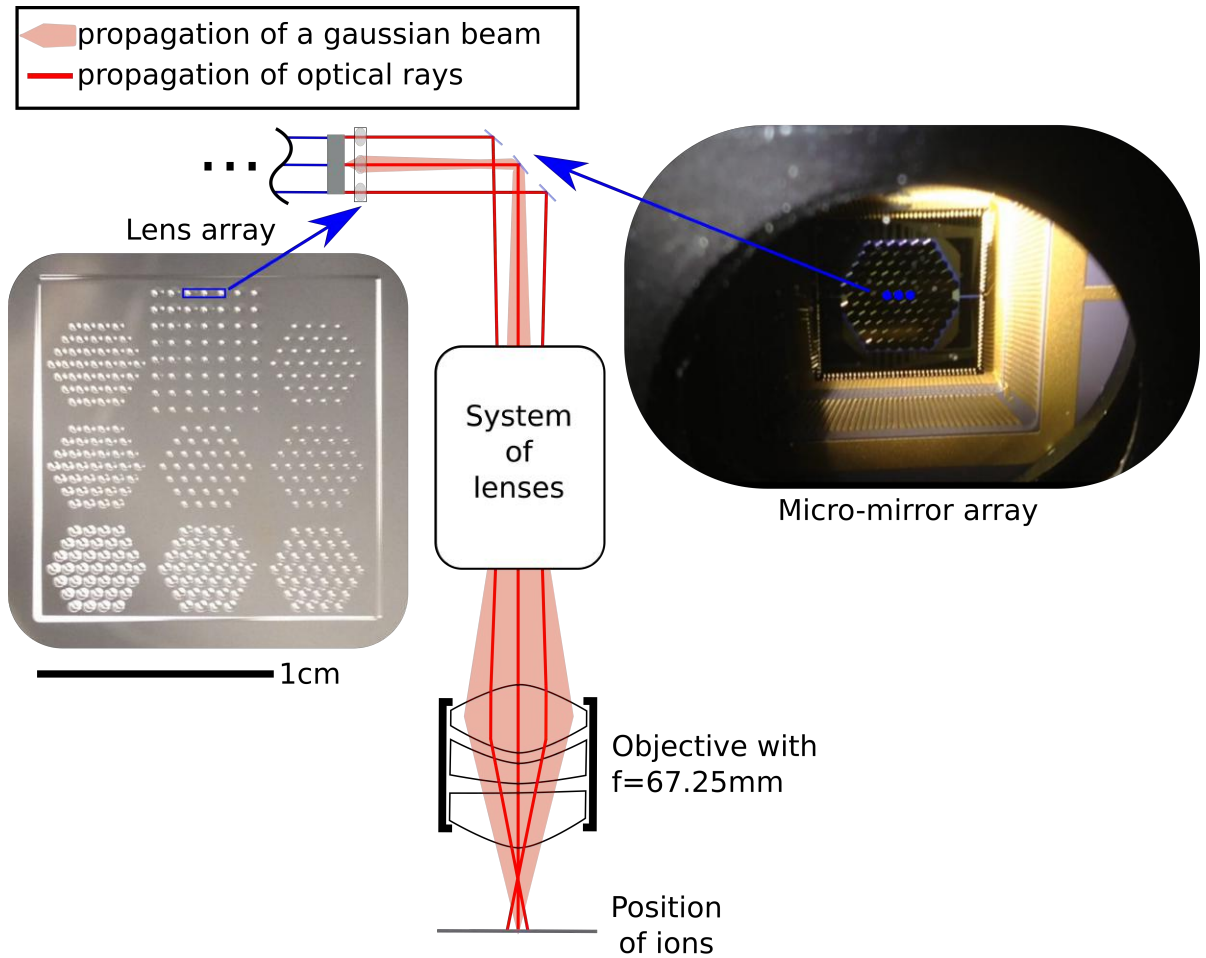


Figure 3.12.: Sketch of the free space optics setup. After leaving the fibre array, each beam is collimated by a lenslet in a lens array. Each collimated beam is deflected by a single mirror of a micro-mirror array. Behind the mirror array a system of lenses is used to expand the beams going onto the objective, which focuses them down onto the positions of the ions. The design of the system of lenses will be discussed in detail in Ch. 4.3. Pilot rays of three beams and the Gaussian beam of the central beam are sketched. The picture on the left hand side shows the lens array, whose design is discussed in Chapter 4.2. The picture on the right hand side shows the front face of the micro-mirror array.

The beams coming out of the fibre array are strongly diverging, therefore a lens is placed in front of each fibre in the array to collimate each beam. The lens array is placed such that each fibre output impinges onto the centre of a lenslet, meaning that the distance between two lenslets is equal to the distance between two fibres. The design of the lens array employed for the measurements presented in Chapter 5 is discussed in Chapter 4.2.

The collimated beams are equidistant and thus need to be adjusted to the unequally spaced ion positions in the harmonic trap for single ion addressing. This equidistant distribution between the fibres can not be altered by transforming the whole array of beams through optical lenses, thus the setup needs to enable manipulation of the individual addressing beams. For this, the beams are directed onto a micro-mirror array (MMA)¹², where each beam hits a single mirror of the array. The configuration of the mirror array is depicted in Figure 3.13; each mirror has a hexagonal shape with a diameter of 650 μm in the horizontal direction and 750 μm diameter in the vertical direction. Each mirror can be tilted up to 3.75 μm with three actuators to provide the decoupling of the positions of the single beams needed for single ion addressing. Single actuators can be steered using a MATLAB program provided from *Boston Micromachines*, which sends electronic signals to a driver that applies voltages of up to 300 V to the actuators.

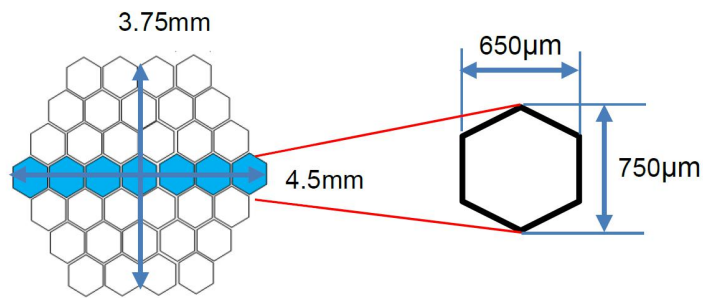


Figure 3.13.: Geometry of the micro-mirror array used in this thesis. Single gold-coated mirrors have a size of 650 $\mu\text{m} \times 750 \mu\text{m}$ and are arranged in a honeycomb structure. The array in our laboratory is customised such that the seven mirrors in the centre (drawn in blue here) can be steered with three actuators each.

The collimated beams need to be expanded to make use of the full aperture of the objective. For this purpose a system of lenses is used which controls the divergence and angles of all beams simultaneously. The design of this system of lenses is discussed in Chapter 4.3. The objective in front of the ions is the same model¹³ as in the old setup.

Deflection of the micro-mirror array

The deflection angle of a single mirror in the MMA determines by which amount the position of the corresponding beam can be changed. Each mirror can be tilted with three actuators by applying a voltage to these actuators.

¹²Boston Micromachines HEX111

¹³Silloptics S6ASS2241

3. Experimental setup

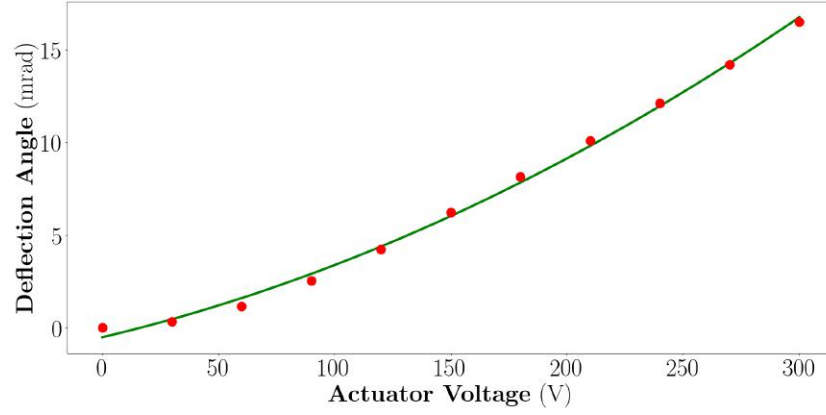


Figure 3.14.: Plot of the deflection angle of a single mirror against the voltage applied to a single actuator of this mirror. The fitted curve shown in green is a quadratic calibration of the deflection angle and is given in Eq. 3.2

Each deflection angle corresponds to a certain voltage applied to the corresponding actuators; the relationship between actuator voltage and tilt angle has been measured for a single actuator and is shown in Figure 3.14. The deflection angle has been calibrated for the applied voltage giving

$$\theta(V_{act.}) = 93(13) \cdot 10^{-6} \frac{\text{mrad}}{\text{V}^2} \cdot V_{act.}^2 + 29.6(4.1) \cdot 10^{-3} \frac{\text{mrad}}{\text{V}} \cdot V_{act.} - 0.50(26) \text{ mrad} \quad , \quad (3.2)$$

where θ is the deflection angle and $V_{act.}$ is the voltage applied to the actuator. For this measurement a CCD laser beam profiler¹⁴ was placed at a distance of 0.21 m behind the MMA and a picture was taken for some actuator voltages. The position of the spot on the screen was determined by fitting a 2D Gaussian

$$I(x, y) = A \cdot e^{-2 \cdot (x-x_0)^2 / \sigma_x^2 - 2 \cdot (y-y_0)^2 / \sigma_y^2} + A_0 \quad (3.3)$$

to the measured data; the actuator voltage was adjusted with the MATLAB software provided by *Boston Micromachines*. Transforming the measured beam displacement into a deflection angle gives a maximum deflection angle of 16.5 mrad.

¹⁴Newport LBP2-HR-VIS2 with resolution $3.69 \mu\text{m} \times 3.69 \mu\text{m}$

4. Optical design and tests

Building an optical setup is time consuming and thus it is advisable to simulate it prior to implementation. Therefore, the setup is simulated using the software ZEMAX OpticStudio and tested in an external setup. Section 4.1 describes the measurement of the beam output of the fibre array, which is needed as an input parameter to the simulation. In Section 4.2 results from the simulations for the lens array used to collimate the beams from the fibre array are presented. The last section of this chapter discusses the simulation of the free space optics, from the fibre array to the focus of the objective and its implementation in a test setup.

4.1. Characterising the output beam of the fibre array

The simulation of the optical setup needs to be informed with the beam parameters from the output of the fibre array. According to Eq. 2.44 the minimum waist of the beam can be determined by measuring the waist at several positions along the optical axis of the beam. For determining the beam waist, a knife edge measurement of one of the output beams from the fibre array is performed.

For this measurement, a razor blade is mounted onto a translation stage with a resolution of $10\ \mu\text{m}$. This blade is placed after the fibre output and moved into the laser beam perpendicular to the propagation axis. For several blade positions the optical power behind the blade is measured with a powermeter. The result of such a measurement series is presented in Figure 4.1. Assuming the profile of the beam to be Gaussian, a Gaussian cumulative distribution function is fitted to the obtained data. This function is given as

$$F(x) = A \cdot \left(1 + \operatorname{erf} \left[\sqrt{2} \cdot \frac{x - \mu}{w_0} \right] \right) \quad (4.1)$$

with an amplitude A , the mean value μ and the Gaussian waist w_0 , which is assumed to be the same in the x - and y -direction, i.e. $w_x = w_y$. Furthermore, the function takes the two-dimensional nature of the underlying Gaussian beam into account¹. The function $\operatorname{erf}(x)$ is called error function, which is defined as the integral of a Gaussian distribution starting from 0 up to the point x . From the fit of the cumulative distribution function, the Gaussian waist of the laser beam at the position of the blade is extracted. The fit is shown in Fig. 4.1.

¹A rigorous derivation of Eq. 4.1 can be found in Ref. [58].

4. Optical design and tests

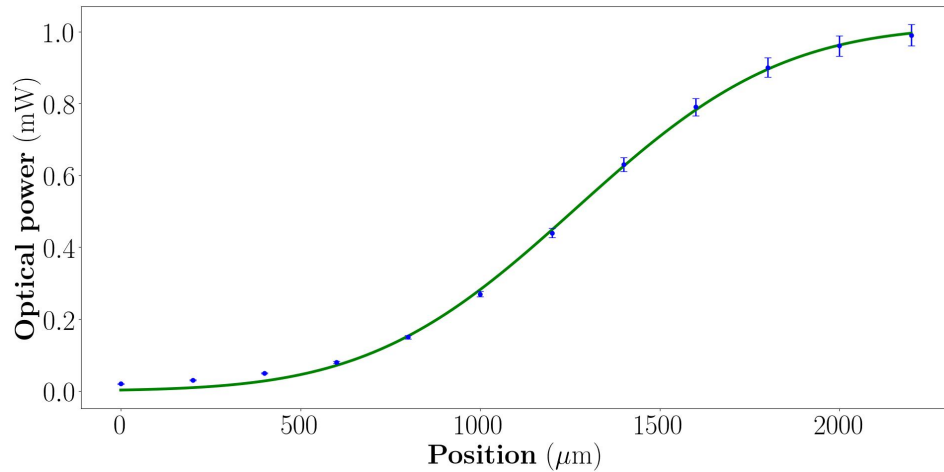


Figure 4.1.: Plot of the measured power on the powermeter as a function of the blade position perpendicular to the optical axis. The measured light intensities resemble the integral of the beam profile. Error bars are obtained from fluctuations on the powermeter, which are larger than the specified measurement uncertainty of the detector².

This razor blade measurement was repeated for several positions within a range of 10 mm along the optical axis to record the axial dependence of the beam waist. The results of the measurements are given in Table 4.1. The measurements show a linear increase of the beam waist as a function of the distance from the fibre as expected for a Gaussian beam outside the Rayleigh range.

Table 4.1.: Results from the input beam measurement

rel. distance (mm)	Gaussian waist (μm)
0	60(1)
0.1	71(7)
0.3	85(3)
0.5	104(3)
1.0	147(3)
5.0	485(15)
10.0	902(31)

A fit of Eq. 2.44 to the data presented in this table gives a minimum beam waist of $w_0 = 2.72(2) \mu\text{m}$. Since all measurements were performed outside the Rayleigh range the minimum waist can also be determined from the divergence angle given in Eq. 2.46. Using the minimum and the maximum value from Table 4.1 yields

$$\Theta \approx \frac{902(31)\mu\text{m} - 60(1)\mu\text{m}}{10\text{mm}} = 4.82(18)^\circ. \quad (4.2)$$

²Thorlabs S120C detector with $\pm 3\%$ uncertainty

For the output beam one can assume a Gaussian with $M^2 = 1$ since it emerges from a PM fibre which only guides the lowest Gaussian mode. Here, M^2 is defined according to Eq. 2.50. From Eq. 2.46 follows, that $w_0 = 2.76(10) \mu\text{m}$ which agrees with the value obtained from the fit. The obtained beam waist at the output of the fibre can be used in the simulation in ZEMAX OpticStudio. Detailed information about setting up a simulation with this parameter in OpticStudio is given in Appendix A.

4.2. Simulating the lens array

The beams launched by the fibre array need to be collimated, such that they fit into the hexagonal shape introduced by the single mirrors of the MMA. This collimation is done by a lens array placed in front of the fibre array. The pitch (lens to lens distance) of the lens array has to be matched to the dimensions of the fibre array, to ensure that every beam impinges onto the optical axis of a lens in the array, which are also called lenslets. This minimises optical aberrations and ensures that the beams are not deflected by the lenslets. Further, the aperture of the lenslets should be as large as possible, such that the beam diameter is smaller than the lens diameter, preventing loss of light intensity. The propagation through a commercially available lens array³ and other, unavailable lens arrays with approximately twice as large apertures was simulated in the setup shown in Figure 4.2 to investigate their performance.

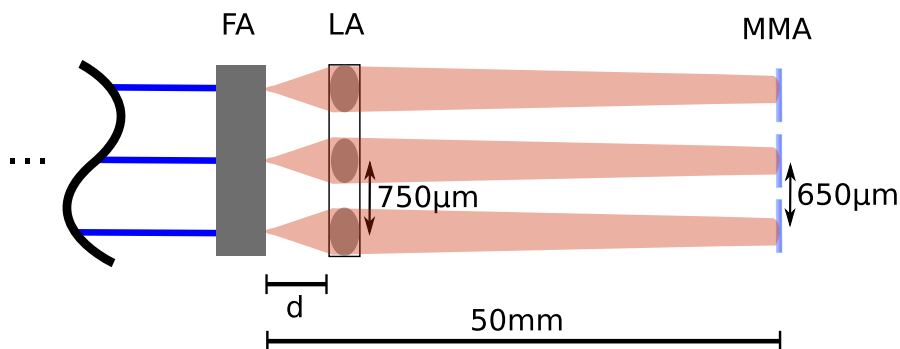


Figure 4.2.: Setup for all investigated lens arrays. The lens array is placed at a distance d away from the input beam such that the beam waist is minimised at the MMA, which is placed 50 mm away from the input beam. As mentioned in Ch. 3.4, the only available fibre array when we implemented the setup into the experiment was mismatched to the MMA. Due to this (s. Fig. 3.13 and 3.9), only the beam originating from the central fibre is focused onto the centre of a mirror; the other beams will impinge onto the mirrors off-centred. This is why the constraints on the beam size are even stricter with the mismatched fibre array, as one beam should only hit a single mirror.

³SUSS MicroOptics 18-00039 with pitch $250 \mu\text{m}$ and ROC $535 \mu\text{m}$.

4. Optical design and tests

In the simulation, the lenslets were placed at a distance d in front of the input beams, such that the beam sizes were minimised 50 mm behind the input, where the MMA resides. The M^2 , defined in Eq. 2.50, and relative power of the beams behind the MMA for the commercially available lens array were obtained from the simulation and are plotted as the leftmost values in the plots in Figure 4.3.

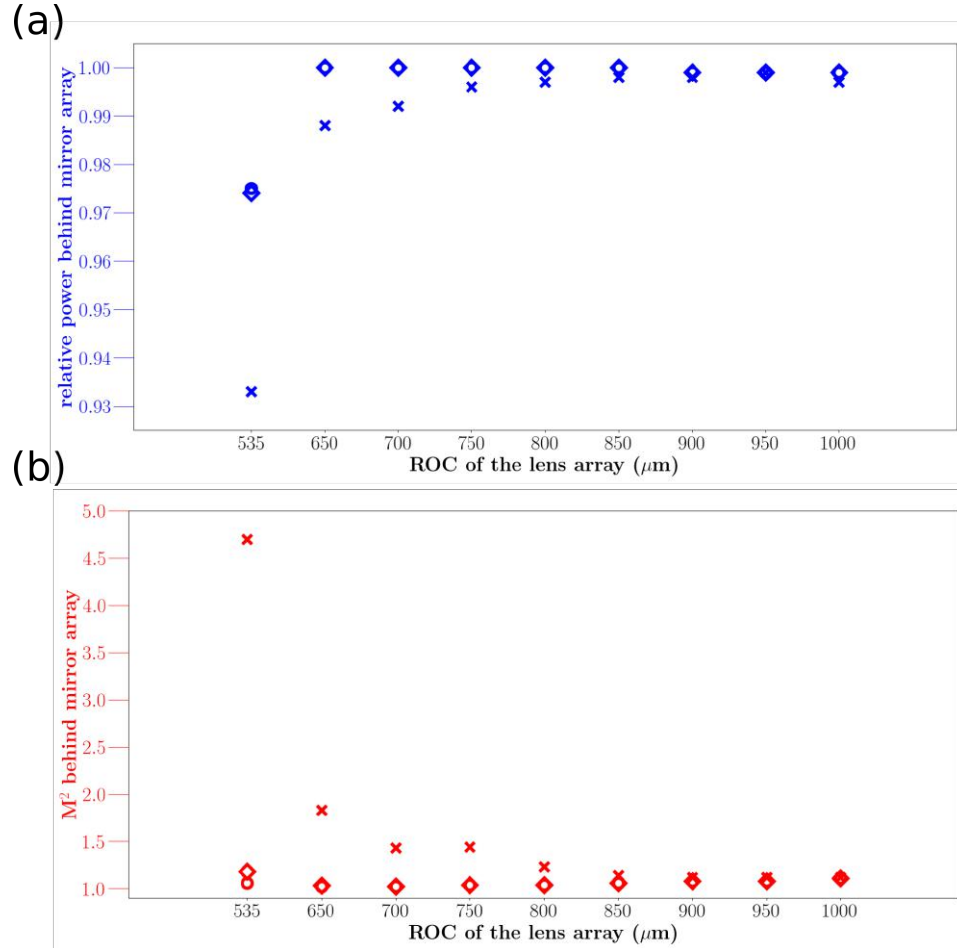


Figure 4.3.: (a) Plot of the relative power behind the MMA for the central beam (circles), the beam that is 750 μm displaced (squares) and the beam that is 1.5 mm displaced from the optical axis (crosses) for the commercially available lens array and for the lens arrays implemented on a fused silica substrate with the LightForge technique⁴, which are described further down. (b) Plot of the M^2 value behind the MMA for the same beams as in (a). The corresponding apertures of the lenslets are given in Table 4.3.

The commercially available lens array has been tested in the laboratory beforehand, where it failed to produce collimated beams. This is due to the small lens diameters of 250 μm , which

⁴See footnote 6.

stem from the lenslet pitch being only $250\ \mu\text{m}$. Typically, commercially available lens arrays have even smaller pitches that do not fit the pitch of the fibre array. Additionally, the lens arrays with smaller pitches have smaller apertures. As can be seen from Figure 4.3, the commercially available array with $535\ \mu\text{m}$ ROC shows degraded relative power and high M^2 values for the central beam as well as for the neighbouring displaced beams. Due to this result we considered to buy a custom made lens array with larger apertures.

We are aware of two companies which offer to fabricate custom made lens arrays. One of them is FEMTOPrint, which uses a femtosecond laser to imprint arbitrary 3D structures into glass substrates⁵. The other company is PowerPhotonic, which uses a laser micro-machining technique called LightForge to print structures onto a fused silica substrate⁶. The properties of the manufacturing procedures of those two companies are summarised in Table 4.2.

Table 4.2.: Comparison of lens array properties from PowerPhotonic and FEMTOPrint

Property	PowerPhotonic	FEMTOPrint
material	fused silica	fused silica
resolution	not specified	up to 600 nm
maximum surface slope	8° / up to $15\text{--}20^\circ$	not specified
maximum surface depth	$50\ \mu\text{m}$	not specified
size	$15\ \text{mm} \times 15\ \text{mm}$, 1 mm thick	up to $76\ \text{mm} \times 26\ \text{mm}$, 10 mm thick

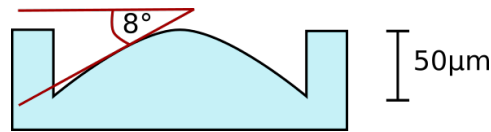


Figure 4.4.: Typical lenslet obtained from the fabrication processes mentioned in this chapter. Surface depth and surface slope are indicated and the maximum achievable values with the LightForge technique [59] are given.

We decided to use the array from PowerPhotonic, because of their more accurate specifications of the maximum achievable surface properties. They specify the maximum achievable surface depth to be $50\ \mu\text{m}$ and a maximum assured surface slope of 8° ; these properties are illustrated in Fig. 4.4. FEMTOPrint on the other hand specifies their resolution to be 600 nm, but does not give a constraint on the maximum achievable surface slope. Further, PowerPhotonic offers the possibility to print several arrays on a single substrate for the same price.

The same simulation as employed for the commercially available lens array has been performed for lenslets with bigger lens apertures with ROC constrained by the specifications of the LightForge procedure. Due to manufacturing constraints, larger apertures correspond to larger ROC, which is why the other lens arrays have larger ROC than the commercially available array. The

⁵More information about the fabrication process can be found here: <https://www.femtoprint.ch/>

⁶More information about the fabrication process can be found here: <http://www.powerphotonic.com/rapid-prototyping>

4. Optical design and tests

results of those simulations are plotted in Figure 4.3 and the corresponding lenslet apertures are summarised in Table 4.3.

Table 4.3.: Apertures of the lenslets in the lens arrays bought from PowerPhotonic

Number	ROC (μm)	lenslet aperture (μm)
1	650	500
2	700	520
3	750	540
4	850	572
5	800	556
6	900	590
7	1000	618
8	950	610

For this simulation, lenslets with ROC of 850 μm show the best combination of transmitted power and M^2 values of the beams behind the MMA. Actually, lenslets with 950 μm ROC show better results in a refined setup, where the beam radius is not minimised at the MMA, but behind it. The combination of transmitted power and M^2 values is better in this case, since the lenslet is placed closer to the fibre which results in reduced intensity loss at the lenslet itself. Due to this reason, the 950 μm lens array is used in the following simulations and in the experiment.

The substrate from PowerPhotonic is depicted in Figure 4.5, where the arrays used for further simulations are circled in blue, those are the ones with ROC of 950 μm .

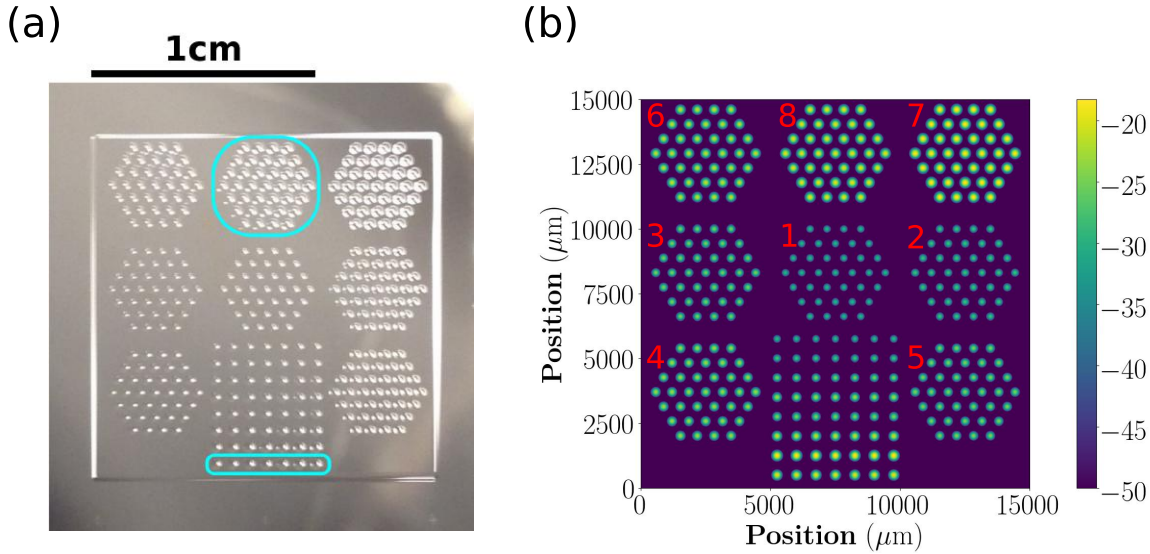


Figure 4.5.: (a) Photo of the manufactured LightForge part with the arrays used for further simulations and experiments circled in blue. (b) Surface depth of the lenses in the array indicated in false colour; the values on the colorbar are given in μm . The ROC and lenslet apertures of each array are given in Table 4.3, where the numbering in the table corresponds to the numbers given in (b).

As can be seen in this figure, several arrays have been integrated onto a single substrate. Some of them have a honeycomb shape, that is matched to the geometry of the MMA. Those arrays are suitable for a future 2D addressing scheme as described in Chapter 6.

4.3. Optical setup to address small strings of ions

In the course of this thesis, several optical setups have been tested. Since the ions are only a few wavelengths apart from each other and each of them needs to be in the focus of the corresponding laser beam to obtain maximum atom-light coupling, the beams' waists and angles need to be controlled. This is done with a lens system between MMA and the ions. With the customised lens array discussed in the previous section several setups for the free space optics between MMA and objective shown in Fig. 3.12 were simulated. The most straightforward implementation would be to put no optical elements between the MMA and the objective and move the mirrors of the MMA such that all beams impinge close to the centre of the objective as shown in the upper part of Figure 4.6. Clearly, not all beams can impinge exactly onto the centre of the objective, since their foci would be equidistant and thus not be matched to the ion positions. Nevertheless, this configuration would minimise the optical aberrations introduced by the objective. To realise it, the distance between MMA and objective would have to be 11 m to get from an initial beam separation of $650\ \mu\text{m}$ down to a beam separation of $4\ \mu\text{m}$ in the focal plane of the objective, which has a focal length of approximately

4. Optical design and tests

70 mm. The divergence of the Gaussian beam would lead to a loss of optical power at the objectives' aperture due to the long distance to the objective. Additionally, the long propagation path is demanding for the stability of the experimental setup. Another possible setup is to use a telescope consisting of two lenses to expand the beam onto the objective. Such a configuration is also used in the current addressing setup with a telescope having a magnification of eight. In contrast to the old addressing scheme, the new scheme involves beams that impinge onto the telescope hundreds of μm displaced from the optical axis. This deviation from the optical axis will be amplified by the telescope's magnification leading to excursions of 5.2 mm for the beams next to the central beam and 10.4 mm for the beams next but one to the central beam for the telescope that is currently used in the experiment. This telescope has a magnification of eight and consists of two lenses with $f_1=25\text{ mm}$ and $f_2=200\text{ mm}$; the distance between the two lenses is 130 mm. The large gap to the optical axis leads to optical aberrations and clipping of the beams at the aperture of the lenses.

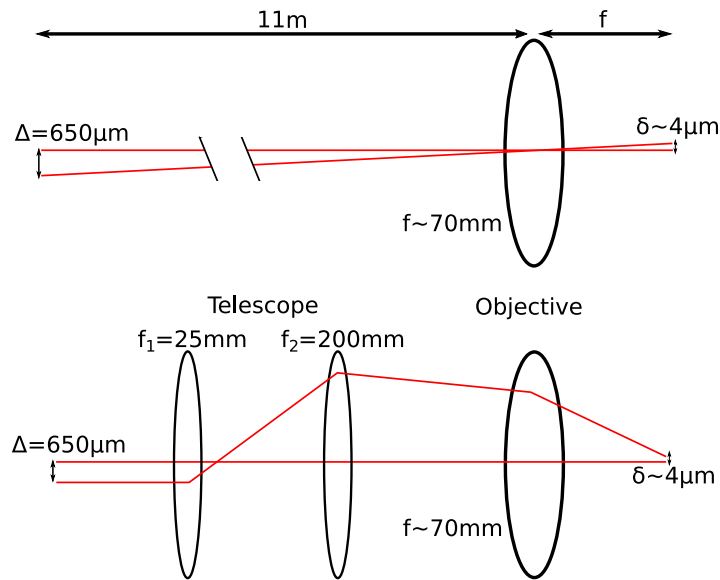


Figure 4.6.: Sketch of two simple optical setups for the system of lenses between the MMA and the objective used to expand the beams onto the objective. The setup without lenses shown above would need a propagation distance of 11 m to get down to beam separations of $4\ \mu\text{m}$ in the focal plane of the objective. A setup with a telescope leads to excursions of beams impinging onto it away from the optical axis.

Due to these complications, ZEMAX OpticStudio was used to simulate configurations with different layouts. For finding the best trade-off between intensity loss due to the lenses' apertures and beam size at the position of the ions, ZEMAX was used to optimise over several thousands of configurations consisting of commercially available stock lenses that do not form a telescope, i.e. configurations with either more or less than two lenses that do not necessarily transform a collimated beam into another collimated beam.

4.3.1. Simulation of the setup

The simulated setups were optimised for several parameters: maximum power transmission, the beam quality M^2 , the beam waist in the focal plane of the objective, and the distance between the beams in this plane. The constraint on maximum power transmission is introduced to prevent the simulations from wandering off into configurations where no power is transmitted to the ions. Further, the separation of the single beams in the focal plane of the objective should match the separation of the single ions in the ion crystal, such that each beam can be used to address a single ion. Finally, the beam waist should be smaller than the inter-ion separation, such that the effect of a laser beam addressing one ion is small on the neighbouring ions. This influence on the neighbouring ions is called crosstalk and will be measured in the experiment in Chapter 5.4. Crosstalk is defined as [60]

$$\epsilon = \frac{\Omega_{\text{unaddr.}}}{\Omega_{\text{addr.}}} , \quad (4.3)$$

that is the ratio of the Rabi frequency of the unaddressed ion $\Omega_{\text{unaddr.}}$ to the Rabi frequency of the addressed ion $\Omega_{\text{addr.}}$. According to Eq. 2.13 the Rabi frequency is proportional to the electric field of the laser beam. Thus, crosstalk corresponds to the relative electric field on a neighbouring ion when addressing one ion.

For matching the beam separation in the focal plane with the inter ion separation in the ion string a high magnification is needed, since an initial separation of $650 \mu\text{m}$ needs to be brought down to $4 \mu\text{m}$. This amounts to a magnification of ~ 160 , which many of the simulated setups couldn't obtain. Often, the beams cannot be moved onto the positions of the ions in the ion crystal without losing a large amount of their optical power at the aperture of the objective because of their large initial separation. This problem arises due to the objective's small NA of only ~ 0.29 . Due to the small NA, the off-axis beams from the fibre array will clip at the aperture of the objective, if they are not steered onto its centre. Additionally, tilting the mirrors of the MMA will decrease the power going through the objective already for small angles, which leads to the problem that the beam behind the objective cannot be steered efficiently with the MMA.

The setup that could steer the beams onto the ions' positions and offers the best trade-off between power loss and beam size in the focal plane is presented here. This configuration is able to address four ions at a trap frequency of $\sim 1 \text{ MHz}$ with a customised fibre array matching the dimensions of the MMA (s. Appendix B) and the corresponding lens array on the LightForge substrate with $650 \mu\text{m}$ pitch between the lenses and a ROC of $950 \mu\text{m}$. This setup is sketched in Figure 4.7.

4. Optical design and tests

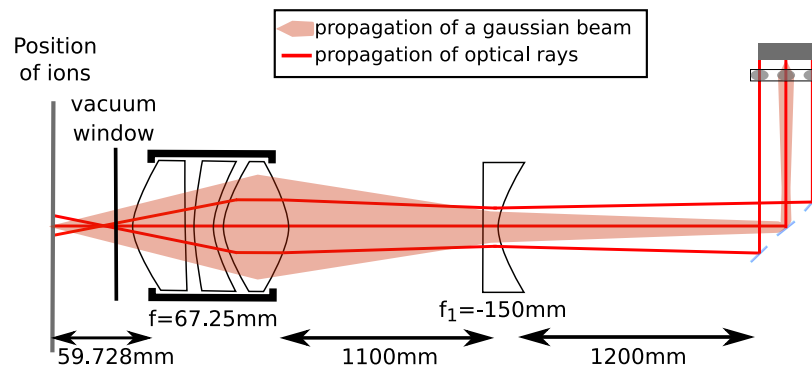


Figure 4.7.: Schematic illustration of the free space optics. Here, the system of lenses is given by a single concave lens with focal length $f_1 = -150$ mm.

The simulation of this setup predicts waists of $\sim 1.7 \mu\text{m}$ for all four beams with beam separations of $\sim 4.1 \mu\text{m}$ between the two beams in the middle and $\sim 4.4 \mu\text{m}$ from the two central beams to the outer two beams. Thus, the beam separations in this configuration are suitable to address all ions in a four ion crystal at ~ 1 MHz. Crosstalks between the beams and neighbouring ions have been calculated from the simulated intensity distributions using Eq. 2.13 and 4.3. The crosstalk between the two central beams is $\sim 14\%$ and below 10% between the central and the outer beams. Further, the power loss at the objective's aperture is smaller than 10% for each beam. The expected intensity distribution resulting from the four beams in the centre of the fibre array is shown in Figure 4.8 a.

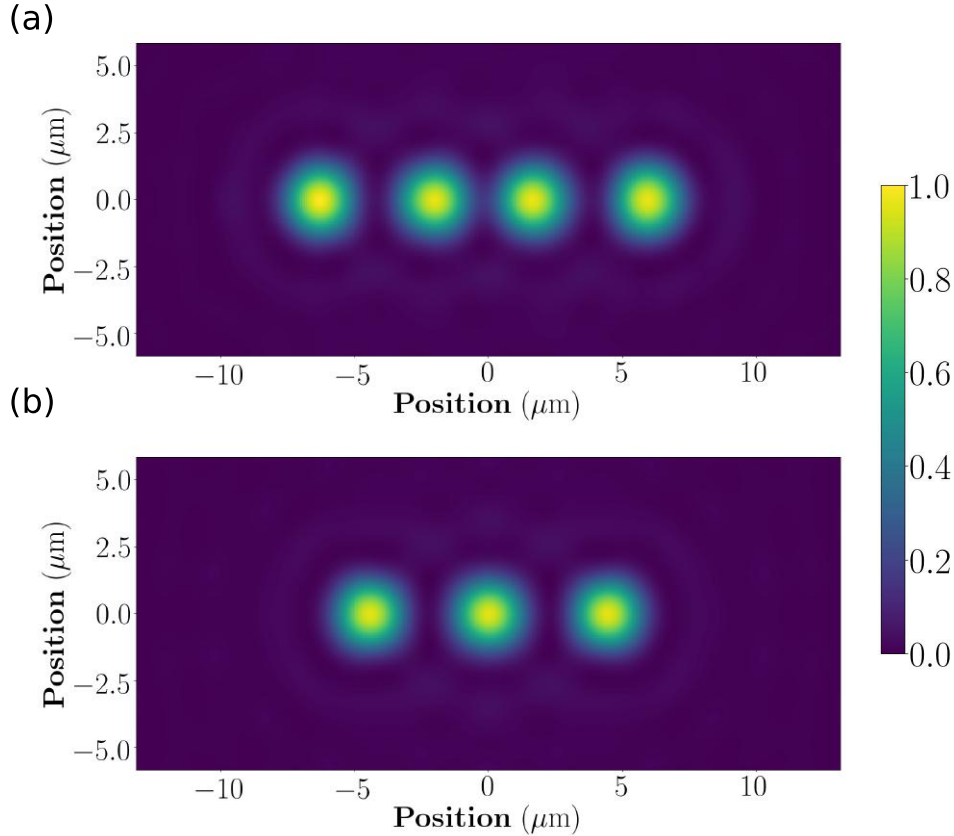


Figure 4.8.: (a) Simulated positions of four beams in the plane of the ions with the customised fibre array described in Appendix B. (b) Simulated positions of three beams with the commercially available fibre array introduced in Ch. 3.4. The colorbar indicates the normalised irradiance for both plots.

In the experiments performed during the work of this thesis the customised fibre array was not yet available. Thus, setups with the commercially available fibre array discussed in Section 3.4 together with the one dimensional array with pitch $750\ \mu\text{m}$ and ROC of $950\ \mu\text{m}$ on the LightForge substrate have also been investigated. Simulations with the same free space optics as in the setup discussed above show addressability of three ions at a trap frequency of $1\ \text{MHz}$. The simulation predicts beam waists of $w_0 = 1.7\ \mu\text{m}$ for each of the three addressing beams with inter-ion separations of $d = 4.4\ \mu\text{m}$ between each of them. Figure 4.8 b shows the profile in the plane of the ions obtained from the simulation. Further, the simulation shows a crosstalk of 6% from the central beam to the outer two ions and a crosstalk of 9% from the outer two beams to the central ion. Again, the power loss at the objectives' aperture is smaller than 10% for each of the beams.

The simulation with the commercially available fibre array predicts addressability of only three instead of four ions because of the larger separation between the fibre outputs of $750\ \mu\text{m}$ compared to the $650\ \mu\text{m}$ with the customised fibre array.

4.3.2. Experimental test setup

The simulated setup with the commercially available fibre array discussed in the previous section was implemented in the laboratory in a test setup on an optical table. To facilitate the transfer of this setup to the experiment table, the fibre array, lens array and MMA are mounted onto a breadboard. Thus, the arrays can be pre-aligned to each other in the test setup before being placed into the main experiment. Further, the lens array is mounted on an X,Y,Z-translation stage⁷ with piezo controlled actuators which provide a stepsize of 20 nm. This translation stage together with a tip-and-tilt stage, on which the fibre array is mounted, are used to adjust the relative position between fibre array and lens array, such that each beam impinges onto the optical axis of its corresponding lenslet and all beams are collimated. Collimation of the outgoing beams is ensured by minimising the beam waist at a distance of ~50 cm behind the fibre array. The MMA is placed ~5 cm behind the lens array facing it with a slight tilt around the horizontal axis. Due to this tilt, the beam is reflected such that it propagates back above the other two arrays. This small angle is chosen to maximise the surface of the single mirrors as seen from the laser beam. The setup of the three arrays on the breadboard is depicted in Figure 4.9.

⁷Newport 9067-XYZ-PPP-M

4.3. Optical setup to address small strings of ions

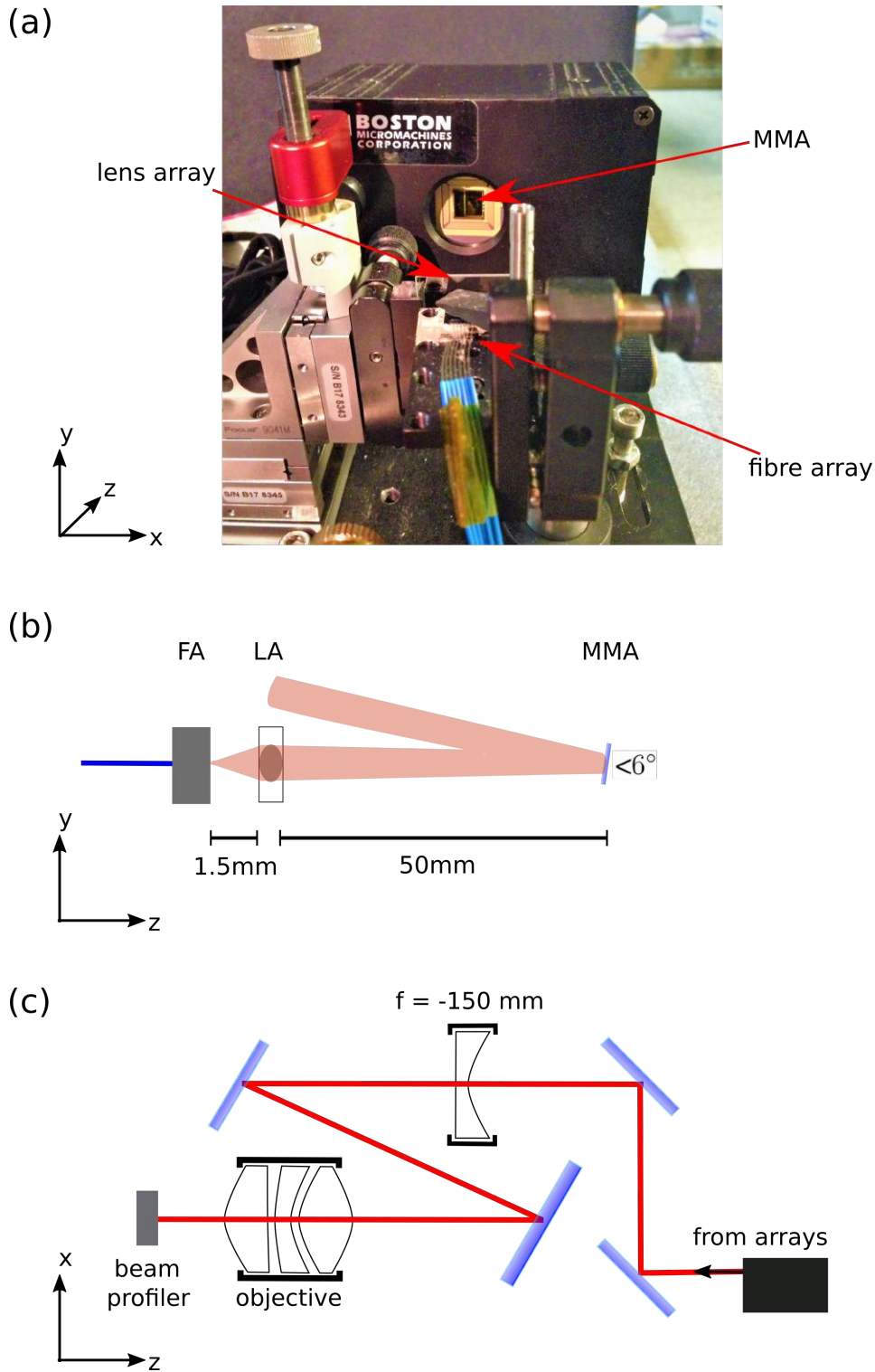


Figure 4.9.: (a) Breadboard with the fibre array (FA), lens array (LA) and the MMA. The LA is mounted on a translation stage with 20 nm stepsize. The MMA is tilted such that the beams originating from the fibre array can pass over the lens array and fibre array. (b) Schematic illustration of the light propagating through the arrays. The deflection angle of the MMA is smaller than 6° . (c) Scheme of the experimental test setup. A beam profiler is placed behind the objective to record the intensity distribution in the focal plane.

4. Optical design and tests

Behind the MMA, the beam is deflected via two two-inch mirrors onto the two-inch $f = -150$ mm lens and then onto the objective via two more mirrors, as is shown in Fig. 4.9 c. The last mirror before the objective is a three-inch mirror, as opposed to the other two-inch optics in the setup, such that no power is clipped due to its aperture. The objective used in the test setup is identical to the one used in the experiment. It is mounted onto an X,Y,Z-translation stage. This stage and the mount of the three-inch mirror are used to minimise the aberrations of the laser spot on a beam profiler placed in the focal point of the objective.

The 729 nm laser has been inserted into the central fibre and the two neighbouring fibres and the image on the CCD camera in the focal plane of the objective has been recorded for all three fibres. The three beam profiles are shown in Figure 4.10.

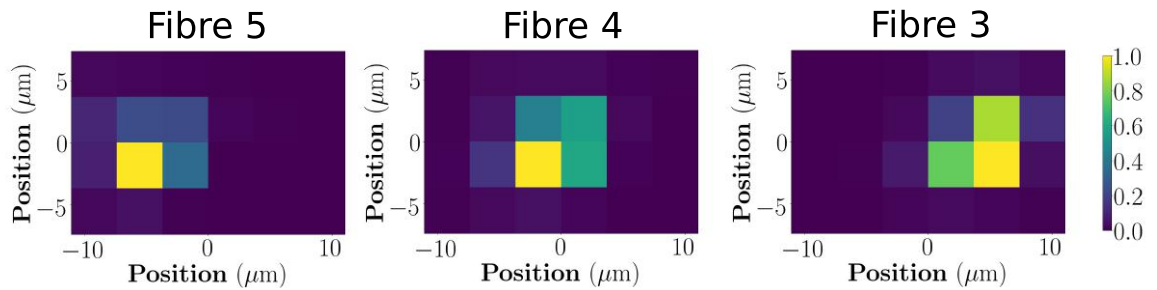


Figure 4.10.: The plot in the middle shows the beam profile of the beam coming from the central fibre, while the other two plots show the two profiles of the two neighbouring beams in the focal plane of the objective. The colorbar on the right hand side gives the normalised intensity for all three plots. These measurements are used to extract the relative beam positions for comparison with the simulation.

Fitting 2D Gaussian functions to the three profiles reveals a separation of $d = 4.5(1)$ μm between them. Thus, the distance between the beams in the focal plane matches the distance that the simulation predicted. Furthermore, the measurement reveals that the beam waists are smaller than 5 μm . The exact waist cannot be determined because of the limited resolution of the CCD camera of $3.69 \mu\text{m} \times 3.69 \mu\text{m}$, but can be measured by assembling the setup into the experiment, which is described in Chapter 5. A comparison of the simulated intensity distribution, as discussed in Sec. 4.3.1, and the measured intensity distributions is shown in Figure 4.11. The relative positions of the measured laser beams shown in Fig. 4.11 b correspond to the positions of the simulated beams in Fig. 4.8 b.

4.3. Optical setup to address small strings of ions

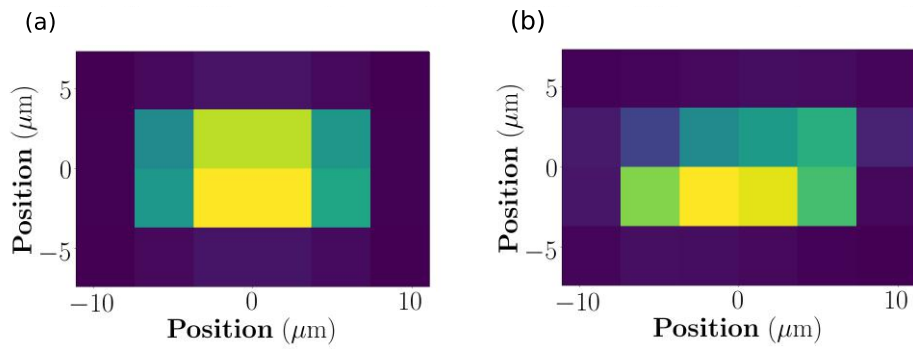


Figure 4.11.: (a) The same simulation result as already given in Fig. 4.8 b. Here, the intensity is binned into pixels with a size of $3.69 \mu\text{m} \times 3.69 \mu\text{m}$ for comparison with the measured data. (b) Sum of the three pictures shown in Fig.4.8 b 4.10. The pictures were taken with a CCD camera placed behind the objective in the test setup.

5. Characterisation of the addressing beams

In this chapter, measurements performed at the ion quantum computer with the simulated setup presented in the previous chapter are presented. In Section 5.1 the process of installing the new optical setup on the experiment table is described. To extract ion positions from the EMCCD images, the imaging has to be characterised and calibrated, which is described in Section 5.2. Measurements of the spot sizes and crosstalk between the three addressing beams in a three-ion crystal are presented in the last two sections of this chapter.

5.1. Testing the addressing setup

In order to measure the beam properties at the ions' positions, the optical setup has to be integrated into the existing experimental setup. Therefore, the setup for addressing up to three ions, which was presented in Section 4.3, is implemented into the experiment. For this, the breadboard with the three arrays is moved onto the experiment table. The fibre AOM used in the current addressing setup is inserted into one of the fibres of the fibre array. A periscope composed of two mirrors is used to deflect the beam to another breadboard above the optical table, which is at the level of the ion trap. Here, the beam passes through the -150 mm lens, before it hits the dichroic mirror, which sends the beam through the objective onto the ions in the trap. A sketch of the setup in the experiment is given in Figure 5.1.

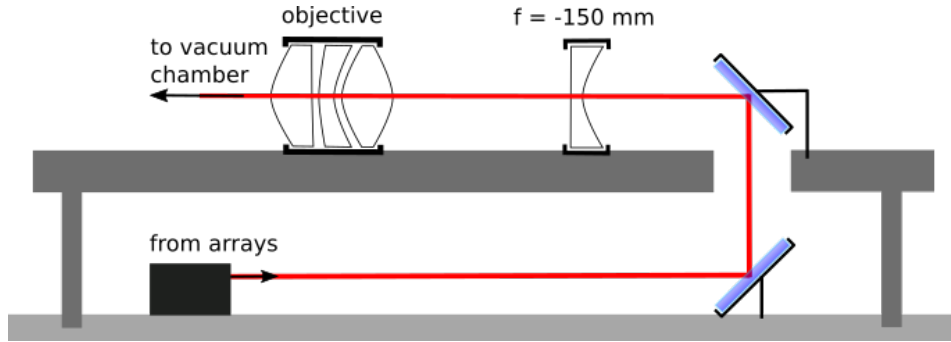


Figure 5.1.: Sketch of the setup on the optical table. The breadboard with the arrays is mounted on the lower level. A periscope deflects the beam onto the upper level, where the beam impinges onto the -150 mm lens before it goes onto the objective in front of the vacuum chamber.

With the new addressing setup, the focus of the addressing beams is shifted along the optical axis compared to the focus position with the old addressing setup. Therefore, the objective has to be moved by ~ 510 μm along the optical axis to ensure the light being focused to the position of the ions. Since the objective is also used for fluorescence detection on the EMCCD camera, as can be seen in Fig. 3.7, the rest of the imaging path has to be changed as well, such that the fluorescence light is focussed onto the EMCCD. The shift in the objective's position leads to the fluorescence light being focused more than 50 cm behind the EMCCD camera. This change in focal length is compensated by putting a -100 mm lens into the imaging path between dichroic mirror and EMCCD. That way, the image of the ions is refocused onto the EMCCD without disturbing the addressing beam.

For adjusting the setup, such that the beams impinge onto the ions in the trap, the -150 mm lens is mounted onto an X,Y,Z-translation stage with 10 μm stepsize. This stage, in addition to the tilt of the last mirror before the dichroic mirror, is used to adjust the beam from the central fibre onto the position of a single ion in the trap. The beam position is optimised onto the position of the ion by applying continuous 729 nm light to it and detecting the frequency of quantum jumps the ion is undergoing. This configuration is used to optimise the alignment up to the point where the PMT detection count rate drops to 50 % of its value for the ion being in the ground state. This count rate indicates that the qubit transition is saturating. As soon as this point is reached, the 854 nm laser is switched to pump the ion back into the ground state, which results in a higher detection count rate. Additionally, the 854 nm laser increases the sensitivity of the laser-ion alignment to the count rate. This rate can be decreased subsequently, improving the alignment of the laser beam with the ion.

5.2. Imaging calibration

Due to the necessary changes to the imaging path, the magnification has to be recalibrated. This recalibration is needed to be able to determine the ions' positions from EMCCD images,

5. Characterisation of the addressing beams

which is crucial for the measurements described further on in this chapter.

For this purpose, three ions are loaded into the trap and imaged onto the EMCCD camera. The endcap voltages are set to 800 V each, which according to previous measurements corresponds to a trap frequency of 1075 kHz. The distance between the outer two ions in a three ion crystal imaged onto the EMCCD camera can be calculated with Eq. 2.8. Here, one has to take into account the angle of 22.5° between the ion crystal axis and the EMCCD plane resulting in a distance

$$\Delta = 2.1544 \cdot \sqrt[3]{\frac{e^2}{4\pi\epsilon_0 M \omega_{tr}^2}} \cdot \cos(22.5^\circ) = 8.377 \mu m \quad (5.1)$$

with the electron charge e , the ion's mass $M = 39.96u$ for $^{40}\text{Ca}^+$ [61] with u being the atomic mass unit and the axial trap frequency ω_{tr} . The distance in pixel on the EMCCD camera between those two ions is determined via two 2D Gaussian fits to the ions on an EMCCD image to extract their positions. Here, A is the amplitude of the Gaussian, A_0 is an offset and x_0/y_0 and σ_x/σ_y are the positions and widths of the spot in x and y direction respectively. Figure 5.2 shows an image of the three ion crystal with the distance of $\Delta = 40.5(1)$ px between the outer ions.

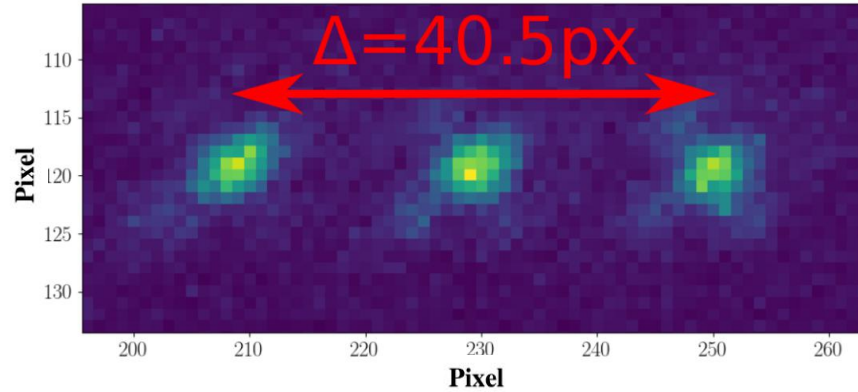


Figure 5.2.: Measurement of the distance between the outer two ions in a three ion crystal for an endcap voltage of $U_0 = 800$ V. The distance between the ions is determined from 2D Gaussian fits, which give a separation of $\Delta = 40.5(1)$ px.

It follows, that each pixel on the camera corresponds to

$$1px \hat{=} 0.2068(5)\mu m, \quad (5.2)$$

which corresponds to a magnification of ~ 77.3 for the EMCCD pixelsize of $16 \mu m$.

For the beam-width measurement, the position of the ion needs to be shifted along the ion crystal axis for determining the Rabi frequency at several positions along the radial profile of the beam. This is done by putting an offset voltage onto one of the two endcaps. This has

been calibrated using a single ion in the trap and taking a picture on the EMCCD camera for each displacement voltage. The ion position vs. applied offset voltage at an endcap voltage of $U_0 = 800$ V is plotted in Figure 5.3. The ion position is changed linearly with the offset voltage. Thus, a linear fit to the data yields a slope of $1.245(4)$ px/V. The blue data points in the plot are not fitted. They were measured about two hours before the other measurements were taken and indicate drifts in the optical setup. These drifts can also be observed on the EMCCD camera, where the ion drifts in the vertical direction by a few pixel during the course of a few hours. This drift can mainly be attributed to drifts of the objective's translation stage, because the position on the EMCCD is very sensitive to the objective's position.

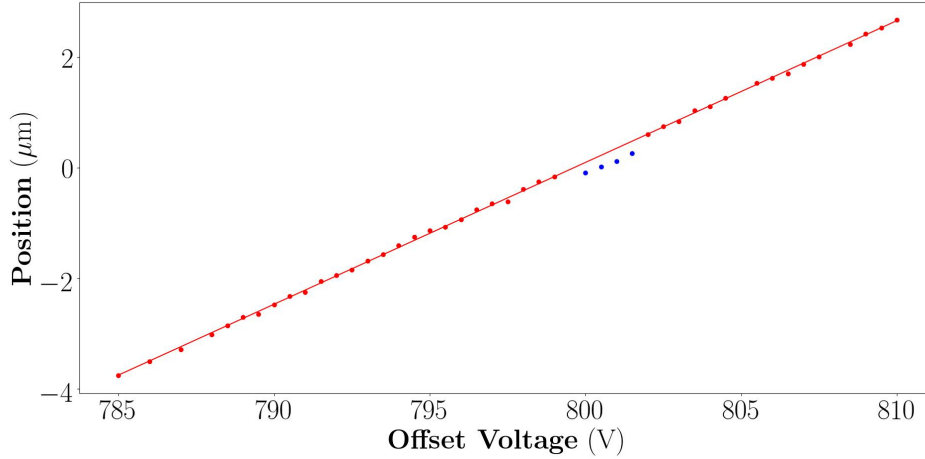


Figure 5.3.: Ion position on the EMCCD camera as a function of the applied offset voltage. The positions were determined by fitting Gaussian functions to the EMCCD images. The fit errors are smaller than the data points. Blue data points are not fitted, they were measured approximately two hours before the other measurements and visualise the drifts present in the setup.

5.3. Beam-width measurement

For measuring the waist of the central addressing beam, a single ion is loaded into the trap and its Rabi oscillations in the vicinity of the addressing beam are recorded with the M-ActION control unit, which is described in [49].

An experimental sequence consists of Doppler cooling the ion for 5 ms with the 397 nm laser and the 866 nm laser. After that, ground state pumping is performed for 2 ms with 729 nm light on the $m_J = +1/2$ to $m_J = -1/2$ transition. Additionally, the lasers at 854 nm and 866 nm are switched on. After this, the atom should be prepared in the state $|S\rangle$ and can be addressed with the 729 nm laser on the qubit transition for a specified duration and power. Following the atom-light interaction on the qubit transition, the ion is illuminated with 397 nm light for 1 ms for fluorescence detection. After detection, the 854 nm laser together with the 866 nm laser are applied for 0.2 ms to reset the ion from the $|D\rangle$ state to the $|S\rangle$ state. This procedure is repeated

5. Characterisation of the addressing beams

100 times per measurement point to gather statistics. A plot of the excitation of the $^{40}\text{Ca}^+$ ion against the duration of the applied 729 nm laser pulse is shown in Fig. 5.4.

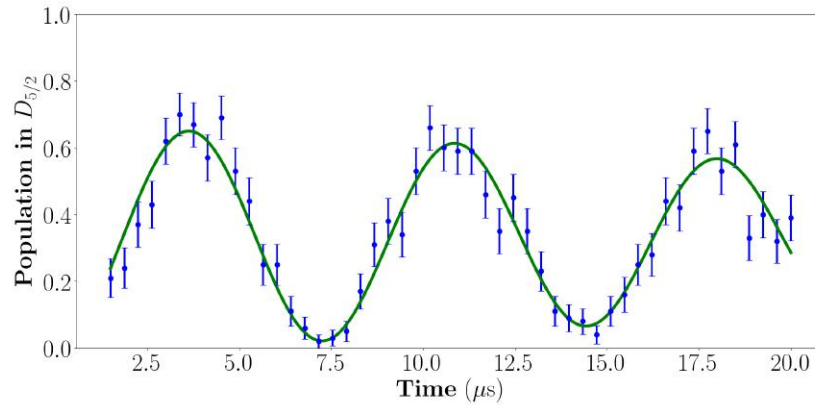


Figure 5.4.: Recorded Rabi oscillations for the laser beam passing through fibre four. The oscillations shown here were recorded with the ion being displaced $0.77 \mu\text{m}$ from the trap centre.

As can be seen in Fig. 5.4, the ion is never completely in the $|D\rangle$ state, which can be attributed to imperfect state preparation. Most likely, the laser for ground state pumping on the $m_J = +1/2$ to $m_J = -1/2$ transition was not set to the right frequency leading to a residual occupation in the $|S, m_J = +1/2\rangle$ -state. This state does not couple to the qubit laser. Thus, the ion will stay in this state and will show up as a qubit in the $|S\rangle$ -state during state detection.

The recorded Rabi oscillations from the interaction of the ion with the 729 nm addressing beam on the qubit transition follow the relation [62]

$$\Omega \propto E_0 \propto \sqrt{I} \quad . \quad (5.3)$$

The beam width is measured by moving an ion along the crystal axis, this is achieved by changing the tip voltage of one of the endcaps using the "iseg" high voltage controller¹. Rabi oscillations are recorded at each position. A scheme of the measurement process is depicted in Figure 5.5.

¹ "iseg" is the name of the company providing these controllers

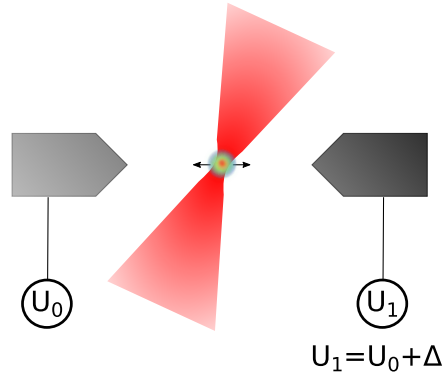


Figure 5.5.: The ion is moved from left to right on the axial trap axis by applying an offset voltage Δ to one of the endcaps using the iseg high voltage controller.

A plot of the squared Rabi oscillations against the position in the trap reveals the intensity profile. This is shown in Figure 5.6.

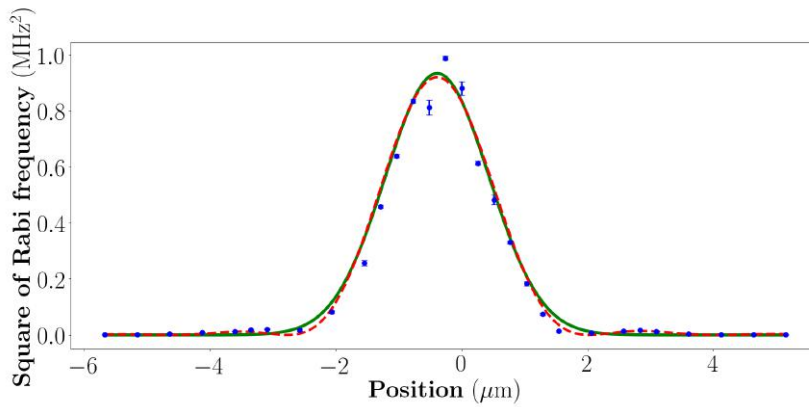


Figure 5.6.: Plot of the squared Rabi oscillations against the axial position of the ion. A fit of the intensity of a Gaussian beam (green solid line) reveals the waist of the beam at the ion position. The two maxima in the wings of the Gaussian profile stem from the finite aperture of the objective and can be modelled by a Bessel function (red dashed line) (s. Ref. [63]).

The intensity profile of a Gaussian beam is given as the square of Eq. 2.42. The resulting function

$$A \cdot e^{-2 \cdot (x-x_0)^2 / w_0^2} \quad (5.4)$$

has been fitted to the data, which gives a waist of $w_0 = 1.52(5) \mu\text{m}$. This waist is smaller than the waist of $\sim 1.7 \mu\text{m}$ expected from the simulation. As can be seen from the plot in Figure 5.6, the profile exhibits non-Gaussian behaviour. This is due to the finite aperture of the objective used to focus the beam onto the ion, which leads to a truncated Gaussian intensity distribution

5. Characterisation of the addressing beams

directly after it. The field of the truncated beam in the focal plane is proportional to the zeroth order Bessel function as has been derived in Ref. [63]. This results in the side maxima present in Figure 5.6.

To conclude this section, it shall be noted that the beam width of the central beam is smaller than the inter-ion separation, which enables single ion addressing.

5.4. Addressing in an ion crystal

In this section, the crosstalk between ions in a three-ion crystal is determined. The measurements shown in the following were performed with the LabView-based program QFP [64]. The experimental sequence is similar to the one used for the measurements in Section 5.3, but with an additional sideband cooling step before the addressed pulse, which was added to be able to observe Rabi oscillations over several oscillation cycles. Before taking the measurements, the optical setup was adjusted such that the central beam coming out of fibre four is aligned with the middle ion. This is done as described in Section 5.1. For addressing the outer two ions, the fibre AOM was inserted into fibre three and five respectively. The MMA was used to tilt these beams to a position where the ratio of excitation on the addressed ion to the excitation of the unaddressed ions was minimised. The excitation probability of the individual ions is measured from the EMCCD signal with the QFP program as described in Ch. 3.2. The results for the central addressing beam and the outer two addressing beams are shown in Figure 5.7. To achieve similar Rabi frequencies, the outer two ions had to be driven with higher laser power than the central ion, indicating that the laser power at their positions was smaller than for the central ion. For the left addressed ion the power was ten times more than for the central ion and for the right addressed ion the power was twenty times more. The smaller power at the outer ions' positions can be explained by loss of laser power at the apertures introduced by the objective and the mirrors in front of the objective on the one hand. On the other hand, the values for the Rabi oscillations on the non-addressed ions shown in Table 5.1 indicate, that the light distribution of the outer two beams is broader than that of the central beam, leading to smaller peak intensities.

The values for the Rabi oscillations and crosstalks between the beams and ions are given in Tables 5.1 and 5.2. The central addressing beam shows an asymmetric crosstalk to the outer two ions and the outer two beams show more crosstalk than the central beam. Interestingly, the crosstalk from the beam coming out of fibre five to the outer ion is larger than the crosstalk to the ion in the centre. This can be explained by the truncation of the Gaussian beam due to the aperture introduced by the objective, which has been discussed in the last section. The intensity of the truncated Gaussian beam in the focal plane is given by the square of the zeroth order Bessel function which exhibits a damped oscillatory behaviour. Thus, the neighbouring ion can be located in a minimum of such a fringe while the next neighbour resides at a maximum.

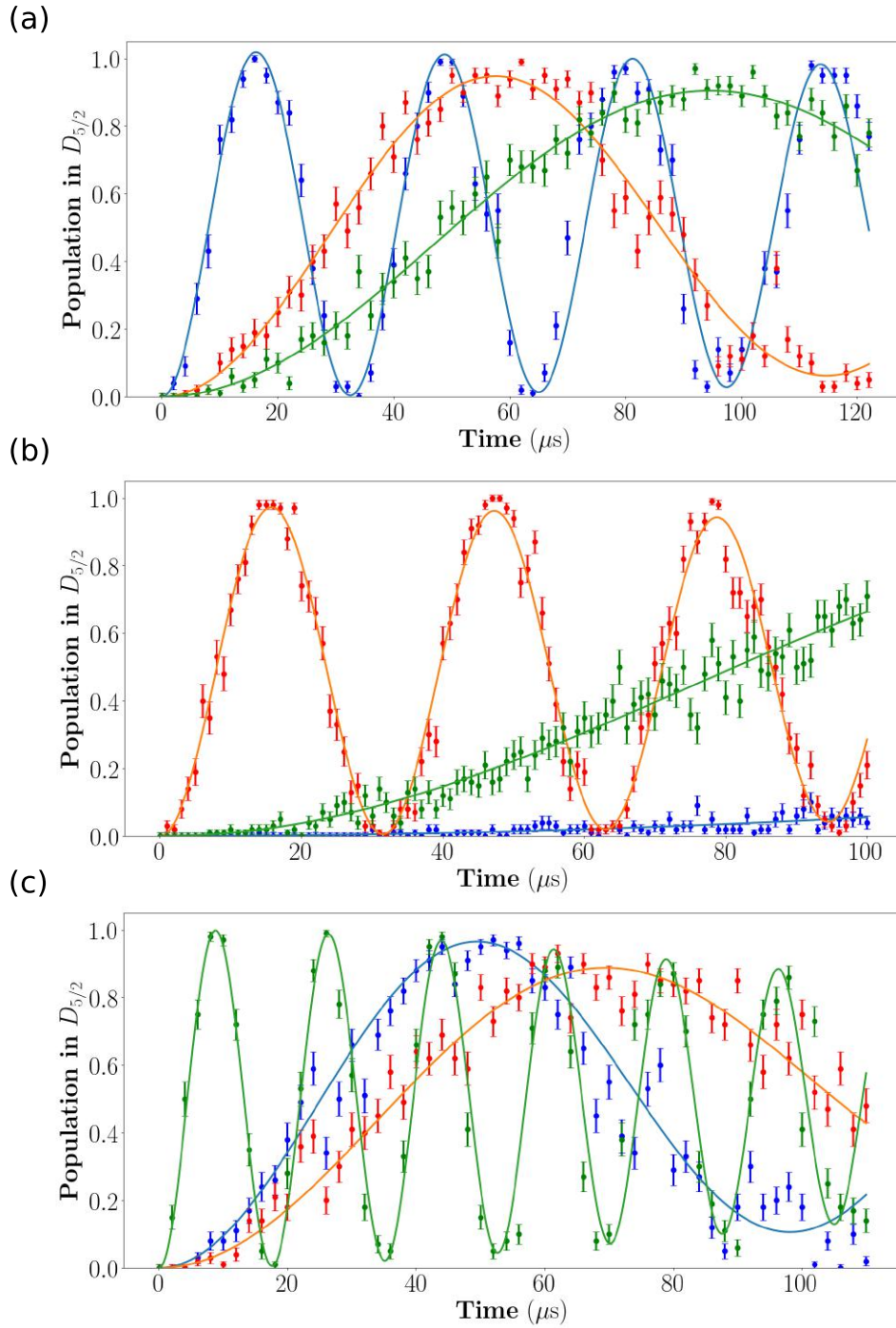


Figure 5.7.: Measurement of Rabi oscillations of three ions while only one of them is addressed. In (a) the left ion (blue) is addressed with fibre three, in (b) the middle ion (red) is addressed with fibre four and in (c) the right ion (green) is addressed with fibre five. The Rabi frequencies obtained from a fit of Eq. 2.19 are summarised in Table 5.1 and the crosstalks between all fibres and ions are given in Table 5.2.

5. Characterisation of the addressing beams

Table 5.1.: Rabi oscillations in a three-ion crystal

on: \ Induced Rabi oscillations from (in kHz):	Fibre 3	Fibre 4	Fibre 5
Ion 1	197(2)	59(1)	37(6)
Ion 2	4(4)	205(1)	24(3)
Ion 3	70(1)	53(1)	366(2)

Table 5.2.: Crosstalk in a three-ion crystal

to: \ Crosstalk from:	Fibre 3	Fibre 4	Fibre 5
Ion 1	-	29.9(6)%	18.8(30)%
Ion 2	4(4)%	-	11.7(15)%
Ion 3	19.1(3)%	14.5(3)%	-

According to the simulation all three beams should have approximately the same beam parameters, which doesn't agree with the measurements. To investigate possible reasons for this discrepancy, the output beams of the three fibres were measured with a beam profiler at a distance of 50 cm behind the MMA. The beam profile obtained from fibre five is shown on the left hand side of Figure 5.8.

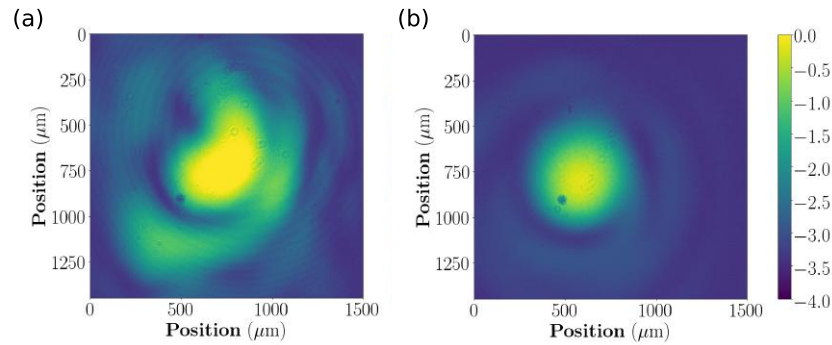


Figure 5.8.: (a) Image of the beam coming out of fibre five at a distance of 50 cm behind the MMA. Distortions are due to misalignments between the fibre array and the lens array. (b) Image of the same beam after correcting the relative position between lens array and fibre array. The intensity data shown in the two pictures was logarithmically scaled to enhance the contrast.

The beam profile deviates from a Gaussian beam, which is due to misalignments between the fibre array and the lens array. Adjusting the relative position of these leads to an improved beam quality, as can be seen on the right hand side of Figure 5.8. The misalignments were most likely introduced into the setup when it was transferred to the experiment table. Another possible reason for the discrepancy observed in the beam parameters could be the fact that

the setup implemented onto the experiment table does not exactly resemble the setup in the simulation in the sense that distances between optical elements do not match up to a couple of centimetres. This might lead to stronger power loss of the outer beams at the objective's aperture when trying to move them onto the position of the ions. The setup is sensitive to such effects as can be seen in Figure 6.1. Further, the trap frequency between experiment and simulation differed by 75 kHz, whereby the ions were $\sim 0.2 \mu\text{m}$ closer to each other in the experiment. Moving the beams onto these positions leads to stronger power loss as well. The mismatch between assumed and actual trap frequency only became apparent when the data was evaluated, but could be matched to the simulated trap frequency for future experiments.

6. Summary and outlook

In the course of this master's thesis a new setup for single ion addressing has been simulated and tested in the experiment. This setup will enable simultaneous and individual addressing of the ions, which leads to a more versatile gate set than the one currently implemented in our experiment. In particular, the new addressing setup will enable us to perform Mølmer-Sørensen-gates on arbitrary subsets of qubits with a set of simultaneously applied laser pulses and speed up quantum computations in this way.

The fibre-based beamsplitters and acousto optical modulators (AOMs) used for multiplexing the laser beam and altering every beam individually have been characterised. It has been shown, that the polarisation extinction ratio (PER) of the AOMs is increased from 27(7) dB to 43(7) dB when using an SM-fibre at the input port. The 3dB-bandwidth of the fibre AOMs has been measured to be larger than 10 MHz, which is sufficient to add the bichromatic fields needed for Mølmer-Sørensen-gates.

The deflection angle of the micro-mirror array (MMA), which is used to move the single beams onto the positions of the ions, has been measured to be 16.5 mrad. It has been shown that the deflection angle changes linearly with the voltage applied to the actuator steering the mirror. A lens array has been designed, which is used to focus the beams onto the MMA. Further, a fibre array matching the dimensions of the MMA was designed.

It has been shown, that the free space optics between the MMA and the objective cannot be implemented as a telescope in the current configuration. Simulations of the free space optics with available stock lenses have resulted in a setup, that can be used to address up to three ions with the fibre array available in the laboratory and up to four ions with the fibre array matching the dimensions of the MMA at a trap frequency of 1 MHz. The simulations showed waists of the addressing beams of $w_0 = 1.7 \mu\text{m}$ and a separation between the beams of $d = 4.4 \mu\text{m}$.

Subsequently, the simulated setup for addressing up to three ions was implemented in a test setup in the laboratory to compare the simulations with the experiment. The results obtained with the test setup showed $d = 4.5(1) \mu\text{m}$ with beam waists smaller than $5 \mu\text{m}$.

Finally, the setup was implemented into the experiment. By performing Rabi oscillations on an ion in the trap, the waist of the central addressing beam was determined to be $w_0 = 1.52(5) \mu\text{m}$. In a three-ion crystal at a trap frequency of 1.075 MHz the cross-talk between the three beams and ions has been measured. The results for this measurement differ from the values obtained in the simulation, which can be attributed to a different trap frequency as compared to the simulation and a misalignment between the lens array and the fibre array.

As of yet, the results of this master's thesis have been summarised. Now, I want to give an outlook on how the tested setup can be improved and what can be achieved with it in the future. A more stable setup can be obtained by mounting the whole free space path on the same level, ideally on the same breadboard. This would circumvent the complications of a periscope.

Nevertheless, the mirrors of the MMA will need to be readjusted from time to time, such that the beams impinge onto the positions of the ions. The mirror tilts of the MMA can be automated with an optimisation algorithm.

A setup for addressing up to four ions can be implemented into the experiment with the customised fibre array; in spite of that, going for large number of ions demands for a high NA objective as will be discussed in the following paragraph.

The biggest problem in the current setup is the fact that the objective has a small NA of ~ 0.29 , meaning that the whole objective has to be illuminated to get to small beam waists in the focal plane. This leads to off-axis beams clipping at the aperture of the objective, as has been stated in Ch. 4.3. Therefore, beams have to impinge close to the centre of the objective to prevent power loss. This however leads to limitations in the tilts that can be introduced with the MMA which in turn limits the position range of the addressing beams in the focal plane of the objective. The conclusion is that a high NA objective could enhance the performance of the addressing setup presented in this thesis.

In fact, we have another experiment in our laboratory, which uses a cryogenic setup with a segmented Paul trap to perform quantum information processing on strings of $^{40}\text{Ca}^+$ and $^{88}\text{Sr}^+$ ions with a high NA objective placed in vacuum close to the trap. The objective¹ with NA ~ 0.8 and a focal length of 9 mm has been installed recently. Detailed information about the experiment can be found in Ref. [65]. Simulations with this objective together with the new fibre array are presented below. The optical setup used for these simulations consists of the arrays placed 690 mm in front of the vacuum chamber's window and the objective residing in vacuum ~ 120 mm away from the vacuum window.

In Figure 6.1 the relative power passing through the objective and the angle of the MMA are plotted against the beam's position in the focal plane of the objective for the central addressing beam with the current objective in the optical setup discussed in Ch. 4.3 and with the new objective in the setup described above.

As can be seen in Figure 6.1, the beam in the setup with the high NA objective can be moved several micrometers in the focal plane without losing more than 1 % of its power, whereas the beam in the current optical setup cannot be steered more than $0.2\ \mu\text{m}$ without losing 2 %–3 % of its power.

¹Edmund Optics 67257 precision asphere

6. Summary and outlook

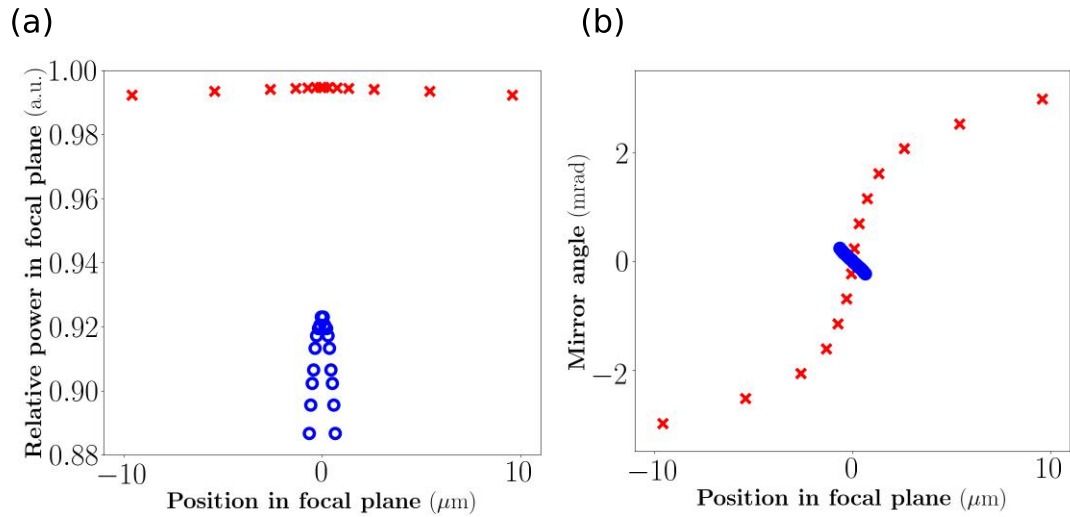


Figure 6.1.: (a) Power of the central beam behind the objective plotted against its position in the focal plane of the objective for the addressing setup presented in this thesis including the new fibre array (blue dots) and for the setup with the high NA objective (red crosses). (b) Plot of the mirror angle of the MMA against the position of the central beam in the focal plane of the objective for the addressing setup presented in this thesis (blue dots) and for the setup with the high NA objective (red crosses).

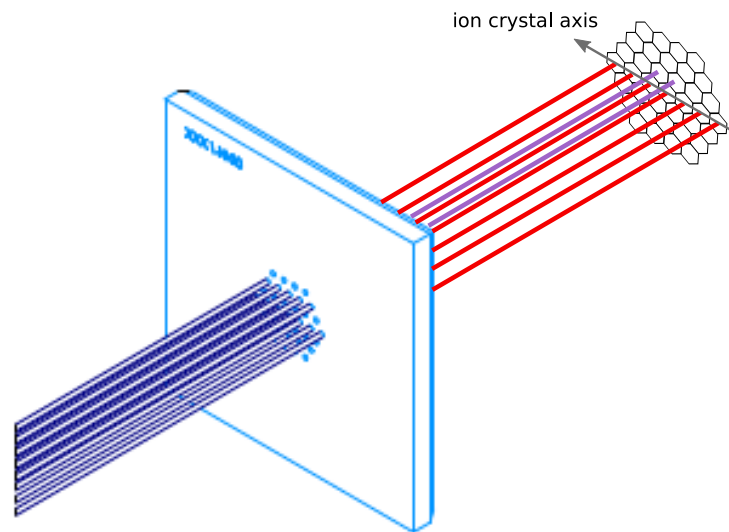


Figure 6.2.: Sketch of the fibre array and mirror array with beams originating from $562.5 \mu\text{m}$ above the ion crystal axis. These beams are steered onto this axis with the mirrors in the MMA. The beams shown here correspond to the nine beams simulated in Fig. 6.3.

This improved steerability could be used to extend the array of laser beams into two dimensions. The mirrors of the MMA are then used to move beams from above and below of the crystal axis onto this axis. A scheme for this two dimensional array of beams employing the customised fibre array described in Appendix B is given in Figure 6.2.

Simulations of the two dimensional array with the free space optical setup described above show that beams originating from the row above and below of the central row can be steered onto the ion crystal axis, which enables one to move 19 beams independently onto the ion axis. A simulation of the light distribution in the focal plane of the objective from seven beams on the crystal axis and two more beams originating from $562.5 \mu\text{m}$ above this axis is shown in Figure 6.3.

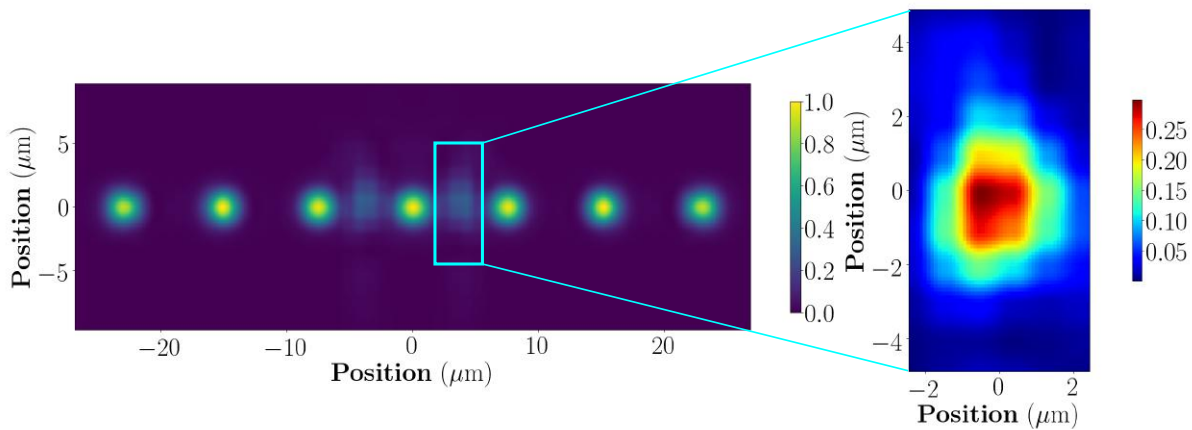


Figure 6.3.: Left: Position of the seven beams on the crystal axis and two off-axis beams steered onto the crystal axis. Right: Intensity profile of one of the two steered beams. It shows deviations from a Gaussian profile, which can solely be attributed to aberrations introduced by the objective. The results shown here are obtained with the optical setup simulated for the cryogenic experiment.

The off-axis beams can be moved onto the crystal axis, while losing only 0.2% of their total power. Nevertheless, they get distorted and show a broader beam profile than the beams originating on the crystal axis. This might be due to the high NA objective not being aberration corrected in contrast to the objective used for the previous simulations.

The objective lens in this setup is illuminated with a Gaussian beam with $1/e^2$ -diameter of $\sim 2.5 \text{ mm}$ leading to a beam waist in the focal plane of $1.8 \mu\text{m}$. This is larger than the beam waist of $1.7 \mu\text{m}$ obtained from the simulations in Ch. 4.3. Still the high NA lens performs better, because the improvement lies in the fact, that 99.5% of the power passes through it and beams can be moved over several micrometers without lowering this fraction, as shown in Figure 6.1. An aberration corrected high NA objective might enable addressing of up to 19 ions individually and simultaneously, if the degraded beam quality observed in the simulations stems only from aberrations introduced by the objective. This is the number of beams that can be moved with the mirrors in the centre row of the MMA and the two rows above and below it, which have been shown to be steerable onto the crystal axis (s. Figure 6.3).

6. *Summary and outlook*

The improved steerability with a high NA lens will also unleash the potential of the MMA. It would relax the constraints on the optical setup and lead to a configuration that could be used for addressing different numbers of ions in the trap by steering the mirrors. This is opposed to the setup designed in this thesis, which was specifically tailored to address three ions in a three ion crystal or four ions in a four ion crystal respectively.

A. ZEMAX OpticStudio

ZEMAX OpticStudio is the software with which all of the simulations given in Chapter 4 were performed. In this appendix I want to give a short introduction on how to set up a simulation with Gaussian optics. A detailed description of all features can be found in the manual of ZEMAX OpticStudio [66].

All the features of OpticStudio that I mention in this section can be found in the software under **Help** → **Feature Finder**. The features will be highlighted in italic.

Preliminaries

Before inserting the desired setup into the software, the wavelength of the laser used in the setup and the aperture have to be defined. This is done in the *System Explorer*. When using *Physical Optics Propagation* to propagate Gaussian beams through the setup, the aperture type should be set to "Float By Stop Size", such that it won't influence the calculations. For this aperture definition, the semi-diameter of the stop surface is used to determine the propagation of geometrical rays through the system. The stop surface is one of the surfaces that needs to be defined in the *Lens Data*, which is described in the following paragraph.

Defining an optical system

The system of lenses that shall be simulated is inserted into the *Lens Data* editor surface by surface. A picture of the *Lens Data* editor with some relevant surfaces in it is given in Figure A.1.

A. ZEMAX OpticStudio

	Surf.Type	Comment	Radius	Thickness	Material	Coating	Semi-Diameter
0	OBJECT	Standard ▾	Object	Infinity	0.000		0.000
1		Standard ▾	Beam Launch	Infinity	0.100		8.000E-03 U
2	STOP	Standard ▾	System Aperture	Infinity	1.400		7.000E-03 U
3	(aper)	Even Asphere ▾	lens 1 front	Infinity	1.000	F_SILICA	0.305 U
4	(aper)	Even Asphere ▾	lens 1 back	-0.950	0.000		0.305 U
5		Standard ▾	Free space before MMA	Infinity	45.000		0.152
6	(aper)	Irregular ▾	MMA	Infinity	0.000		0.042 U
7		Coordinate Break ▾	Displacements		0.000	-	0.000
8		Standard ▾	Free space before objective	Infinity	690.000		10.000 U
9	(aper)	Standard ▾	Vacuum window	Infinity	6.000	SILICA	7.500 U
10	(aper)	Standard ▾	Vacuum	Infinity	117.965	VACUUM	7.500 U
11	(aper)	Even Asphere ▾	Edmund Optics 67257	6.054	7.000	N-SF5	ZEC_MF825
12	(aper)	Standard ▾	Vacuum	Infinity	5.035 S	VACUUM	ZEC_NIRI673
13	IMAGE	Standard ▾	Ion Position	Infinity	-		0.014

Figure A.1.: Picture of the *Lens Data* editor in ZEMAX OpticStudio.

Each surface in the *Lens Data* editor has a set of properties, which are displayed in the surface's row. The first property is the surface type, which defines the other properties a surface can have. A "Standard" surface for example is only defined through its radius of curvature, thickness, material, coating and semi-diameter. The surface type "Even Asphere" also includes asphere coefficients, an "Irregular" surface can be decentred and tilted with respect to the rest of the setup and a "Coordinate Break" surface rotates and decentres the part of the setup in front of it relative to the setup behind it.

In the example setup given in Figure A.1 the zeroth surface is the object surface which acts as a point source for geometric ray tracing. The rays from the point source are propagated to the stop surface, which introduces an aperture defined in the *System Explorer* to it. The semi-diameter value of the stop surface and the distance to it, given by the thickness of surface two, can be adjusted to alter the propagation of geometric rays through the setup. Those rays are displayed in the *3D Viewer* and the *Shaded Model*, which can be used to display the system. The values for radius and thickness of a surface should be read from left to right, meaning that the radius of curvature of a surface occurs before the propagation through it. A radius of infinity indicates a flat surface.

Using Physical Optics Propagation

After the optical system has been defined, the *Physical Optics Propagation* feature can be used to define a Gaussian beam going through the system. First, the input beam needs to be defined in the "Beam Definition" tab, which is displayed in Figure A.2.

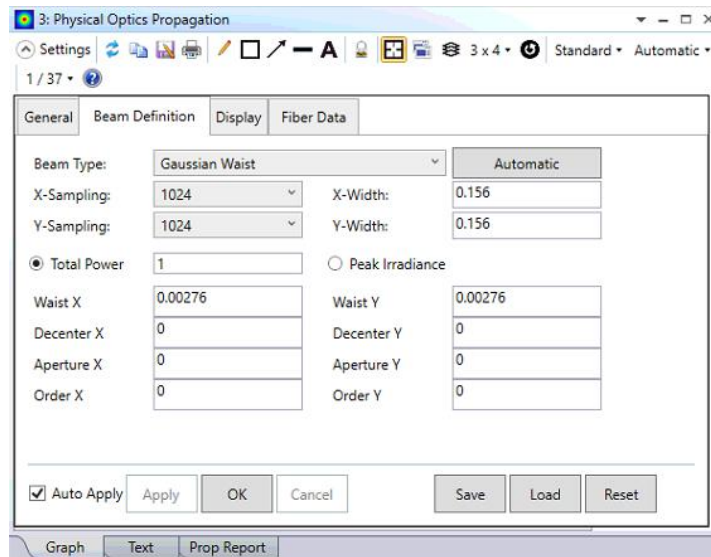


Figure A.2.: The input beam parameters for the Gaussian propagation are plugged into the "Beam Definition" tab in *Physical Optics Propagation*.

Several different beam types can be chosen, which differ in the set of parameters wherewith they are defined. The one that I used for my simulations is the "Gaussian Waist" type, where the waist of the input beam in x and y direction is plugged into the simulation. The resulting input beam is then given as

$$E(x, y) = E_0 \exp \left(- \left(\frac{x^2}{w_{0x}^2} + \frac{y^2}{w_{0y}^2} \right) \right) . \quad (\text{A.1})$$

Additionally, the input beam can be decentred and truncated. Further, higher order Hermite-Gaussian beams can be introduced into the setup by setting the parameters "Order X" and "Order Y".

Note: Before the beam definition can be used outside of the *Physical Optics Propagation* feature, it has to be saved by clicking the save button on the "Beam Definition" tab.

Note: The input parameters defined in this window will be the beam parameters at the start surface defined in the "General" tab. Setting the start surface to "Ent. Pupil" will release the beam at the stop surface.

Note: It is important, that the beam is sufficiently sampled over the whole beam array, otherwise beam shapes will be distorted by aliasing. Strategies on how to accomplish this can be found here¹ in the articles "Using Physical Optics Propagation (POP), Part 1: Inspecting the beams", "Using Physical Optics Propagation (POP), Part 2: Inspecting the beam intensities" and "Using Physical Optics Propagation (POP), Part 3: Inspecting the beam phases".

After the beam has been defined and saved, the beam parameters at each surface can be read out by using the *Merit Function Editor*.

¹<http://customers.zemax.com>

The Merit Function Editor

In the *Merit Function Editor* a wide variety of parameters from the setup can be calculated and used to define a merit function, with which the system can be optimised. All of the available operands which can be used in the merit function are summarised in the chapter "Optimization Operands Summary" in Ref. [66]. The most important operator when dealing with Gaussian beams is the POPD operator. It outputs parameters of the Gaussian beam obtained from the propagation within *Physical Optics Propagation*.

The data value of the POPD operand determines which parameter is computed at the surface given by the surface value. An important data value is value 3, which gives the total power at the specified surface. It is obtained by integrating the irradiance over the entire beam array. The data values 11 and 12 give the X and Y coordinate of the centre of the beam array relative to the optical axis at the specified surface. Further, the two values 21 and 22 give the centroid c_x/c_y of the intensity distribution in the beam array relative to its centre. The centroid is calculated as

$$c_x = \frac{\int xI(x, y)dxdy}{\int I(x, y)dxdy} \quad . \quad (\text{A.2})$$

Thus, the absolute position of the Gaussian beam on the end surface can be calculated by summing the two data values 11 and 21 for the x value and 12 and 22 for the y value respectively. The values 23 and 24 give the beam width in X and Y direction, which is calculated as

$$w_{D4\sigma} = 2\sqrt{\frac{\int (x - c_x)^2 I(x, y)dxdy}{\int I(x, y)dxdy}} \quad . \quad (\text{A.3})$$

This is the so called $D4\sigma$ -waist, which gives the beam radius at the $1/e^2$ intensity point for an arbitrary intensity distribution. For a Gaussian profile it is equal to the $1/e^2$ waist w_0 .

The two data values 25 and 26 give the M^2 parameter of the beam in X and Y direction respectively. The parameter is calculated via

$$w_{D4\sigma}^2(z) = w_{D4\sigma}^2(0) + M_x^4 \left(\frac{\lambda z}{\pi w_{D4\sigma}(0)} \right)^2 \quad (\text{A.4})$$

When those parameters are plugged into the merit function editor they can be used to optimise the system.

Optimising the setup

Optimisation of the setup begins with defining a suitable merit function, which is done by setting targets and weights for the operands in the *Merit Function Editor*. The targets specify onto which value the corresponding operator shall be optimised and the weights specify how much importance is put onto the optimisation of this operand.

All of the operands in the *Merit Function Editor* with non-zero weights contribute to the merit

function, which the software can minimise.

Before one can optimise the setup, one first has to specify variables in the *Lens Data* editor. This can be done by setting the solve of a surface parameter to "Variable", which is achieved by clicking the square on the right of a surface parameter. This way, surface thicknesses, radii, decentres and tilts can be set variable for example.

OpticStudio provides deterministic and stochastic optimisation algorithms. The deterministic algorithm is called *Optimize!*; it uses the damped least squares or orthogonal descent algorithm to arrive at a local minimum. Thus, with this technique the setup can only be optimised locally. For a global optimisation the stochastic algorithm *Global Search* can be used. This algorithm is in principle capable of finding the global minimum of the merit function, but this is never guaranteed, as is stated in the manual [66]:

It is important to realize that there is no guarantee that the true global optimum will always, or even occasionally be found.

ZEMAX macro for summing several beams

In this master's thesis I have shown several results from the simulation where more than one beam is displayed at a surface. Those results include Figures 4.8, 4.11 and 6.3. These images were obtained within the software OpticStudio with the following ZPL macro:

```
Path$=$DATAPATH()+"\POP\BEAMFILES\"

number_of_beams=3
! Surface where the beams were extracted
surface=30

FOR i, 1, number_of_beams, 1

print i
number$=$str(i)
if i<=9
number$=$LEFTSTRING(number$,1)
else
number$=$LEFTSTRING(number$,2)
endif
file1$="Setup ",number$,".ZBF"
file2$="Setup ",number$," decentered.ZBF"
file1_full_path$=path$ + file1$
file2_full_path$=path$ + file2$
COPYFILE file1_full_path$, file2_full_path$

print file1$
SETCONFIG i
```

A. ZEMAX OpticStudio

```
POPD=OCOD("POPD")
x_decenter=OPEV(POPD,surface,0,0,11,0,0)+OPEV(POPD,surface,0,0,21,0,0)
y_decenter=OPEV(POPD,surface,0,0,12,0,0)+OPEV(POPD,surface,0,0,22,0,0)
ZBFRESAMPLE file2$, 0,0,0,0,x_decenter, y_decenter
print x_decenter
print y_decenter

NEXT i

fileA$="Setup ","1", " decentered.ZBF"
fileB$="Setup ","2", " decentered.ZBF"
fileC$="Incoherent superposition.ZBF"

ZBFSUM 0 fileA$ fileB$ fileC$

ZBFSHOW fileC$

FOR i, 3, number_of_beams, 1

print i
number$=$str(i)
if i<=9
number$=$LEFTSTRING(number$,1)
else
number$=$LEFTSTRING(number$,2)
endif
fileA$="Setup ",number$," decentered.ZBF"

ZBFSUM 0 fileA$ fileC$ fileC$

NEXT i

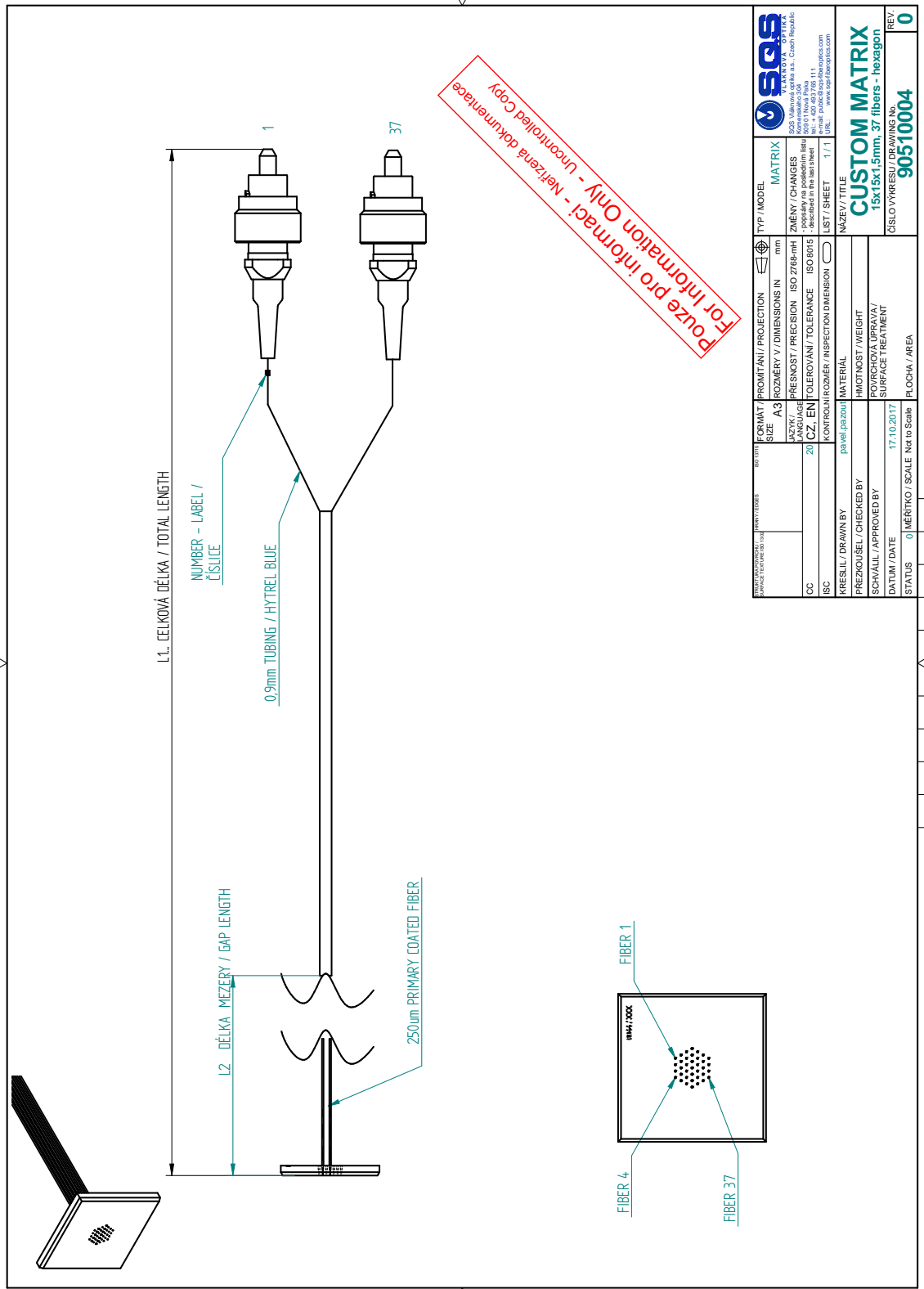
ZBFSHOW fileC$

PRINT "done"
END
```

The macro takes the beam files "Setup #" and sums them incoherently onto a single output image. The positions of the beams on the corresponding surface are extracted with the POPD operands 11, 12, 21 and 22.

B. Specifications of the new fibre array from SQS

In this appendix the technical drawings for the new fibre array with 37 fibres in a honeycomb structure are presented. They are given in Figures B.1, B.2 and B.3. Additionally, the PER, insertion loss and positions of the fibre cores are comprehended in Figure B.4.



The reproduction, distribution and utilization of this document as well as the communication of its contents to others without expressed authorization is prohibited. Offenders will be held liable for the payment of damages. All rights reserved in the event of the grant of a patent, utility model or design.

Reprodukční, šíření a poskytnutí tohoto dokumentu, jeho částí nebo jeho obsahu je bez výslovného povolení zakázáno. Pochybnost zůstává k odpovědnosti za vzniklou škodu. Všechna práva jsou vyhrazena.

FORMÁT / FORMAT	A3	PROJEKCE / PROJECTION	MATRIX
ROZMĚRY / DIMENSIONS IN	mm	ZMĚNY / CHANGES	
ČÍSLO / NO.	20	PŘESNOST / PRECISION	ISO 2768-mH
KONTROLNÍ ROZMĚRY / INSPECTION DIMENSION		TOLEROVÁNÍ / TOLERANCE	ISO 9015
KRESLIL / DRAWN BY	pavel.jasouzi	LIST / SHEET	1 / 1
PŘEZKOUŠEL / CHECKED BY		NÁZEV / TITLE	CUSTOM MATRIX
SCHVÁLIL / APPROVED BY		HMOTNOST / WEIGHT	15x15x1,5mm, 37 fibers - hexagon
DATUM / DATE	17.10.2017	POVRCHOVÁ ÚPRAVA / SURFACE TREATMENT	
STATUS	0	ČÍSLO VÝKRESU / DRAWING NO.	90510004
INFORMACE / INFORMATION		POVRCHOVÁ ÚPRAVA / SURFACE TREATMENT	
POVrchová úprava / Surface treatment		ČÍSLO VÝKRESU / DRAWING NO.	90510004
POVrchová úprava / Surface treatment		REV.	0

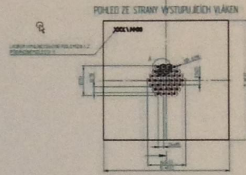
Figure B.2.: The FC/APC connectors are numbered from 1 to 37. The inset at the bottom left corner shows where the corresponding fibres have their output in the array.



DELIVERY PROTOCOL

Description: 2D Fiber Array with connectors (Matrix) 37ch-hexagon

Product no.: 90510004
 Revision: 00
 SQS order no.: Z17-3319
 Serial no.: F0044/001



FA dimension: 15 x 15 x 1,5 mm
 FA material: fused silica
 FA pitch: 0,6495 x 0,5625 mm
 Fiber core offset(FCO): typ. 1 μm / max. 3 μm
 FA channel no.: 37
 Fiber type: PM PANDA-PM630HP
 Connector type: FC / APC

Measured DATA

IL, PER measured @ 635nm

Channel no.:	1	2	3	4	5	6	7	8	9	10	11	12	13
IL [dB]	0,30	1,05	0,87	0,55	0,81	1,10	0,38	0,71	0,50	0,69	0,21	0,90	0,54
PER [dB]	30,3	27,3	36,6	38,0	36,4	37,6	33,7	28,7	36,6	32,8	36,5	36,2	40,0
FCO [μm]	0,62	0,69	0,81	0,82	1,42	0,25	0,86	0,51	0,21	0,19	0,18	0,15	0,59

Channel no.:	14	15	16	17	18	19	20	21	22	23	24	25	26
IL [dB]	0,88	0,86	1,17	0,92	1,19	0,83	0,82	0,45	1,20	0,75	1,09	0,19	0,78
PER [dB]	36,9	34,1	31,2	32,9	40,0	32,1	30,8	40,0	30,7	34,6	27,0	38,3	33,5
FCO [μm]	0,39	0,39	0,46	0,29	0,23	0,49	0,14	0,83	0,50	0,51	0,95	1,26	0,47

Channel no.:	27	28	29	30	31	32	33	34	35	36	37		
IL [dB]	0,97	1,02	1,11	0,88	0,48	0,84	1,12	0,79	1,14	1,04	0,67		
PER [dB]	32,7	26,1	37,1	33,5	32,6	35,4	30,7	35,1	37,1	36,0	31,7		
FCO [μm]	0,47	0,88	0,80	1,17	1,33	0,52	0,16	1,31	1,20	1,26	1,57		

Tested by: F.Šútor

Reviewed by: P.Pazout

Figure B.4.: Data for the PER, insertion loss and deviation of the position of the fibre cores from the desired position in the array.

Bibliography

- [1] Schrödinger, E. Quantisierung als Eigenwertproblem. *Annalen der Physik* **384**, 489–527 (1926). URL <https://onlinelibrary.wiley.com/doi/abs/10.1002/andp.19263840602>.
- [2] Heisenberg, W. Über quantentheoretische Umdeutung kinematischer und mechanischer Beziehungen. *Zeitschrift für Physik* **33**, 879–893 (1925). URL <https://doi.org/10.1007/BF01328377>.
- [3] Turing, A. M. On computable numbers, with an application to the Entscheidungsproblem. *Proceedings of the London Mathematical Society* **s2-42**, 230–265 (1937). URL <https://londmathsoc.onlinelibrary.wiley.com/doi/abs/10.1112/plms/s2-42.1.230>.
- [4] Benioff, P. The computer as a physical system: A microscopic quantum mechanical hamiltonian model of computers as represented by turing machines. *Journal of Statistical Physics* **22**, 563–591 (1980). URL <https://doi.org/10.1007/BF01011339>.
- [5] Feynman, R. P. Simulating physics with computers. *International Journal of Theoretical Physics* **21**, 467–488 (1982). URL <https://adsabs.harvard.edu/abs/1982IJTP...21..467F>.
- [6] Deutsch, D. Quantum theory, the church–turing principle and the universal quantum computer. *Proceedings of the Royal Society of London A: Mathematical, Physical and Engineering Sciences* **400**, 97–117 (1985). URL <https://rspa.royalsocietypublishing.org/content/400/1818/97>.
- [7] Shor, P. W. Algorithms for quantum computation: discrete logarithms and factoring. In *Proceedings 35th Annual Symposium on Foundations of Computer Science*, 124–134 (1994). URL <https://ieeexplore.ieee.org/stamp/stamp.jsp?tp=&arnumber=365700>.
- [8] Grover, L. K. A fast quantum mechanical algorithm for database search. In *Proceedings of the Twenty-eighth Annual ACM Symposium on Theory of Computing, STOC '96*, 212–219 (ACM, New York, NY, USA, 1996). URL <https://doi.acm.org/10.1145/237814.237866>.
- [9] Lloyd, S. Universal quantum simulators. *Science* **273**, 1073–1078 (1996). URL <https://science.sciencemag.org/content/273/5278/1073>.

- [10] Schumacher, B. Quantum coding. *Phys. Rev. A* **51**, 2738–2747 (1995). URL <https://link.aps.org/doi/10.1103/PhysRevA.51.2738>.
- [11] Häffner, H., Roos, C. & Blatt, R. Quantum computing with trapped ions. *Physics Reports* **469**, 155 – 203 (2008). URL <https://www.sciencedirect.com/science/article/pii/S0370157308003463>.
- [12] Barz, S. Quantum computing with photons: introduction to the circuit model, the one-way quantum computer, and the fundamental principles of photonic experiments. *Journal of Physics B: Atomic, Molecular and Optical Physics* **48**, 083001 (2015). URL <https://stacks.iop.org/0953-4075/48/i=8/a=083001>.
- [13] Devoret, M. H. & Schoelkopf, R. J. Superconducting circuits for quantum information: An outlook. *Science* **339**, 1169–1174 (2013). URL <https://science.sciencemag.org/content/339/6124/1169>.
- [14] Schindler, P. *et al.* A quantum information processor with trapped ions. *New Journal of Physics* **15**, 123012 (2013). URL <https://stacks.iop.org/1367-2630/15/i=12/a=123012>.
- [15] Casabone, B. *Two Ions Coupled to an Optical Cavity: from an Enhanced Quantum Computer Interface towards Distributed Quantum Computing*. Ph.D. thesis, Universität Innsbruck (2015). URL https://quantumoptics.at/images/publications/dissertation/casabone_diss.pdf.
- [16] Monz, T. *et al.* 14-qubit entanglement: Creation and coherence. *Phys. Rev. Lett.* **106**, 130506 (2011). URL <https://link.aps.org/doi/10.1103/PhysRevLett.106.130506>.
- [17] Nigg, D. *et al.* Quantum computations on a topologically encoded qubit. *Science* **345**, 302–305 (2014). URL <https://science.sciencemag.org/content/345/6194/302>.
- [18] Monz, T. *et al.* Realization of a scalable shor algorithm. *Science* **351**, 1068–1070 (2016). URL <https://science.sciencemag.org/content/351/6277/1068>.
- [19] Martinez, E. *et al.* Real-time dynamics of lattice gauge theories with a few-qubit quantum computer. *Nature* **534**, 516–519 (2016). URL <https://dx.doi.org/10.1038/nature18318>.
- [20] Schmidt-Kaler, F. *et al.* How to realize a universal quantum gate with trapped ions. *Applied Physics B* **77**, 789–796 (2003). URL <https://doi.org/10.1007/s00340-003-1346-9>.
- [21] Nägerl, H. C. *et al.* Laser addressing of individual ions in a linear ion trap. *Phys. Rev. A* **60**, 145–148 (1999). URL <https://link.aps.org/doi/10.1103/PhysRevA.60.145>.
- [22] Saleh, B. E. A. & Teich, M. C. *Fundamentals of Photonics* (Wiley, 2007), 2nd edn.

Bibliography

- [23] Hempel, C. *Digital quantum simulation, Schrödinger cat state spectroscopy and setting up a linear ion trap*. Ph.D. thesis, Universität Innsbruck (2014). URL https://quantumoptics.at/images/publications/dissertation/hempel_diss.pdf.
- [24] Debnath, S. *et al.* Demonstration of a small programmable quantum computer with atomic qubits. *Nature* **536**, 63–66 (2016). URL <https://dx.doi.org/10.1038/nature18648>.
- [25] Linke, N. M. *et al.* Experimental comparison of two quantum computing architectures. *Proceedings of the National Academy of Sciences* **114**, 3305–3310 (2017). URL <https://www.pnas.org/content/114/13/3305>. <https://www.pnas.org/content/114/13/3305.full.pdf>.
- [26] Mølmer, K. & Sørensen, A. Multiparticle entanglement of hot trapped ions. *Phys. Rev. Lett.* **82**, 1835–1838 (1999). URL <https://link.aps.org/doi/10.1103/PhysRevLett.82.1835>.
- [27] Jurcevic, P. *Quantum Computation and Many-Body Physics with Trapped Ions*. Ph.D. thesis, Universität Innsbruck (2017). URL https://quantumoptics.at/images/publications/dissertation/Jurcevic_Dissertation.pdf.
- [28] Roos, C. F. *Controlling the quantum state of trapped ions*. Ph.D. thesis, Universität Innsbruck (2000). URL https://quantumoptics.at/images/publications/dissertation/roos_diss.pdf.
- [29] Foot, C. *Atomic Physics* (Oxford University Press, 2005).
- [30] White, H. E. *Fundamentals of Optics* (McGraw-Hill, 1976), 4th edn.
- [31] Siegman, A. E. *Lasers* (University Science Books, 1986).
- [32] Paul, W. & Steinwedel, H. Notizen: Ein neues Massenspektrometer ohne Magnetfeld. *Zeitschrift Naturforschung Teil A* **8**, 448–450 (1953).
- [33] Gulde, S. T. *Experimental Realization of Quantum Gates and the Deutsch-Jozsa Algorithm with Trapped $^{40}\text{Ca}^+$ Ions*. Ph.D. thesis, Universität Innsbruck (2003). URL https://quantumoptics.at/images/publications/dissertation/gulde_diss.pdf.
- [34] Drewsen, M. & Brøner, A. Harmonic linear paul trap: Stability diagram and effective potentials. *Phys. Rev. A* **62**, 045401 (2000). URL <https://link.aps.org/doi/10.1103/PhysRevA.62.045401>.
- [35] James, D. Quantum dynamics of cold trapped ions with application to quantum computation. *Applied Physics B* **66**, 181–190 (1998). URL <https://doi.org/10.1007/s003400050373>.
- [36] Webb, S. The quantum harmonic oscillator. Published online: https://www.fisica.net/quantica/quantum_harmonic_oscillator_lecture.pdf.

- [37] Morigi, G., Eschner, J., Cirac, J. I. & Zoller, P. Laser cooling of two trapped ions: Sideband cooling beyond the lamb-dicke limit. *Physical Review A* **59**, 3797–3808 (1999). URL <https://doi.org/10.1103/PhysRevA.59.3797>.
- [38] Monz, T. B. *Quantum information processing beyond ten ion-qubits*. Ph.D. thesis, Universität Innsbruck (2011). URL https://quantumoptics.at/images/publications/dissertation/monz_diss.pdf.
- [39] Nielsen, M. A. & Chuang, I. L. *Quantum Computation and Quantum Information* (Cambridge University Press, 2010).
- [40] Chuang, I. L. & Gottesmann, D. Demonstrating the viability of universal quantum computation using teleportation and single-qubit operations. *Nature* **402**, 390–393 (1999). URL <https://dx.doi.org/10.1038/46503>.
- [41] Nolting, W. *Grundkurs Theoretische Physik 2*, chap. 1.3 (Springer, 2014).
- [42] Andersen, K. The mathematical technique in fermat’s deduction of the law of refraction. *Historia Mathematica* **10**, 48 – 62 (1983). URL <https://www.sciencedirect.com/science/article/pii/0315086083900320>.
- [43] Born, M. & Wolf, E. *Fundamentals of Optics* (Elsevier, 1980), 6th edn.
- [44] Feng, S. & Winful, H. G. Physical origin of the gouy phase shift. *Opt. Lett.* **26**, 485–487 (2001). URL <https://ol.osa.org/abstract.cfm?URI=ol-26-8-485>.
- [45] Self, S. A. Focusing of spherical gaussian beams. *Appl. Opt.* **22**, 658–661 (1983). URL <https://ao.osa.org/abstract.cfm?URI=ao-22-5-658>.
- [46] Chwalla, M. *Precision spectroscopy with $^{40}\text{Ca}^+$ ions in a Paul trap*. Ph.D. thesis, Universität Innsbruck (2009). URL https://quantumoptics.at/images/publications/dissertation/chwalla_diss.pdf.
- [47] Barton, P. A. *et al.* Measurement of the lifetime of the $3d^2D_{5/2}$ state in $^{40}\text{Ca}^+$. *Phys. Rev. A* **62**, 032503 (2000). URL <https://link.aps.org/doi/10.1103/PhysRevA.62.032503>.
- [48] Ramm, M., Pruttivarasin, T., Kokish, M., Talukdar, I. & Häffner, H. Precision measurement method for branching fractions of excited $P_{1/2}$ states applied to $^{40}\text{Ca}^+$. *Phys. Rev. Lett.* **111**, 023004 (2013). URL <https://link.aps.org/doi/10.1103/PhysRevLett.111.023004>.
- [49] Meth, M. *Dynamische Kontrolle von Laserimpulsen zur Quanteninformationsverarbeitung*. Master’s thesis, Universität Innsbruck (2017). URL https://quantumoptics.at/images/publications/diploma/MichaelMeth_Kontrolle_Laserimpulse_QIV.pdf.
- [50] Itano, W. M. *et al.* Quantum projection noise: Population fluctuations in two-level systems. *Phys. Rev. A* **47**, 3554–3570 (1993). URL <https://link.aps.org/doi/10.1103/PhysRevA.47.3554>.

Bibliography

- [51] Laplace, P.-S. *Essai philosophique sur les probabilités* (1814).
- [52] ANDOR. *ANDOR iXon Ultra*. Published online: <https://www.andor.com/cameras/ixon-emccd-camera-series>.
- [53] Nigg, D. *Towards fault tolerant quantum computation*. Ph.D. thesis, Universität Innsbruck (2016). URL https://quantumoptics.at/images/publications/dissertation/Nigg_Thesis.pdf.
- [54] Stricker, R. *Gatteroperationen hoher Güte in einem optischen Quantenbit*. Master's thesis, Universität Innsbruck (2017). URL https://quantumoptics.at/images/publications/diploma/master_stricker.pdf.
- [55] Gooch & Housego. *Fiber-Q 780nm Fiber Coupled Acousto-Optic Modulator*. Published online: https://goochandhousego.com/wp-content/uploads/2016/11/GH_DS_FO_FiberQ_780nm_150MHz_Fiber_Coupled_Acousto-Optic_Modulator.pdf.
- [56] Simbol Test Systems Inc. Polarization maintaining alignment within optical fiber systems (2009). Published online: <https://www.simbol.ca/lab/pages/Polarization-Maintaining-Alignment-within-Optical-Fiber-Systems-.html>.
- [57] Schäfter + Kirchhoff. *MANUAL Polarization Analyzer SK010PA-VIS,-UVIS,-NIR,-IR*, 4.6.2 edn. (2012).
- [58] Kaspar, P. *Aufbau und Charakterisierung eines frequenzverdoppelten Lasersystems für die Zwei-Photonen Rydberg-Anregung von Rubidium*. Master's thesis, Universität Stuttgart (2015). URL https://www.pi5.uni-stuttgart.de/common/show_file.php/finished_thesis/142/beschaenkt/thesis.pdf.
- [59] PowerPhotonic. Lightforge - rapid prototyping (2016). Published online: <http://www.powerphotonic.com/rapid-prototyping>.
- [60] Schindler, P. *Quantum computation and simulation with trapped ions using dissipation*. Ph.D. thesis, Universität Innsbruck (2013). URL https://quantumoptics.at/images/publications/dissertation/schindler_diss.pdf.
- [61] Wang, M. *et al.* The AME2016 atomic mass evaluation (II). Tables, graphs and references. In *Chinese Physics C*, vol. 41 (2017).
- [62] Metcalf, H. & van der Straten, P. *Laser cooling and trapping* (Springer, 1999).
- [63] Duan, K. & Lü, B. Nonparaxial analysis of far-field properties of gaussian beams diffracted at a circular aperture. *Opt. Express* **11**, 1474–1480 (2003). URL <https://www.opticsexpress.org/abstract.cfm?URI=oe-11-13-1474>.
- [64] Schindler, P. *Frequency synthesis and pulse shaping for quantum information processing with trapped ions*. Master's thesis, Universität Inns-

bruck (2008). URL https://quantumoptics.at/images/publications/diploma/diplom_schindler.pdf.

[65] Brandl, M. F. *Towards Cryogenic Scalable Quantum Computing with Trapped Ions*. Ph.D. thesis, Universität Innsbruck (2016). URL https://quantumoptics.at/images/publications/dissertation/brandl_diss_web.pdf.

[66] ZEMAX, LLC. OpticStudio 16.5 SP5 Help Files.